Transient resonances in extreme-mass-ratio inspirals

Priti Gupta

Graduate School of Science
Kyoto University

This dissertation is submitted for the degree of
Doctor of Philosophy

July 2022

In loving memory of my mother, Anju, and grandparents Shiv & Tara ...

You are with me every step of the way.

Declaration

I hereby declare that except where specific reference is made to the work of others, the contents of this dissertation are original and have not been submitted in whole or in part for consideration for any other degree or qualification in this, or any other university. This dissertation is my own work and contains nothing which is the outcome of work done in collaboration with others, except as specified in the text and Acknowledgements. All concepts, results and data obtained by others are properly referenced. This dissertation contains fewer than 65,000 words including appendices, bibliography, footnotes, tables and equations and has fewer than 100 figures.

Priti Gupta
July 2022

Acknowledgements

"And now, Harry, let us step out into the night and pursue that flighty temptress, adventure."

The path to a doctoral thesis is arduous, which fortunately is supported by a group of people in many significant ways. My journey was no different.

Looking back at the beginning of my research career, I am indebted to my Master's supervisor, Kei-ichi Maeda. Thank you for accepting me as your student, allowing me to work in this exciting field, and guiding me patiently through each learning curve. I would not be here today if it weren't for your guidance.

I want to express my gratitude to my incredible thesis advisor, Takahiro Tanaka, for his suggestions, encouragement, frequent meetings, and endless ideas for research directions. During Covid times, he did not let us feel disheartened and was always a call away for discussions. I cannot imagine the end of this thesis without his enduring support. I greatly appreciate all his help outside the research matters that he welcomed with a smiling face.

During these years, I had the additional pleasure of collaborating with fantastic researchers. I am thankful to Hirotada Okawa for his help with the silly bugs in the code and feedback on my grant/fellowship applications. I immensely admire his genius and grounded personality. Another invaluable member in the three-body project was Haruka Suzuki, who has always made me feel welcome with my stack of doubts.

In retrospect, I feel happy that I participated in the JGRG conference in Kobe and met another collaborator, Alvin Chua, just in time before Covid took over. Since then, it has been a fantastic working experience with him. I appreciate his crisp and clear views on research work, which always motivated me to do better after our calls. Another big thanks to him for connecting me to Beatrice Bonga. While it would have been amazing to meet her in person, the virtual meetings have had quite an impact on my research path. The passion she holds for work is captivating and contagious! Undoubtedly, her honest and detailed feedback has made me a better researcher. Near the last year of my doctoral program, Lorenzo Speri joined our project and shared his expertise on data analysis techniques. I am thankful to him for answering my questions with such eloquence.

I have also benefited a lot from the academic aura of the Physics department. The weekly night seminar with my research group members was a great place to share progress and

also things that did not work. I am thankful to all the members for their questions and suggestions. A special thanks to my office-mate Kei Yamada for his explanations of several concepts, Kota Ogasawara, who diligently aided me in my struggle with Japanese documents despite his busy schedule, and Lucy McNeil for her feedback on my post-doc applications. In addition, I express my gratitude to Kiyoe Yokota for her work in the background so the researchers could work in peace with minimal attention to administrative paperwork.

Living in a foreign country with a language barrier comes with challenges and requires increased efforts to maintain relationships. With the Covid situation, I had a strong support system extended by my family and friends in this emotional time. First and foremost, my parents thank you for believing in me and letting me pursue my interests with no interference. Thank you for doing the best you could to raise and educate us. I hope to make you proud always. A final thanks to my friends — Abhishek and Akash for the meaningful long conversations and science discussions. You both have played a significant role in my research career. Thanks to Ekashmi, Jyoti, Laura, Priyanka, Sabrina, and Vandana for maintaining this long-distance friendship and holding your end gracefully in the pandemic. A special thanks to Ankit for reminding me to smile more often in rough times and listening to my rants calmly. You make me feel grounded when things are upside down and help me find a balance that I probably would not have conquered on my own.

This thesis's work was supported by MEXT (DC1) and JSPS (DC2) grants and fellowship.

Abstract

From the 17th century until recently, the scientific community observed and gathered tremendous information about the cosmos solely through electromagnetic (EM) radiation and Neutrinos. While the ends of the EM spectrum limited astronomy, parallel breakthroughs in technical and theoretical fronts made it possible to open a new window to observe the universe: Gravitational-wave (GW) astronomy. We witnessed the first direct detection of GWs in 2015 by two LIGO interferometers [1]. Since then, nearly a hundred of merging stellar-mass binaries have been identified, with more to follow in the next decade [2]. While LIGO and other ground-based detectors continue searching for these high-frequency signals, the space-based interferometers (LISA, TianQuin, DECIGO) [3–5] will explore the sources emitting GWs in the low frequency range (mHz-deci Hz). One of the most important sources for LISA will be the capture orbits of stellar-mass compact objects into the massive black holes that reside in galactic nuclei. These are known as extreme-mass-ratio inspirals (EMRIs), and the observation of even a single such source can significantly advance our understanding of massive black holes, their stellar environments, or even the true theory of gravitation itself. GW astronomy is an intricate inverse problem where source signals are buried in the detector noise. Apart from the technical challenges, unlocking the scientific potential of sources like EMRIs with complex orbital dynamics heavily depends on our theoretical knowledge. To filter the signal present in the noise, we need accurate modeling of the predicted EMRI waveform. The event is then further analyzed to infer source properties. Both detections of signals and bias in parameters are directly affected if our waveform templates are inaccurately modeled.

Despite two decades of research activity in the area, many critical pieces remain to be incorporated. For instance, the current models are focused on clean, isolated EMRI systems, i.e., unaffected by the environment. This assumption is well motivated (although uncertain) as the clean systems will offer uninfluenced tests of general relativity (GR) in a strong-field regime. A recent work [6] pointed out that nearby stellar-mass objects induced resonances leave an observable imprint on the gravitational waveform. These resonances contain information about the next closest black hole(s) or

stars to these systems, which cannot be obtained otherwise and may contain important clues for astrophysicists studying the formation of galaxies. Moreover, if we do not account for these resonance effects, we lose the opportunity to perform precision tests of GR with EMRIs and may even misattribute the effect of these nearby objects to deviations from GR.

My current research carries out an in-depth study of these newly discovered tidal resonances in EMRIs by exploring their impact on the EMRI's orbital parameter space. We find that a large portion of inspirals encounter a low-order resonance in the observationally important regime. Moreover, we show that the effect is detectable for a significant fraction of sources. Motivated by this result. we extended our work and also present a new fast and efficient waveform model taking resonances into account. Using this model and Fisher matrices, we study the parameter measurement precision, and the bias induced by ignoring resonances.

Table of contents

List of figures

Nomenclature

Symbols

c	speed of light
G	Gravitational constant

Abbreviations

BH	Black hole
CBC	compact binary coalescence
COBE	Cosmic Background Explorer
CSPT	Cumulative shift of periastron time
EHT	Event horizon telescope
EM	Electromagnetic
EMRI	Extreme Mass Ratio Inspiral
ESA	European Space Agency
ET	Einstein telescope
GR	General theory of relativity
GW	Gravitational wave
INTEGRAL	INTErnational Gamma-Ray Astrophysics Laboratory
KAGRA	Kamioka Gravitational Wave Detector
LIGO	Laser Interferometer Gravitational-wave Observatory

LISA	Laser Interferometer Space Antenna
LVC	LIGO-Virgo collaboration
NanoGrav	North American Nanohertz observatory
NASA	National Aeronautics and Space Administration
NR	Numerical relativity
NS	Neutron star
PN	Post-Newtonian
PTA	Pulsar timing array
QNM	Quasi normal modes
SMBH	Supermassive black hole
SNR	Signal-to-noise ratio
SR	Special theory of relativity
TT	Transverse–Traceless
VLBI	Very-long baseline interferometry
WMAP	Wilkinson Microwave Anisotropy Probe

Chapter 1

Introduction

"In questions of science, the authority of a thousand is not worth the humble reasoning of a single individual." - Galileo Galilei

The 17th century saw Sir Isaac Newton publish his most acclaimed work, *Principia Mathematica*, laying the foundation for classical mechanics and giving birth to the Universal Law of Gravitation. He introduced the concept of absolute space and time. Shakespeare's words "All the world is a stage" are an apt metaphor for this theory, where all creation is enacted on a stage (space-time) that never changes. In *Principia*, Newton described a gravitational force that was inversely proportional to the square of the distance between the centers of mass and proportional to the product of the masses of the bodies. In mathematical notation, the force between masses m_1 and m_2, at a distance r and gravitational constant G is,

$$F = \frac{Gm_1m_2}{r^2}. \tag{1.1}$$

Newton's law of gravitation proved to be an invaluable tool to astronomers, allowing them to predict the motion of planets. However, over the century that followed, astronomical observations brought to light some minute deviations between Newton's theory and what was observed. A prominent observation was Mercury's peculiar precession, a phenomenon explained by Newton's gravity as a result of planetary perturbations. This effect is demonstrated in Fig. 1.1. The observed precession of 574" per century did not agree well with Newton's calculations of 531" per century, with an additional 43" per century that would later be accounted for by GR [7].

In 1905, Albert Einstein published his paper on SR [8, 9] which was based on two key postulates — 1) the laws of physics are the same in all inertial frames of reference, and 2) speed of light must be constant, measured by any two observers, regardless

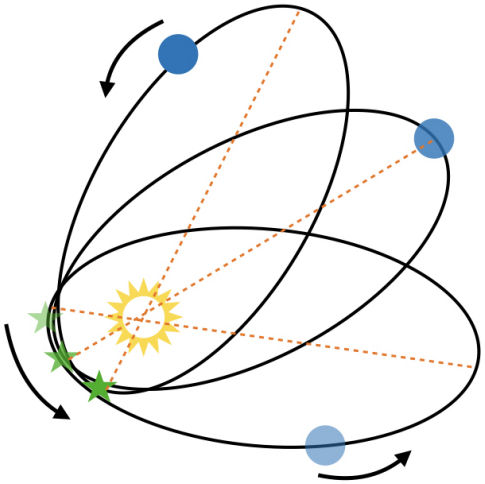

Fig. 1.1 Demonstration of the advance of Mercury's (blue) perihelion (star) about the Sun (yellow). Figure not to scale.

of their relative motion. Einstein united space and time by treating them on equal footing and hence, abolishing Newton's idea of absolute space and time. In 1915, he went on to extend SR to GR where he presented a geometrical view of gravity with curvature being caused by the presence of mass. The words of John Archibald Wheeler sum it up well — *"Space-time tells matter how to move; matter tells space-time how to curve"*. This complex theory of gravity is encapsulated within the famous Einstein field equations [10]:

$$G_{\mu\nu} = \frac{8\pi G}{c^4} T_{\mu\nu}. \tag{1.2}$$

In the above expression, the right-hand side describes the energy/matter content of the system via the stress-energy tensor $T_{\mu\nu}$, while the left-hand side describes the curvature of space-time via the Einstein Tensor $G_{\mu\nu}$. In weak-field limits, GR reduces to Newtonian gravity, or in reverse, it extends Newtonian gravity to stronger gravitational fields. Since its birth, GR has been tested several times and came out with flying colors [7]. To support/check his theory, Einstein proposed three observational tests: the precession of Mercury's orbit, the deflection of light about the Sun, and the gravitational redshift of light. GR could explain the advancement of Mercury's orbit and agreed strongly with the observation.

Sir Arthur S. Eddington an English astronomer, carried out the second test in May 1919 (see Fig 1.2 for schematic description), observing a solar eclipse and concluding that the light passing close to the Sun was indeed bent in a manner consistent with GR

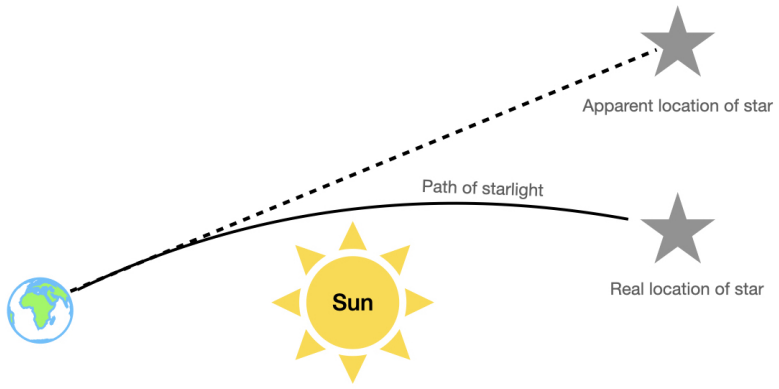

Fig. 1.2 Demonstration of light deflection by the Sun. Figure not to scale.

[11]. Soon after, Walter S. Adams an American astronomer, measured the predicted gravitational redshift in 1925, which describes the shift in photon wavelengths to longer wavelengths when observed from a higher gravitational potential [12]. In the past century, such experiments have improved significantly while continuing to demonstrate the validity of Einstein's theory of general relativity. Moreover in 2019, we have had the unique opportunity to probe the space-time surrounding a SMBH at the center of galaxy M87. An image of the SMBH M87 was obtained using EHT [13], which combined observations from seven millimeter and sub-millimeter instruments around the globe (or VLBI). The image reconstructed is in close agreement with theoretical predictions of GR [14].

In 1905, Henri Poincare, a French mathematician was independently attempting to resolve the problem of instantaneous action at a finite distance posed by Newtonian gravity. He assumed that the gravitational force propagates at the speed of light, and the effect is propagated by gravitational waves (ondes gravifiques). The term 'Gravitational waves' was first used in his paper 'On the Dynamics of the Electron', published by the French Académie des Sciences [15]. In 1916, Einstein predicted the existence of GWs — ripples in the space-time fabric as a direct consequence of his field equations. Einstein (not fully convinced) spent a long time on this problem and after meaningful inputs from De Sitter, Leopold Infeld and Howard Robertson, resubmitted the proofs in 1936 after correcting the mathematical errors and was convinced of their existence.

In 1974 American physicists, Joseph H. Taylor and Alan R. Hulse together discovered a binary pulsar PSR B1913+16 or commonly known as the "Hulse-Taylor" binary [16] after its discoverers. This fascinating binary system was carefully studied over the

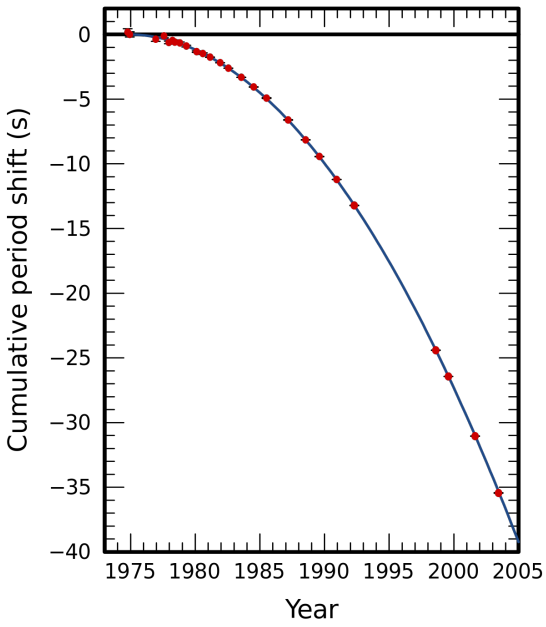

Fig. 1.3 Decay of the orbital period of the Hulse-Taylor binary pulsar system PSR B1913+16 [17] (data points with error bars "mostly too small to see"). The solid line depicts the predicted orbital decay from the emission of GWs, which is in remarkable agreement with the observed data. The years in the late 1990s with no data correspond to the period when Arecibo telescope was closed for upgrades. From Ref. [17] under non-exclusive license.

following three decades and proved to be one of the significant events in the history of detection of GWs. The binary orbit shrinks due to the GW emission resulting in decrease of orbital period. As shown in the Fig 1.3, the decay of the period clearly appeared in the cumulative shift of the periastron time. The observed CSPT curve matches perfectly with the predictions of GR, which tells us that GWs carry energy and angular momentum away from the system. This astronomical observation gave concrete evidence for the existence of GWs and as well as a first indirect GW observation. In 1993, the duo received the Nobel Prize "*for the discovery of a new type of pulsar, a discovery that has opened up new possibilities for the study of gravitation*".

The direct detection of GWs has been a long and arduous process due to their incredibly difficult measurement. The initial run of LIGO lasted from 2002 to 2010 with no detections. Several decades later, on the historic day of September 14, 2015 the LIGO observatories located in Hanford, and Livingston, simultaneously observed GWs from a binary black hole system — GW150914 [1]. Based on a careful analysis of the data, it was estimated the signal originated from a merging binary BHs with masses

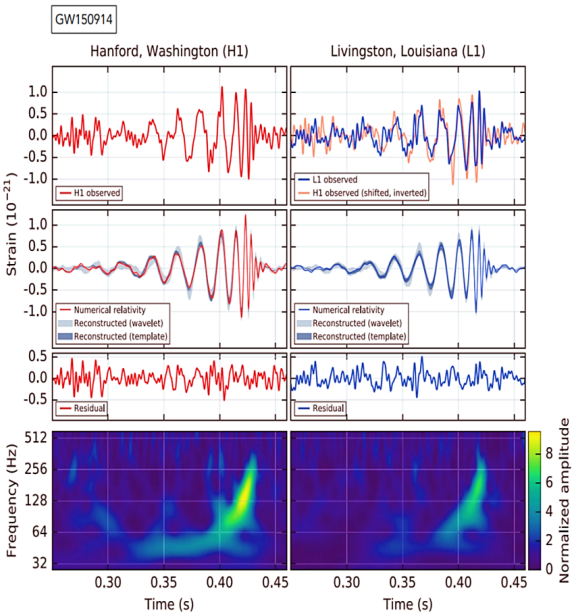

Fig. 1.4 GW150914 detected by LIGO observatories at Hanford and Livingston (See text for details). From the discovery paper, Ref. [1] distributed under Creative Commons Attribution 3.0 License.

of 36^{+4}_{-5} $M_\odot$ and 29^{+4}_{-4} $M_\odot$, located 410^{+160}_{-180} Mpc away. During a fraction of a second, this event released approximately fifty times the energy of all the stars in the universe. Usually, such perturbations of space-time are listed as a quantity called *strain*, which is given by $\Delta L/L$, where L is the characteristic distance between two masses, and ΔL is the resulting change in length between them caused by the passing of a gravitational wave. The GW strain measured by LIGO for GW150914 was 10^{-21}, which means that as the wave peaked, the LIGO arms oscillated by about 0.1 percent of the radius of a proton! In figure 1.4, the first row shows the strain versus time in the two detectors. The solid line in the second row shows a NR waveform for a source with parameters consistent with the merger, ringdown, and inspiral of binary BHs showing excellent agreement with the observed signal. In 2017, Reiner Weiss, Barry Barish and Kip Thorne were awarded the Nobel Prize *"for decisive contributions to the LIGO detector and the observation of gravitational waves"*.

The first observation run (O1) lasted from September 2015 to January 2016 and the second observation run (O2) lasted from November 2016 to August 2017. During the end of O2 term, Virgo detector in Italy joined the venture and together with LIGO collaboration (or LVC) detected nine more GW signals from merging BH binaries, as well as one detection of GWs from a merging pair of neutron stars, GW170817 [18].

The first NS-NS binary detection was significant because a short gamma-ray burst had been observed by the Fermi and INTEGRAL satellite, a second after the end of the GW signal. Virgo helped in localization of the event, and an alert was released to different observatories all over the world to follow up EM observations from the event [19]. Combining with the third observation run (commenced on April 2019), close to hundred observations of GWs have been made by LVC [20]. Undoubtedly, with advanced sensitivity, the network of detectors will fetch numerous signals in the coming era and a new science.

Several tests of GR and fundamental physics are already feasible with these first detections, such as: *Is the ring down phase of the observed waveform consistent with the QNMs of the final black hole predicted by GR?* The BH ringdown radiation) is characterized by QNMs with frequency f and damping time τ. Both the damping time and frequency of this oscillation are determined by the mass and spin of the Kerr BH formed after the merger (denoted by M_f and χ_f, respectively). In GR, the ringdown waveform $h_+(t) - ih_\times(t)$ is a superposition of various modes such that [21],

$$h_+(t) - ih_\times(t) = \sum_{\ell=2}^{+\infty} \sum_{m=-\ell}^{\ell} \sum_{n=0}^{+\infty} \mathcal{A}_{\ell mn} \exp\left[-\frac{t-t_0}{(1+z)\tau_{\ell mn}}\right] \exp\left[\frac{2\pi i f_{\ell mn}(t-t_0)}{1+z}\right] {}_{-2}S_{\ell mn}(\theta, \phi, \chi_{\rm f}), \tag{1.3}$$

where z is the cosmological redshift, and the (ℓ, m, n) indices label the QNMs. The quantitiy $\mathcal{A}_{\ell mn}$ is the complex amplitude that measures the mode excitation and the phase of modes at a reference time. All the $f_{\ell mn}$ and $\tau_{\ell mn}$ are determined by the final mass and spin of the remnant. Usually, $(\ell, m) = (2, 2)$ mode are dominant due to the longest damping time. We can compare the prediction by GR with the damped oscillating behavior of the final part of the waveform. This test was performed with GW150914 and within the available accuracy, data is consistent with GR prediction for frequency and decay time of the damped black hole QNM [22].

Soon, more events are expected with a high SNR flooring the way for more stringent tests. Moreover, the observations ahead may answer the following fundamental questions and paint a better picture of the cosmic landscape. We may unveil — a) How far does the black hole mass function extend? b) How are compact binaries formed in the cosmos? c) Are there middle sized black holes still to be detected? d) What is the maximum mass for a stellar origin black hole?

The current catalog of GW sources has already revolutionized our understanding by putting constraints on fundamental theories of gravity . As the current and future ground-based detectors continue to search for high-frequency signals (with bandwidth

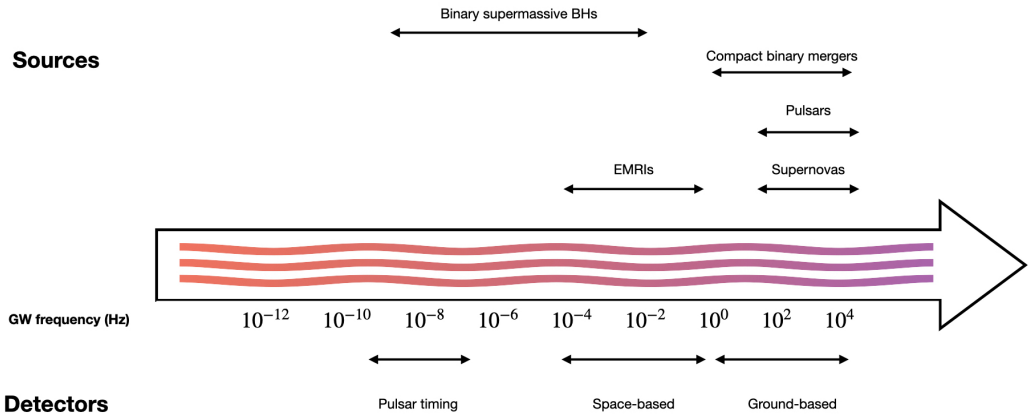

Fig. 1.5 GWs spectrum depicting different sources on basis of frequency range.

of a few tens of Hz), the space-based interferometers (LISA, TianQuin, DECIGO) will explore the sources emitting GWs in the lower frequency range (mHz-deci Hz) [3–5]. In particular, LISA is planned to launch in 2034, and preparatory work is now ramping up to span the full spectrum of astrophysical GW sources. A potential source under this regime are massive BH coalescence resulting from galaxy mergers. Another promising source target for LISA is EMRIs, where a stellar-mass object (a few tens of solar masses) spirals into a massive black hole (a few million of solar masses). The estimated event rate of such binaries is about a few tens per year [23]. EMRIs will spend at least a year in the observable band before plunging, given the extremity in mass ratio. Therefore, the signals from such systems encode space-time information around the massive black hole and allow for incredibly precise tests of GR and other modified gravity theories [24, 25].

Furthermore, by observing galactic millisecond pulsars with radio telescopes, it is possible to use arrays of such pulsars as natural detectors in the nano-hertz gravitational band [26]. For these arrays, the most promising signals are derived from the stochastic background signals of inspiralling SMBH binaries, for which detection is expected within the next decade. Thanks to pulsar timing arrays and space-based detectors, the gravitational spectrum can be observed nearly completely (see Fig. 1.5).

1.1 Chapter Synopses

We provide an elementary overview of GW astronomy in Chapter 2, with a strong focus on its theoretical characteristics: the mathematical framework of GWs, their

generation, and interaction with test masses. Additionally, the working principle of ground and space-based interferometers is discussed, and respective target sources are listed. In the last section, a statistical analysis of detector data is presented.

In Chapter 3, we first discuss the importance of EMRIs and LISA science. To understand the orbital dynamics of such sources, we present the geodesic equations of Kerr space-time and fundamental frequencies. Further, the self-force interaction is discussed via the action-angle formalism showing that the dissipative piece of self-force is responsible for the inspiral motion of the object.

Chapter 4 describes the phenomena of transient resonances in EMRIs with a particular focus on the framework of self-force resonances. Additional origins of resonances arising from extrinsic and intrinsic deviation from the Kerr space-time in EMRI evolution are discussed in the last section.

In Chapter 5, we show the method used to obtain the metric of a tidally perturbed black hole. The chapter summarises in brief the three-step procedure showing the construction of the Newman-Penrose scalar and potential, which yields the metric perturbation on applying the Chrzanowski operator. This metric perturbation is the key element to study the impact of tidal resonances.

Chapter 6 introduces the concept/framework of tidal resonances and explores the impact of such resonances over the observable orbital parameter space. The results show that the dephasing caused in the waveform is in the observable regime of LISA for a large portion of orbital parameter space.

Chapter 7 examined the modeling of transient resonances in EMRIs. The resonance model introduced efficiently implements the impact of resonances in waveforms. Using this model and Fisher matrices, the parameter measurement precision and systematic bias are studied. The study carried out is crucial for modeling self-force resonances as well. Finally, concluding remarks and additional discussion of possible future research directions are given in Chapter 8.

Chapter 2

GW astronomy

With the remarkable discovery of GWs from compact binaries, the seed of GW astronomy has begun to bloom. The experimental aspect of GW astronomy is rich as it makes use of extraordinary techniques that allow us to measure displacements that were unachievable in the past. The theoretical aspect of GWs is also quite interesting, for it brings together different areas of physics, such as GR, astrophysics, and cosmology. This chapter intends to provide a brief review of Einstein's field equations and to introduce the concept required for the discussion of GWs. We use the geometrical language of GR to discuss GWs as opposed to field theory. While both descriptions are complementary on the fundamental level, the geometric description allows the interaction of GWs with the detectors to be easily and better understood.

2.1 A brief theoretical review of GWs

Here, we discuss how GWs arise from Einstein's general theory of relativity and what their properties are. As a first step, we will write the field equations in a weak field approximation, also known as the linearized gravity approximation which consists of expanding the equations around a near Minkowski (flat or slightly curved) metric. Based on the resulting wave equation, we can explore the basic properties of GWs (with the appropriate gauge) and evaluate how they are generated and how they interact with matter. Michele Maggoire influential work [21] is the source of our discussion here.

2.1.1 Linearized gravity

GR does not view space-time as a static and absolute entity, but rather presents fundamental equations of motion governing the dynamics of space-time. It also eliminated the notion of a preferred coordinate system or observer. As a result, gravity is not considered as a force between two massive objects, but rather as a curvature of space-time. The connection between the mass-energy content and resulting space-time curvature is derived by taking the variation of gravitational action (sum of Einstein-Hilbert and matter action) with respect to the metric tensor $g_{\mu\nu}$. The resulting relation is

$$G_{\mu\nu} \equiv R_{\mu\nu} - \frac{g_{\mu\nu}R}{2} = \frac{8\pi G}{c^4}T_{\mu\nu}. \tag{2.1}$$

The quantity $T_{\mu\nu}$ is the energy-momentum tensor, which accounts for the mass-energy content in a system. Whereas on the left-hand side, the Einstein tensor $G_{\mu\nu}$ includes a measure of the curvature through the Ricci tensor $R_{\mu\nu}$ and Ricci scalar R; they are functions of the metric tensor $g_{\mu\nu}$. A solution to these field equations is a metric tensor $g_{\mu\nu}$, describing a space-time geometry, whose curvature depends on the mass-energy content.

To understand the concept of GWs, we work in a much simpler setting called 'linearized or weak field equations.' When the gravity is weak, the space-time metric is very close to the flat Minkowski space-time. Thus, the metric can be decomposed into two parts — a flat Minkowski metric $\eta_{\mu\nu}$ plus a small perturbation $h_{\mu\nu}$:

$$g_{\mu\nu} = \eta_{\mu\nu} + h_{\mu\nu}, \tag{2.2}$$

such that $|h_{\mu\nu}| \ll 1$ and is symmteric. We use the Minkowski metric $\eta_{\mu\nu}$ and its inverse $\eta^{\mu\nu}$ to raise and lower the tensor indices such that we have $h^{\alpha\beta} = \eta^{\mu\alpha}\eta^{\nu\beta}h_{\mu\nu}$. The inverse of the space-time metric $g^{\mu\nu}$ to the first order in perturbation is given as,

$$g^{\mu\nu} = (\eta_{\mu\nu} + h_{\mu\nu})^{-1} = \eta^{\mu\nu} - h^{\mu\nu} + \mathcal{O}(h^2). \tag{2.3}$$

Notation: Greek indices, such as $\alpha, \beta, \ldots$ take the values $0 \ldots 3$, while the spatial indices are denoted by Latin letters, $i, j, \cdots = 1, 2, 3$. The signature for flat space-time metric is

$$\eta_{\mu\nu} = (-, +, +, +).$$

We use the two-step (broadly) procedure to derive Einstein's linearized field equation taking into account the above-mentioned approximations:

- To compute the $G_{\mu\nu}$ in terms of perturbation, the first step is to compute the Christoffel symbols defined as

$$\Gamma^{\rho}_{\mu\nu} = \frac{1}{2} g^{\rho\sigma}(\partial_\mu g_{\sigma\nu} + \partial_\nu g_{\sigma\mu} - \partial_\sigma g_{\mu\nu}).$$

- Next, Riemann curvature tensor is computed using the following definition

$$R^{\mu}{}_{\nu\rho\sigma} = \partial_\rho \Gamma^{\mu}_{\nu\sigma} - \partial_\sigma \Gamma^{\mu}_{\nu\rho} + \Gamma^{\mu}_{\alpha\rho}\Gamma^{\alpha}_{\nu\sigma} - \Gamma^{\mu}_{\alpha\sigma}\Gamma^{\alpha}_{\nu\rho}.$$

  Thereafter, the Ricci tensor and the Ricci scalar is obtained from the Riemann curvature tensor: $R_{\mu\nu} = R^{\alpha}{}_{\mu\alpha\nu}$ and $R = g^{\mu\nu}R_{\mu\nu}$.

$G_{\mu\nu}$ and $T_{\mu\nu}$ are symmetric tensors, this makes Einstein's field equation a set of non-linear partial differential equations of second order with 10 linearly independent variables. Further, the Bianchi identities reduce the number of independent equations from 10 to 6.

Keeping to the first order in the perturbation, we obtain the following expression for the Christoffel symbol,

$$\Gamma^{\rho}_{\mu\nu} = \frac{1}{2}\eta^{\rho\sigma}(\partial_\mu h_{\sigma\nu} + \partial_\nu h_{\sigma\mu} - \partial_\sigma h_{\mu\nu}). \tag{2.4}$$

The linearization of Reimann tensor gives,

$$R^{\mu}{}_{\nu\rho\sigma} = \partial_\rho \Gamma^{\mu}{}_{\nu\sigma} - \partial_\sigma \Gamma^{\mu}{}_{\rho\nu}. \tag{2.5}$$

On substituting the expression of linearized Christoffel symbol in above equation, the Reimann tensor reduces to,

$$R^{\mu}{}_{\nu\rho\sigma} = \frac{1}{2}(\partial_\rho\partial_\nu h^{\mu}{}_{\sigma} - \partial_\rho\partial^{\mu}h_{\nu\sigma} - \partial_\sigma\partial_\nu h^{\mu}{}_{\rho} + \partial_\sigma\partial^{\mu}h_{\nu\rho}). \tag{2.6}$$

Contracting the first and the third indices, we get the Ricci tensor

$$R_{\nu\sigma} = \frac{1}{2}(\partial_\mu\partial_\nu h^{\mu}{}_{\sigma} - \Box h_{\nu\sigma} - \partial_\sigma\partial_\nu h + \partial_\sigma\partial^{\mu}h_{\nu\mu}), \tag{2.7}$$

where $\Box = \partial_\mu\partial^\mu$ is the d'Alembertian operator in flat space-time and h is the trace of the metric perturbation defined as $h = h^{\mu}{}_{\mu}$. Contracting the indices again to obtain the Ricci scalar yields,

$$R = \partial_\mu\partial_\nu h^{\mu\nu} - \Box h. \tag{2.8}$$

So far, we have all the quantities needed to write the linearized form of Einstein tensor. Before that is useful to define a tensor called 'trace reverse' of perturbation. As the name implies, the trace of this tensor is $-h$.

$$\bar{h}_{\mu\nu} = h_{\mu\nu} - \frac{1}{2}\eta_{\mu\nu}h. \tag{2.9}$$

Given this definition and linearized form of Riemann tensor, it is now straightforward to write Einstein Tensor $G_{\mu\nu} = R_{\mu\nu} - g_{\mu\nu}R/2$ in linear form,

$$G_{\mu\nu} = \frac{1}{2}(\partial_\alpha\partial_\mu\bar{h}^\alpha{}_\nu + \partial_\alpha\partial_\nu\bar{h}^\alpha{}_\mu - \Box\bar{h}_{\mu\nu} - \eta_{\mu\nu}\partial_\alpha\partial_\sigma\bar{h}^{\alpha\sigma}). \tag{2.10}$$

The harmonic or Lorenz gauge is the generalization of the Lorenz gauge in electromagnetism, and consists of the 4 conditions

$$\partial_\nu\bar{h}^{\mu\nu} = 0. \tag{2.11}$$

We see that in this gauge the Einstein tensor simplifies to

$$G_{\mu\nu} = -\frac{1}{2}\Box\bar{h}_{\mu\nu},$$

so the Einstein field equations in the vacuum (*i.e.* $T^{\mu\nu} = 0$) is simplified to

$$\Box\bar{h}^{\mu\nu} = 0 \qquad \text{(outside the source)}. \tag{2.12}$$

On the basis of linearized theory, this equation shows that the trace-reversed metric perturbation propagates as a wave deforming a flat space-time. Since $\Box = (1/c^2)\partial_t^2 + \nabla^2$, the wave equation implies that GWs travel at the speed of light. It has the solution of the form called a plane wave solution.

$$\bar{h}^{\alpha\beta} = A^{\alpha\beta}\exp(ik_\alpha x^\alpha), \tag{2.13}$$

where $A^{\alpha\beta}$ is called the amplitude tensor and k_α is the propagation four vector. Using the Lorentz gauge condition and plane wave solution of field equation, we get

$$k^\alpha k_\alpha = 0, \qquad A^{\alpha\beta}k_\beta = 0. \tag{2.14}$$

implying that k^α is a null vector and amplitude tensor is transverse to the propagation vector k_β. The tensor $A^{\alpha\beta}$ is symmetric since $\bar{h}^{\alpha\beta}$ is symmetric. The four constraints

on the ten independent components of $A_{\alpha\beta}$ arise from the Lorenz condition (2.14). The remaining four constraints come from the left-over gauge fixing as follows. We choose the standard TT gauge by imposing the three spatial conditions and the trace-free condition

$$A^{0i} = 0, \qquad \mathrm{tr}(A) = 0. \tag{2.15}$$

This leaves two dynamical degrees of freedom in $A^{\alpha\beta}$ that correspond to two possible polarization of GWs in GR . In matrix form, we can write the amplitude as (assuming we orient our spatial coordinate axes such that the GW is travelling in the positive z-direction),

$$A^{TT}_{\alpha\beta} = \begin{bmatrix} 0 & 0 & 0 & 0 \\ 0 & A_{11} & A_{12} & 0 \\ 0 & A_{12} & -A_{11} & 0 \\ 0 & 0 & 0 & 0 \end{bmatrix} \tag{2.16}$$

As a result, the metric perturbation in this gauge reduces to its transverse and traceless part, h^{TT}_{ab}. The only non-zero component of the metric perturbation are the plus (+) and the cross (x) polarization of GWs such that,

$$\bar{h}^{TT}_{11} = -\bar{h}^{TT}_{22} \equiv h_{+}; \quad \bar{h}^{TT}_{12} = -\bar{h}^{TT}_{21} \equiv h_{\mathrm{x}}. \tag{2.17}$$

2.1.2 GWs generation in linearised theory

The framework for the generation of radiation is greatly simplified if the velocities inside the source are non-relativistic. In a non-relativistic system, for a source with size R, the reduced wavelength of the radiation generated is much bigger than the size of the system. Morever, we are interested in the value of h^{TT}_{ij} at large distance from the source where the detector is located (far field solution), say at distance r. Combining the two approximations we get

$$R \ll \lambda \ll r.$$

On neglecting the internal motions of the source, we have

$$\bar{h}^{\alpha\beta}(t, x) \sim \frac{4G}{c^4 r} \int T^{\alpha\beta}(t - r/c, x')\, d^3x'. \tag{2.18}$$

On switching to TT gauge, we only need to compute the spatial components of the trace-reversed metric perturbation. Following the conservation laws and ignoring the

boundary terms, the above expression reduces to

$$\bar{h}^{ij}(t,x) \sim \frac{2G}{c^4 r}\frac{\partial^2}{\partial t^2}\int x'^i x'^j\, T^{00}(t-r/c,x')\, d^3x'. \tag{2.19}$$

Defining the quadrupole tensor,

$$I^{ij}(t) = \int x'^i x'^j\, T^{00}(t-r/c,x')\, d^3x', \tag{2.20}$$

our solution in TT gauge is

$$\bar{h}^{TT}_{ij}(t) \sim \frac{2G}{c^4 r}\,\ddot{I}^{TT}_{ij}(t-r/c). \tag{2.21}$$

with

$$I^{TT}_{ij}(t) = P_{ik}I^{kl}P_{lj} - \frac{1}{2}P_{ij}P^{kl}I_{kl}, \tag{2.22}$$

and the transverse projector operator being

$$P_{ij} = \delta_{ij} - \hat{n}_i\hat{n}_j, \tag{2.23}$$

where $\hat{n}_i = x^i/r$ is the unit vector in the propagation direction and overhead dot denotes the time derivative. From the equation (2.21), we see that the lowest-order radiation emitted is quadrupolar in nature, *i.e.*, generated by a time-varying mass quadrupole moment. In the multipole expansion, the leading order term is mass quadrupole. GWs do not have monopole or dipole radiation. The monopole term depends only on the mass M, and the dipole term depends on momenta $P^i \sim \int d^3x\, T^{0i}(t,x)$. Due to the conservation of mass and the total momentum of the source, the monopole and dipole terms do not contribute to radiated GWs.

GWs carry energy and angular momentum at the expense of energy and angular momentum of the source. The total radiated power (P) and angular momentum (J) in quadrupole approximation are given as [27]

$$P_{\rm quad} = \frac{G}{5c^5}\Big\langle \dddot{I}_{ij}\,\dddot{I}_{ij}\Big\rangle, \tag{2.24}$$

$$\left(\frac{dJ^i}{dt}\right)_{\rm quad} = \frac{2G}{5c^5}\epsilon^{ikl}\Big\langle \dddot{I}_{ij}\,\ddot{I}_{ij}\Big\rangle, \tag{2.25}$$

where the angular brackets correspond to averaging over several orbits and ϵ^{ikl} is the Levi-Civita tensor.

2.2 Effect of GWs and detection principles

The equation of motion of a test particle in a background metric $g_{\alpha\beta}$ can be derived from geodesic equation,

$$\frac{d^2x^\alpha}{d\tau^2} + \Gamma^\alpha{}_{\mu\nu}\frac{dx^\mu}{d\tau}\frac{dx^\nu}{d\tau} = 0. \tag{2.26}$$

where x^α represents the coordinates of the particle and τ is the *proper* time measured by a clock carried along the trajectory. In the TT gauge, GWs have a particularly simple form. We define the corresponding frame as the TT frame, and calculate the initial acceleration of the particle using the geodesic equation. If the test mass is at rest at $\tau = 0$, we find

$$\frac{d^2x^i}{d\tau^2} = -\left[\Gamma^i{}_{00}\left(\frac{dx}{d\tau}\right)^2\right]_{\tau=0}, \tag{2.27}$$

where

$$\Gamma^i{}_{00} = \frac{1}{2}(2\partial_0 h_{0i} - \partial_i h_{00}). \tag{2.28}$$

In the TT gauge, however, this quantity disappears because both h_{00} and h_{0i} are set to zero. As a result, in linearised gravity and the TT frame particles remain at rest even after the wave arrives. It does not mean that GWs have no physical impact. Rather, such effects can be determined by monitoring the *proper* distances or *proper* times.

Consider two events at $(t, x_1, 0, 0)$ and $(t, x_2, 0, 0)$ in the TT gauge. The coordinate distance $x_2 - x_1 = L$ remains unchanged even after the passing of GW. However, the *proper* distance between these two events (upto linear order and assuming propagation direction as z-axis) is

$$s \sim L\,[1 + \frac{1}{2}h_+ \cos(\omega t)]. \tag{2.29}$$

Thus the proper distance changes periodically in time because of the passing GW. The time evolution of a ring of free-falling test particles under the influence of h_+ and h_x mode is shown Fig 2.1. The proper distance is what determines the time it takes for light to travel back and forth between the two test masses (mirrors), and so the fact that GWs affect the proper distance means that they can be detected by measuring the round trip time. This is the bottom line of the detection principle used in our interferometric detectors discussed in the following subsections.

2.2.1 Ground-based and spaced-based interferometers

All our knowledge of the cosmos came from neutrinos and EM radiation in the past. Until the 1930s, visible light was the only form of astronomy that provided a serene

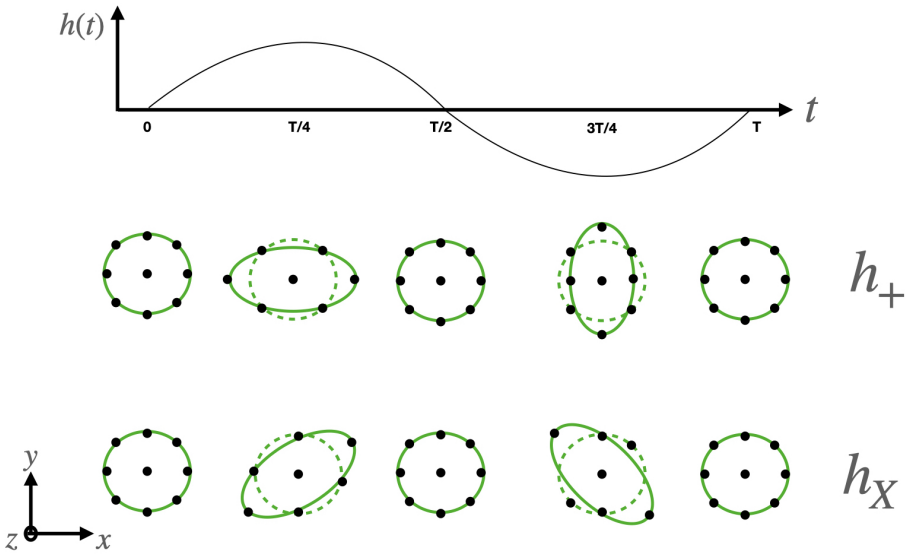

Fig. 2.1 The displacement of the test mass under the action of GW of plus (+) and cross (x) polarizations.

view of stars, planets, and galaxies. Edwin Hubble, an American astronomer discovered that our Universe is expanding by observing the nearby Nebulae and gave the famous Hubble's law [28]. With the advancement in technology, astronomers began observing different parts of the EM spectrum. Our view of the Universe has been revolutionized by the observation of active galaxies through radio and microwave astronomy. American astronomers, Arno A. Penzias and Robert W. Wilson discovered the cosmic microwave background radiation, which supports the big bang model and furthermore the isotropy and homogeneity of the universe through the later observations by COBE, WMAP and Planck spacecraft [29–31]. Observing new wavelengths of light can lead to revolutions in astronomy, and so what do we expect when we see an entirely new GW spectrum?

Joseph Weber, an American physicist proposed a method of measuring the energy radiated by binary stars in 1960. After working on the proposal for several years, he finally built an antenna to detect waves in 1966. A five-foot-long, two-foot-diameter aluminum solid cylinder weighing 3000 pounds was chosen for the work. The cylinder was suspended in a vacuum chamber with a wire wound around its circumference to isolate it from external disturbances. The length was calculated to match the frequency of about 1000 cycles per second, targeted at a supernova gravitational collapse, which is supposed to produce gravitational waves. The concept was to produce a 'ring' lasting for a certain duration as waves hit the cylinder analogous to the kind of ring in tuning fork. In 1969, Weber published detection results of his apparatus (came to be known as

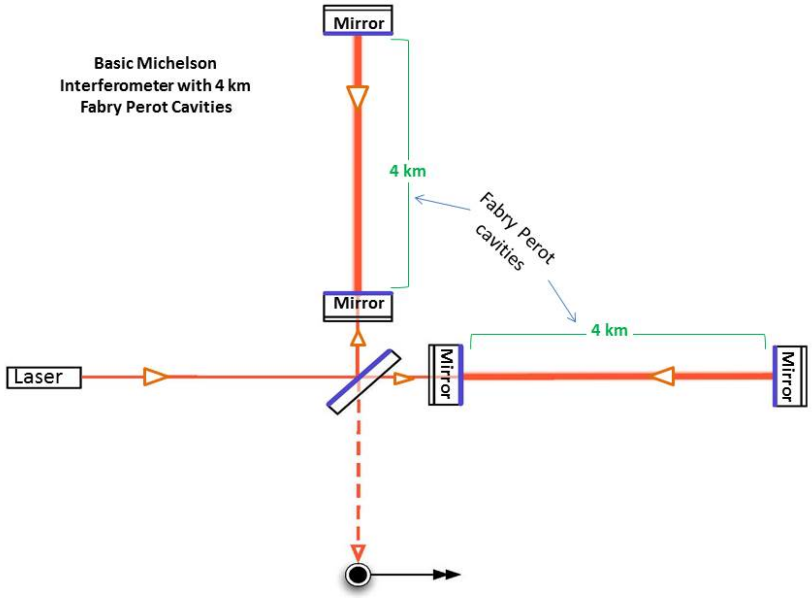

Fig. 2.2 Schematic design of ground-based LIGO detector. Image courtesy: Caltech/MIT/LIGO Laboratory (open gallery).

Weber bars) claiming 17 coincidence events from two of his detectors built separately within the range of 1000 km. He observed anisotropy of more than 6σ in GW intensity with peaks in the direction of galactic center. This created a stir in the community as it implied massive scale conversion of mass into energy within the galaxy and hence lack of matter to gravitationally bound it. After a few attempts, observations were found to be unaccommodating and soon lost integrity. Nevertheless, the lack of a sounding apparatus to explain theoretical studies prompted several groups to improve upon Weber's observations by designing their own detectors. Fortunately, the discovery of indirect GWs in 1974 made by Hulse and Taylor revived interest in the detection of waves [16].

In the 1980s, a project for the first ground-based kilometer-scale gravitational wave interferometer was proposed by a joint effort of eminent physicists. The initial run of LIGO lasted from 2002 to 2010 with no detections. The instrument design was improved over the years and is called Advanced LIGO (aLIGO). LIGO is an engineering marvel with the practical idea suggested by Rainer Weiss at MIT. LIGO's observatories are technically interferometers mainly comprised of a mirror, detector and two laser beams (schematic design shown in figure 2.2). When the crest of two waves

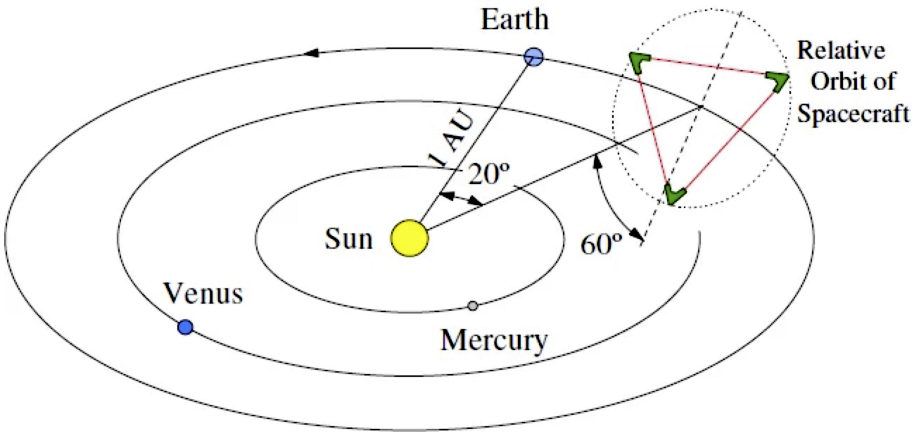

Fig. 2.3 Schematic Design of spaced-based LISA orbit.

of light overlap, they unite to form a constructive interference pattern. In contrast, when the peak of one light wave overlaps with the trough of another, the two waves create destructive interference. In LIGO, the high-power lasers bouncing back between the arms cancel each other entirely. However, if a gravitational wave happened to pass through the LIGO observatory, it would induce curvature in space-time fabric and thus stretching one detector arm and compressing the other, throwing off this destructive interference — making light reach the photo-detector. It also explains why LIGO detectors are 'L' shaped. This interference pattern of light signal would provide data about the changes the arms experienced and thus unveil features about the gravitational wave event and their source.

Ground-based interferometers such as LIGO (USA), Virgo (Italy) and KAGRA (Japan) observe high frequency GWs, but to detect low frequencies, we'll need an extremely quiet area sheltered from any disturbances — even the tiny gravitational waves generated by flies! To further explore the Cosmos, NASA and the ESA is jointly working to develop LISA, a constellation of three satellites that would form a triangular interferometer with three 2.5 million-kilometer arms. The cluster would be placed in an Earth-like orbit at a distance of 1 AU from the Sun, 20° behind the Earth and inclined at 60° to the ecliptic. The schematic heliocentric orbit is shown in Fig 2.3. LISA will focus on low-frequency (mHz) range and is expected to launch in the 2030s. For exploring sources at a lower frequency than LISA bandwidth, NANOGrav (or PTA) uses the Galaxy itself to detect gravitational waves with the help of objects

called pulsars — exotic stars that send out pulses of radio waves with extraordinary periodicity. Figure 1.5 shows the the target sources of operating ground-based and future space-based detectors.

2.2.2 Target source overview

Here we list some of the prospected high and low-frequency GW sources (also see Fig. 1.5). The **sources of the high-frequency universe**, observed with ground-based detectors at frequencies between 10 Hz to a few kHz can be classified as [32]:

- **Compact binary coalescence**: CBCs comprise of binary neutron star, binary black hole and black hole-neutron star binaries. CBCs are transient sources as they can last for a fraction of seconds or a few minutes (depending on the parameters) in the ground-detector bandwidth. At design sensitivity aLIGO can detect neutron star binaries out to a distance of $\sim$ 400Mpc, and black hole binaries out to $\sim$ 10Gpc.

- **Continuous-wave sources**: Sources producing continuous waves are generally steady, producing signals with roughly constant amplitudes and frequencies over the observation period. In particular, more than 2000 radio pulsars have been discovered with precise location and frequency measurements. Some of them have spin frequencies above 20 Hz, making them accessible to aLIGO and Virgo.

- **Unmodelled Bursts**: refer to short-duration events caused by a sudden change of state in the source that does not have well-modeled waveform templates such as pulsar glitches [33]. Glitches are mystifying spin-up events seen in mostly relatively young neutron stars such as Crab and Vela. During a glitch there is a sudden increase in the rotational frequency of a pulsar. Such events are likely to be within reach of ET (future underground detector), but still too weak for aLIGO and Virgo sensitivity. Another exciting source falling in this category is the Core collapse supernovae (CCSNae). Violent dynamics in CCSNae are expected to generate low amplitude, short-duration, bursts of gravitational waves over a wide frequency range, from 50 to 1000 Hz, if they are aspherical. Due to the richness of the input physics accompanied by the infall of matter and its bounce, gravitational wave bursts do not have universal characteristics. The EM observations of CCSNae might reveal secondary observables such as ejecta composition, mass, and progenitor type. GWs, on the other hand, are emitted

from the core of the CCSN and can therefore provide direct, live insight into the dynamics of the collapse and bounce of the core.

- A **stochastic background** can arise from a large number of weak sources so that there are many signals of comparable strength with overlapping frequencies within every resolvable frequency bin. Such background can also result from the primordial gravitational waves produced at the inflation era [34].

The **sources of the low-frequency universe**, observed with space-based detectors at frequencies between mHz to 0.1Hz can be listed as [32]:

- **Massive black hole coalescence** are binaries resulting from the merger of galaxies and are detected at the time of their coalescence out to luminosity distance of around 230 Gpc. Hence, the upcoming LISA-like observatories will therefore provide an extremely complete census of such massive objects throughout the universe.

- Some of the most important sources for LISA will be the capture orbits of stellar-mass compact objects into the massive black holes that reside in galactic nuclei. These are known as **EMRIs**. The observation of even a single such source can significantly advance our understanding of massive black holes, their stellar environments, or even the true theory of gravitation itself. These sources will be the focus of the next chapter as well as the work discussed in this thesis.

2.3 Basics of data analysis in a nutshell

In GW strain observations, it is not uncommon for the SNR from laser interferometers to be low, due to the high levels of instrumental and environmental noise. A template filter generated from waveform models can, however, be applied to the data in order to increase the SNR. The output of any real detector is a combination of noise and GW signal such that,

$$s(t) = h(t) + n(t). \tag{2.30}$$

The noise $n(t)$ in the detectors is ideally stationary and Gaussian, but the characteristics are the same. Under these assumptions, the probability of a particular realization of stationary and Gaussian noise process $n(t)$ can be concisely written as,

$$p_n[n(t)] \propto e^{-(n,n)/2}. \tag{2.31}$$

The notation of curly brackets stand for noise-weighted inner product defined as,

$$\langle a|b\rangle := 4\,\mathrm{Re}\int_0^\infty \frac{\tilde{a}(f)\tilde{b}^*(f)}{S(f)}\,df, \tag{2.32}$$

where $S(f)$ is the one-sided power spectral density of the noise and $\tilde{a}(f)$ is the Fourier transform of the signal $a(t)$. A matched filter is a process that involves cross-correlating a signal h with some optimal template filter $K(t)$ that maximizes the output SNR. It is defined as,

$$\frac{S}{N} = \frac{\int_{-\infty}^{\infty} df\,\tilde{h}(f)\tilde{K}^*(f)}{[\int_{-\infty}^{\infty} df\,(1/2)\,S(f)\,|\tilde{K}(f)|^2]^{1/2}}. \tag{2.33}$$

In the above equation, we are assuming, based on the theoretical model, we already know what GW signal we are looking for. The technique is called matched filtering because the filter is chosen to 'match' the signal we are searching for. In LIGO-Virgo detectors, this technique is heavily used for detecting signals from raw data. In both signal detection and parameter estimation, the principle of comparing detector data with many templates and identifying the best match is used. The generating waveform model should be as accurate as possible otherwise the SNR could be greatly reduced. Considering the large number of templates needed in both procedures, it must also be computationally efficient. There are different strategies for detection and parameter estimation. Detection is a global search over the parameter space of the model, and parameter estimation explores (along a more localized region) the likelihood that the template-subtracted data will be consistent with detector noise.

We define two quantities which serve as a measure of similarity between two template waveforms $h_a(t)$ and $h_b(t)$, the Overlap $\mathcal{O}(h_a, h_b)$ and Mismatch $\mathcal{M}(h_a, h_b)$, by

$$\mathcal{O}(h_a, h_b) = \frac{\langle h_a|h_b\rangle}{\sqrt{\langle h_a|h_a\rangle\langle h_b|h_b\rangle}} \tag{2.34}$$

$$\mathcal{M}(h_a, h_b) = 1 - \mathcal{O}(h_a, h_b). \tag{2.35}$$

If $\mathcal{O}(h_a, h_b) = 1$, the two waveforms are identical. Waveforms with $\mathcal{O}(h_1, h_2) = 0$ are mutually orthogonal. In contrast, by definition, the smaller $\mathcal{M}(h_a, h_b)$, the better the match is. In addition to waveform models, the detection pipelines also incorporate generic search techniques. This usually involves identifying excess power in spectra of the data, which is a time-frequency plot of the power spectrum density of short-term sources, and they are also useful for detecting transient sources, such as burst sources. GW astronomy is likely to evolve to include modern statistical techniques such as deep

neural networks [35, 36] in addition to or as a substitute for the standard detection algorithms based on template banks.

Chapter 3

Orbital dynamics in Kerr space-time

Since the discovery of the Kerr solution, the mathematics of the Kerr black hole has been well studied and understood. Moreover, it has wide astrophysical relevance and plays an important role in the mathematical problems of general relativity. An approach to understanding space-time around a Kerr BH is to examine the orbital dynamics in this background. Chandrashekar [10] presents a comprehensive summary of the Kerr geodesics.

Newton's gravity is particularly effective in explaining the motion of a test mass in weak fields. The resulting Keplerian orbits are quite simple with a conserved total energy E (due to time translation symmetry) and a conserved orbital angular momentum $\boldsymbol{L}$ (due to rotational invariance) which leads to a planar motion. Bound orbits are exactly periodic and are characterised by the azimuthal frequency. When the field is strong, the bound orbits become complicated and are no longer periodic: the deviation of the potential from the inverse-distance law produces the relativistic precession effect, whose observational imprint on Mercury's perihelion advance became a legendary example of validating GR theory during its infancy.

We introduce Kerr geodesics in this chapter and describe the notation and conventions we use. Also discussed are the Kepler orbital elements and their associated frequencies. We will then examine the gravitational self-force, the dissipative portion of which leads to orbit shrinkage and thereby to the emission of GWs. This allows one to compute GWs from binary systems containing a compact stellar mass object moving around a supermassive primary BH, so-called extreme-mass-ratio inspirals. The following sections summarise why EMRIs are particularly rewarding target sources for LISA and the event rate.

3.1 Importance of extreme-mass-ratio inspirals

We have already gained a modest catalog of sources from the current network of ground-based detectors that has greatly increased our understanding of black holes and neutron stars, and strengthened our confidence in Einstein's general theory of relativity. Now, preparation is in full swing for a new generation of observatories that will cover the full range of astrophysical GW sources. Millihertz signals are particularly abundant in this spectrum, which includes EMRIs and late-stage events involving massive black holes binaries. Scientists will have access to the millihertz GW sky only via space-based detectors such as LISA, the third large-class mission in ESA's Cosmic Vision program, scheduled to launch in 2034. In particular, a typical EMRI is expected to spend more than a year in observational band and undergoes $\sim 10^5$ orbital cycles around the central massive black hole, *i.e.*, about 10^6 radians in gravitational-wave phase. There are two independent channels to form an EMRI. The "traditional" channel operates through scattering and capture processes. These can put stellar-mass objects in galactic nuclei close enough to the central massive BHs in galactic centers for the object to be gravitationally bound to the SMBH [24, 23, 37–40]. Recently, an alternative formation channel for EMRIs around accreting massive black holes has been proposed [39, 40] and is referred to as the wet formation channel. In this channel, stellar-mass black holes (and stars) on inclined orbits are captured by the accretion disk, and migrate under the influence of density wave generation towards the central SMBH [41]. Despite the fact that roughly 1% local galaxies and 10% high-redshifted galaxies have active galactic nuclei [42, 43], this wet EMRI formation channel is fairly efficient and expected to be equally important (if not more important) as the traditional channel. The two formation scenarios have distinct characteristics: EMRIs formed in the dry environment of traditional capture channels are expected to have higher eccentricities and higher inclinations than EMRIs formed in the wet environment of accretion disks when they enter the LISA band. For this reason, capture channels are particularly interesting for our work as asserted in the following chapters. EMRI event rate is determined by a combination of several uncertain parameters like the stellar distribution surrounding the SMBH, spin distribution of the central SMBH, and the formation scenario. According to the Monte-Carlo study of [44], the number of EMRIs detected by LISA is likely to be $\mathcal{O}(10) - \mathcal{O}(10^3)$ per year at an SNR of 20.

The orbit of the compact object can exhibit high eccentricity or extreme precession since it occurs deep in the strong gravitational field of the central black hole; this endows EMRI signals with rich harmonic content. Efforts to solve the EMRI inverse problem are well motivated by the scientific payoff of a successful observation [45]. One

of the main goals of LISA is: Space-time geodesy — testing the no-hair theorem which states that every black hole is fully described by just three quantities: its mass, spin and charge [46]. All other properties (hairs) are lost during the formation process. In particular for a Kerr BH with mass M and spin parameter a, so that all higher mass multiples moments M_l and spin multipoles S_l are fixed in terms of M and a by

$$M_l + i\, S_l = M\,(ia)^l.$$

The exterior vacuum space-time of any stationary, axi-symmetric body is specified by mass and current moments. These moments tell us how fields constructed from a metric fall off with distance and their angular dependence. GWs from EMRIs will be used to infer these moments, and if inconsistency is found between the observed and predicted multipole moments, that object cannot be a BH or may signal the impact of environment near EMRI system. EMRIs can be used to detect deviations of the quadrupole moment from that predicted by the Kerr geometry, at the level of 0.1% [47].

The precision of measurements made with EMRI signals has unmatched potential in astrophysics, cosmology, and the study of fundamental physics. The detection of EMRIs will complement electromagnetic astronomy in probing the formation rates and evolution scenarios of massive black holes, as well as serve as standard sirens for studying the expansion history of the Universe.

3.2 Orbital dynamics

3.2.1 The metric and geodesic equations

In Boyer-Lindquist coordinates (t, r, θ, ϕ), the Kerr metric is written as,

$$ds^2 = -\left(1 - \frac{2Mr}{\Sigma}\right) dt^2 - \frac{4a\sin^2\theta Mr}{\Sigma} dt d\phi + (\varpi^4 - \Delta a^2 \sin^2\theta)\frac{\sin^2\theta}{\Sigma} d\phi^2 + \Sigma d\theta^2 + \frac{\Sigma}{\Delta} dr^2,$$

where

$$\Sigma \equiv r^2 + a^2\cos^2\theta\,, \tag{3.1a}$$

$$\Delta \equiv r^2 + a^2 - 2Mr\,, \tag{3.1b}$$

$$\varpi \equiv \sqrt{r^2 + a^2}\,, \tag{3.1c}$$

and M, a are the black hole mass and spin parameter. For the remainder of this section we use natural units with $G = c = 1$. We first summarise the generic geodesic motion

in Kerr spacetime [48–51]. Consider a point-like body of mass μ orbiting a Kerr black hole described by mass M and spin parameter a. We use Boyer-Lindquist coordinates $\{t, r, \theta, \phi\}$ and Mino time λ to describe the geodesic equations:

$$\left(\frac{dr}{d\lambda}\right)^2 = \Big[E(r^2+a^2) - aL_z\Big]^2 - \Delta\Big[r^2 + (L_z - aE)^2 + Q\Big]$$
$$\equiv R(r)\,, \tag{3.2a}$$
$$\left(\frac{d\theta}{d\lambda}\right)^2 = Q - \cot^2\theta L_z^2 - a^2\cos^2\theta(1-E^2)$$
$$\equiv \Theta(\theta)\,, \tag{3.2b}$$
$$\frac{d\phi}{d\lambda} = \Phi_r(r) + \Phi_\theta(\cos\theta) - a\,L_z\,, \tag{3.2c}$$
$$\frac{dt}{d\lambda} = T_r(r) + T_\theta(\cos\theta) - a\,E\,. \tag{3.2d}$$

The quantities E, L_z, and Q are the orbital energy (per unit μ), axial angular momentum (per unit μM), and Carter constant (per unit $\mu^2 M^2$), respectively. Here, the Mino time parameter λ is related to proper time τ by $d\lambda = d\tau/\Sigma$. The explicit forms of functions in Eqs. (3.2c) and (3.2d) can be found, e.g., in Fujita & Hikida's paper, Ref [51].

By introducing λ the radial and angular equations of motion are completely decoupled as can be seen in Eqs. (3.2a) and (3.2b). Therefore, for a bound orbit, radial motion $r(\lambda)$ and angular motion $\theta(\lambda)$ become periodic functions with Mino-time periods $\Lambda_r, \Lambda_\theta$ defined as [51],

$$\Lambda_r = 2\int_{r_\mathrm{p}}^{r_\mathrm{a}} \frac{dr}{\sqrt{R(r)}}\,, \quad \Lambda_\theta = 4\int_{\theta_\mathrm{min}}^{\pi/2} \frac{d\theta}{\sqrt{\Theta(\theta)}}\,, \tag{3.3}$$

where r_a, r_p are the values of r at the apoapsis and periapsis respectively and θ_min is the minimum value of θ (measured from the black hole's spin axis). The motion in t and ϕ can be written as a sum of three parts: a linear term with respect to λ, an oscillatory radial part with period Λ_r, and an oscillatory angular part with period Λ_θ as follows:

$$t(\lambda) = t_0 + \Gamma_t\lambda + t_\lambda^{(r)} + t_\lambda^{(\theta)}\,, \tag{3.4}$$
$$\phi(\lambda) = \phi_0 + \gamma_\phi\lambda + \phi_\lambda^{(r)} + \phi_\lambda^{(\theta)}\,. \tag{3.5}$$

In the above equations, t_0 and ϕ_0 describe the initial conditions. The quantities Γ_t and γ_ϕ describe the frequency of coordinate time and ϕ with respect to λ, respectively,

which are given by [51]

$$\Gamma_t = \langle T_r(r)\rangle_\lambda + \langle T_\theta(\cos\theta)\rangle_\lambda + aL_z\,, \tag{3.6}$$

$$\gamma_\phi = \langle \Phi_r(r)\rangle_\lambda + \langle \Phi_\theta(\cos\theta)\rangle_\lambda - aE\,, \tag{3.7}$$

where $\langle \dots \rangle_\lambda$ represents the time average over λ.

The associated frequencies with Mino-time periods are given by

$$\gamma_{r,\theta} = \frac{2\pi}{\Lambda_{r,\theta}}\,. \tag{3.8}$$

The frequencies associated with distant observer time can be obtained by taking the ratio of the Mino-time frequencies to Γ_t:

$$\omega_{r,\theta,\phi} = \frac{\gamma_{r,\theta,\phi}}{\Gamma_t}\,. \tag{3.9}$$

Unlike Keplerian orbits, bound Kerr geodesics are triperiodic. The radial frequency ω_r is associated with oscillations in the radial direction. The polar frequency ω_θ is associated with oscillations in the θ direction, while the azimuthal frequency ω_ϕ describes the rotations around the central BH spin axis. The frequencies of the precessional motions of the periastron and the orbital plane are $\omega_r - \omega_\phi$ and $\omega_\theta - \omega_\phi$, respectively. As shown in Fig. 3.1, in the weak field regime, these three frequencies asymptote to the frequency predicted by Kepler's law whereas, in the strong field, they increasingly deviate from each other and evolve at different rates. Orbits are marginally stable at the separatrix and beyond this point, they become plunging orbits.

Besides the three constants of motion: $\{E, L_z, Q\}$, the Kerr geodesic orbit can be characterised by another set of parameters: the semi-latus rectum p, the orbital eccentricity e, and orbital inclination angle I. These parameters are defined by

$$p := \frac{2r_{\rm p}r_{\rm a}}{M(r_{\rm p}+r_{\rm a})}\,, \tag{3.10}$$

$$e := \frac{r_{\rm a}-r_{\rm p}}{r_{\rm a}+r_{\rm p}}\,, \tag{3.11}$$

$$I := \pi/2 - \mathrm{sgn}(L_z)\,\theta_{\rm min}\,. \tag{3.12}$$

For later convenience, we also introduce $x = \cos I$. To find the relation between the constants of motion $\{E, L_z, Q\}$ and orbital parameters $\{p, e, I\}$, one has to solve the

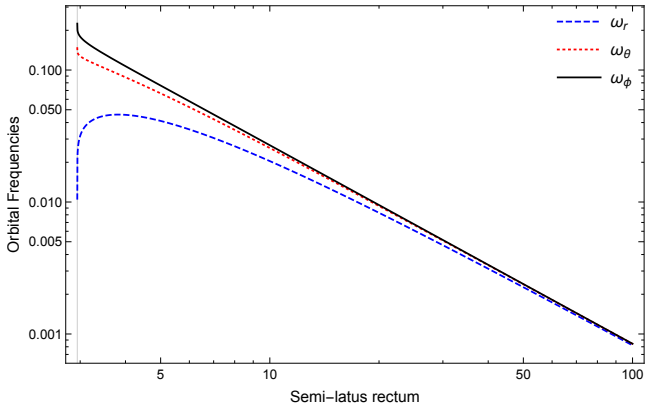

Fig. 3.1 Dimensionless fundamental frequencies as a function of semi-latus rectum for orbital eccentricity $e = 0.33$ and orbital inclination 30°. The spin parameter a of central massive BH is set to be 0.9. The vertical grey line marks the location of the separatrix.

following set of equations:

$$R(r) = 0\,, \tag{3.13}$$

$$\Theta(\theta) = 0\,. \tag{3.14}$$

The closed-form of the relation obtained after solving can be found in Ref. [49].

3.3 Dissipative effects

At leading order in mass ratio, the smaller body can be treated as a point-like particle moving along a geodesic orbit around the large black hole. At subsequent orders, a 'self-force' arises from the small body's interaction with its own gravitational perturbation that moves the orbit away from the geodesic of the Kerr spacetime [52–55]. The dissipative piece of the self-force is predominantly responsible for the inspiral, while the conservative piece shifts the orbital frequencies. In the following section, we review the action-angle formalism and use it to add the effect of self-force in the dynamical evolution equations.

3.3.1 Action angle formalism and gravitational self-force

An integrable system is one in which the Hamiltonian has the maximum number of mutually independent constants of motion. It follows that for a system of N degrees of

freedom, the Hamilton-Jacobi equations can be divided into N independent equations. Consider a system with N degrees of freedom, that is, a phase space consisting of N-dimensional positional vector $\vec{Q} = (Q^1, ..., Q^N)$ and a corresponding set of N conjugate momenta $\vec{P} = (P_1, ..., P_N)$. Hamilton's equations then read

$$\frac{\mathrm{d}\mathbf{Q}}{\mathrm{d}t} = \frac{\partial H}{\partial \mathbf{P}}, \quad \frac{\mathrm{d}\mathbf{P}}{\mathrm{d}t} = -\frac{\partial H}{\partial \mathbf{Q}}\,. \tag{3.15}$$

In the case of an integrable system, there exists a suitable choice of canonical coordinates, known as the action-angle variables, for which the new Hamiltonian is independent of the angle coordinates. Therefore, new momenta J_i are constants of motion and the new coordinates q_i vary linearly in time. Following the canonical transformation, the equations of motion reduce to

$$\dot{\boldsymbol{q}} \equiv \boldsymbol{\omega}(\mathbf{J}) = \frac{\partial H}{\partial \mathbf{J}}\,,\ \dot{\mathbf{J}} = -\frac{\partial H}{\partial \boldsymbol{q}} = 0\,. \tag{3.16}$$

For N pairs of action-angle variables, the orbits lie on N-dimensional invariant tori in the $2N$-dimensional phase space. If we consider an integrable system with two degrees of freedom, that is a 4-D phase space, we can express the motion as trajectories winding around a 2-dimensional torus. This is illustrated in Fig. 3.2. The orbits are visualized as trajectories wrapped around a two-dimensional torus with characteristic frequencies ω_1 and ω_2, associated with the angular advances q_1 and q_2. For rational values of ω_2/ω_1, the orbital trajectory will retrace its path, while for irrational values of ω_2/ω_1 a trajectory will fill the torus densely.

The geodesic equations in Kerr are integrable, *i.e.*, there exists one integral of motion for each degree of freedom. The integrability allows one to introduce a set of "action-angle" variables, such that the "angle" variables q_i parameterize a torus and the conjugate "action" variables J_i are functions of the constants of motion $\{E, L_z, Q\}$. This method is advantageous in obtaining the frequencies of Kerr orbits [49] and including deviations to the geodesic motion due to different forces. Thus, we rewrite the equations of motion in this formalism to describe the dynamics in (r, θ, ϕ) [56].

$$\frac{dq_i}{d\tau} = \omega_i(\boldsymbol{J}) + \eta g^{(1)}_{i,\mathrm{sf}}(q_\theta, q_r, \boldsymbol{J}) + O(\eta^2), \tag{3.17}$$

$$\frac{dJ_i}{d\tau} = \eta G^{(1)}_{i,\mathrm{sf}}(q_\theta, q_r, \boldsymbol{J}) + O(\eta^2)\,. \tag{3.18}$$

where $\eta = \mu/M$ denotes the mass ratio of EMRI. As can be seen from the above equations, at zeroth order (on short timescales $\sim M$), a particle with mass μ is well

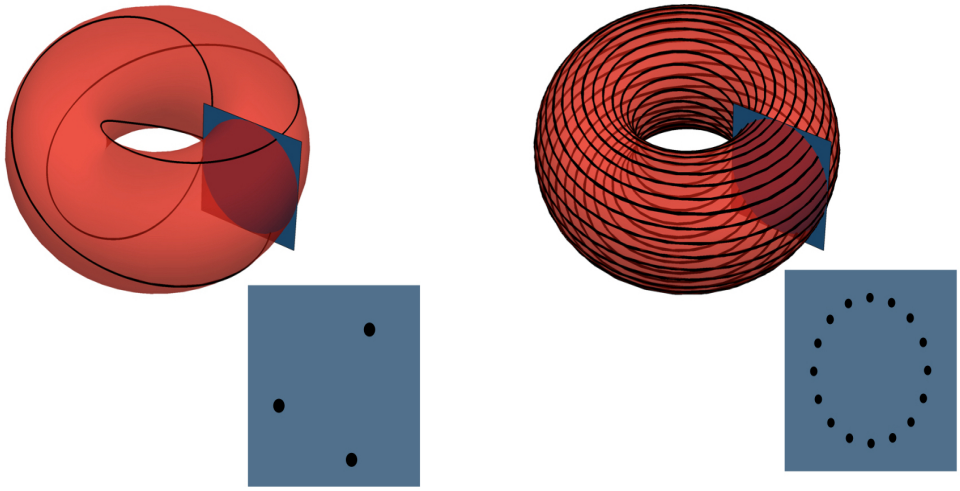

Fig. 3.2 Two panels show the intersections of phase-space trajectories (black) through a section surface (blue). The orbits stay on the torus defined by the action variables which are functions of integrals of motion (red). The left trajectory is resonant where the frequency of motion over the small circle of the torus is two-thirds of that over the large circle ($\frac{\omega_2}{\omega_1} = \frac{3}{2}$). The trajectory on right is non-resonant and it asymptotically trace out the whole cross-section of the torus.

approximated by a geodesic of the background space-time. At this order, action variables are conserved, and q_i increases at a fixed rate in time. However, in secular timescale ($\sim M/\eta$) the EMRI orbit deviates from geodesic motion due to the particle's self-force ($g_{i,\mathrm{sf}}$,$G_{i,\mathrm{sf}}$) [52–55]. The leading order self-force motion is an adiabatic inspiral. Over the longer timescale, it is necessary to consider various post-adiabatic corrections currently under development [57, 58].

For a slowly evolving orbit, we can take aid of frequency domain and express each component of the self force in terms of the underlying fundamental modes:

$$g^{\mu} = \sum_{k=-\infty}^{\infty} \sum_{n=-\infty}^{\infty} g^{\mu}_{kn} e^{-i(k\omega_\theta + n\omega_r)t} \,. \tag{3.19}$$

The azimuthal frequency does not appear in the above series because the Kerr space-time is axi-symmetric and hence does not depend on the axial position of the small object. As an orbit slowly evolves, both the Fourier components g^{μ}_{kn} and the frequencies themselves gradually change. From Eq. (3.19), we see that the impact of self-force is mainly given by a near-constant piece (g^{μ}_{00}). This is because, the rapidly oscillating terms with $k \neq 0$, $n \neq 0$ average to zero over multiple orbits, and the bulk of the self

interaction arises from 00 piece of the force. It is crucial to mention that some orbits may have commensurate fundamental frequencies such that $\omega_\theta/\omega_r = n/k$, where n and k are small integers. When this relation holds (namely, the self-force resonance condition), the phase term in Eq. (3.19) does not oscillate, and the corresponding Fourier amplitude contributes to the altering the orbital evolution. This breaks down the 'standard' adiabatic approximation. The next chapter focuses on the topic of orbital resonances.

3.3.2 Adiabatic inspiral

The self force can be broken into a conservative (time-symmetric) piece, and a dissipative (time-asymmetric) piece:

$$g^\mu = g^\mu_{\rm diss} + g^\mu_{\rm cons} \ . \tag{3.20}$$

Generally, the dissipative piece of the self-force drives energy and angular momentum from the binary, causing the binary to inspiral, and the conservative piece shifts the orbital frequencies from their geodesic values. When we consider the leading order, *i.e.*, in the adiabatic approximation, we neglect the conservative self-force, focusing instead on dissipative self-interactions.
Thus, the instantaneous rate of change of the conserved integrals can be expressed as:

$$\frac{dE}{dt} = -\xi^{(t)}_\mu g^\mu_{\rm diss} \ , \tag{3.21}$$

$$\frac{dL_z}{dt} = \xi^{(\phi)}_\mu g^\mu_{\rm diss} \ , \tag{3.22}$$

$$\frac{dQ}{dt} = 2Q_{\mu\nu}u^\nu g^\mu_{\rm diss} \ , \tag{3.23}$$

where E, L_z are related to the time-like and axial Killing vectors as: $E = -\xi^{(t)}_\mu u^\mu$, and $L_z = \xi^{(\phi)}_\mu u^\mu$. The quantity $u^\mu \equiv dz^\mu/d\tau$ is the 4-velocity of the small body. On the other hand the Carter constant Q is related to a Killing tensor: $Q = Q_{\mu\nu}u^\mu u^\nu$. These components can be written

$$\frac{d\mathcal{C}}{dt} = \dot{\mathcal{C}}_{00} + \sum_{\substack{k=-\infty \\ k\neq 0}}^{\infty} \sum_{\substack{n=-\infty \\ n\neq 0}}^{\infty} \dot{\mathcal{C}}_{kn} e^{-i\Phi_{kn}(t)} \ , \tag{3.24}$$

where $\mathcal{C}$ stands for E, L_z, or Q. The 00 components are separated to emphasize that these components survive the long-time averaging. The second term averages out due to the fast oscillation of phase term for non-resonant orbits.

For generic orbits, calculating the self-force directly can be challenging, especially in Kerr spacetime. Since the point mass limit causes the self field to diverge, practical calculations of the GSF will require a huge amount of time and computing resources. Therefore, PN expansions in the first-order black hole perturbation theory are primarily concerned with time-averaged dissipative forces that dominate the evolution of inspirals. For circular orbits and equatorial orbits, the 22PN calculation of the energy flux has been demonstrated in the Schwarzschild case [59] and the 11PN calculation in the Kerr case [60]. Additionally, PN formulae are presented for slightly eccentric and arbitrary inclined orbits up to the 5PN order, as well as the tenth-order correction of the eccentricity, which includes the effect of black hole absorption [61].

For the fast and qualitative computation of GWs, the scientific community relies on Kludge approximations [62]. Templates using the Kludge approximation might be useful as a search template in the first step of a hierarchical and multi-step search. Kludge templates have been used in EMRI studies for a long time. In the first kludge models, back-reaction effects were approximated using PN formulas [63]. The waveforms are based on Peters and Mathews decomposition and hence quadrupolar. However, there is a long-running program [64–67] aimed to improve the accuracy of the models using numerical data from self-consistent self-force calculations.

Chapter 4

Transient resonances in EMRIs

Systems with resonance islands lack sufficient conserved quantities due to non-integrability. Resonances have been examined in several papers, focusing on their role in astrophysics and black hole orbital dynamics [68–72]. In particular, the self-force resonances were studied in detail by Hinderer and Flanagan [73, 74], who developed the framework by coupling exact Kerr geodesics to a post-Newtonian self-force model. Based on their analysis, they found that resonant behavior near commensurate orbits significantly changes the evolution of a binary, by inducing a 'jump' in the orbit's conserved integrals compared to a study without resonance. To prepare for the upcoming low-frequency stage of GWs, we need our waveform models to be very accurate because gravitational wave observations rely on matched filtering techniques that are extremely sensitive to the phase of the gravitational waves emitted by the system. Accurate waveform modeling is not only required to extract the signal, but also a prerequisite to parameter estimation. Since the phase is directly related to the orbital evolution, it is necessary to take the resonant effects into consideration.

Using the two-timescale expansion [75], the orbital phase can be expanded with respect to the mass ratio $\eta = \mu/M$ (considering a body of mass μ orbiting an SMBH of mass M) as

$$\psi = \frac{1}{\eta}\left(\psi^{(0)} + \eta^{1/2}\psi^{(\mathrm{res})} + \eta\psi^{(1)} + O(\eta^{3/2})\right), \tag{4.1}$$

where $\psi^{(0)}/\eta$ denotes the orbital phase determined by the averaged dissipative piece of the first order self-force whereas $\psi^{(1)}$ denotes the post-adiabatic order derived from the remaining oscillatory piece of the first order self-force and dissipative piece of the second order self-force. Corrections to the phase due to resonance scale as the square root of the inverse of mass ratio. These corrections thus become large over an EMRI inspiral, dominating over post-adiabatic effects. Significant efforts focusing on the computation

of the self-force are made by the community to model EMRI waveforms [61, 76, 77]. While self-force calculations are tedious, resonances (both self-force and tidal) will further complicate this enterprise [78, 79, 6, 80]. Recent work has shown the impact of self-force resonances on parameter estimation, suggesting that parameter estimates of a resonant EMRI orbit are likely to be biased if resonances are not taken into account in waveform modeling [81].

The purpose of this chapter is to summarise the importance of transient resonances in modeling EMRIs. We discuss the observational signatures of the well-studied self-force resonances in the literature. Additionally, we briefly discuss different types of resonances (due to extrinsic and intrinsic deviations from Kerr) besides self-force resonances.

4.1 Framework of self-force resonance

When analyzing resonances it is useful to refer to characteristic timescales. We use coordinate time t which corresponds to the time measured by an observer at infinity. Translation to Mino time can be done with an appropriate factor of Γ_t (see Eq. (3.6)). We discuss scales of the orbital period T, the radiation reaction or inspiral timescale $\tau_{\rm rr}$, and the resonance timescale $\tau_{\rm res}$.

The simplest and shortest timescales are the orbital periods $T_r = 2\pi/\omega_r$, $T_\theta = 2\pi/\omega_\theta$ and $T_\phi = 2\pi/\omega_\phi$. The radiation reaction timescale, which is longest one in the physical setting is defined as

$$\tau_{\rm rr} = \frac{\mathcal{C}}{\dot{\mathcal{C}}}, \tag{4.2}$$

where an overdot denotes a derivative with respect to t and $\mathcal{C}$ stands for E, L_z, Q. This timescale sets the period over which there is a significant change in the frequencies and scales as $\tau_{\rm rr} \sim M/\eta$. As a result, using the adiabatic prescription is also possible because it means the trajectory moves slowly through different orbital parameters.

Another important time scale is the resonance duration $\tau_{\rm res}$. From the fact that the phase in Eq. (3.19) changes slowly during a resonance, we can estimate its scale. In particular, expanding the phase variable $q_{kn} := kq_\theta + nq_r$ in a Taylor series around the time at which the system encounters resonance, $\tau_{\rm res,0}$

$$q_{kn}(\tau) = q_{kn}(\tau_{\rm res,0}) + (k\omega_\theta + n\omega_r)(\tau - \tau_{\rm res,0}) + \frac{1}{2}(k\dot{\omega}_\theta + n\dot{\omega}_r)(\tau - \tau_{\rm res,0})^2 + \cdots . \tag{4.3}$$

The frequency and its derivative are evaluated at $\tau_{\rm res,0}$. For non-zero integers k, n, the second term $k\omega_\theta + n\omega_r = 0$ at $\tau_{\rm res,0}$. Thus, the duration of resonance is given by the

condition that the third term becomes $\mathcal{O}(1)$, *i.e.*,

$$\tau_{\rm res} \sim \sqrt{\frac{2}{k\dot{\omega}_\theta + n\dot{\omega}_r}} \sim M\sqrt{\frac{1}{\eta}}\,. \tag{4.4}$$

Hence, the resonance time scale is longer than the orbital time scale and shorter than the radiation reaction time scale.

We are only concerned with the radial ω_r and polar ω_θ frequency resonances for self-force resonances when it comes to their impact on orbital evolution. Due to the axisymmetric nature of spacetime, resonances with azimuthal frequency are irrelevant. Since the equations are the same for all values of axial angle, it does not matter where the small object is placed in ϕ for the EMRI to evolve. However, this does not mean that resonances with $m \neq 0$ are not relevant. Due to the preferential direction of gravitational waves, such resonances can cause small kicks to the binary system. As pointed out by [82], this is negligibly small for EMRIs, but could have some interesting consequences for systems with more equal masses.

An EMRI can pass through a resonance during the observationally relevant period. It can lead to a 'jump' in constants of motion relative to the adiabatic prescription. After spending hundreds of orbital cycles in the resonance region, the parameters of the inspiraling orbit are different from those calculated from an adiabatic evolution. Flanagan and Hinderer [73] gave an analytic expression for this deviation in the context of self-force resonances.

$$\Delta J_i = \eta \int_{-\infty}^{\infty} G_i^{(1)}(q_\theta, q_r, \boldsymbol{J}) d\tau = \eta \sum_{s=\pm 1} \sqrt{\frac{2\pi}{|\Gamma s|}} \exp\left[\mathrm{sgn}(\Gamma s)\frac{i\pi}{4} + is\chi\right] G^{(1)}_{i,sk,sn}(\boldsymbol{J})\,. \tag{4.5}$$

Here, $\chi = kq_{\theta 0} + nq_{r0}$ and $\Gamma = k\dot{\omega}_{\theta 0} + n\dot{\omega}_{r0}$, and the quantities q_{i0} and $\dot{\omega}_{i0}$ are phases and frequency derivatives evaluated at $\tau_{\rm res,0}$ respectively. The jump across the resonance is evaluated by summing over non-vanishing harmonics of the self force $G_{i,kn}$ after orbit averaging. In principle, s ranges over all integers but since low-order resonances are dominant we only sum over $s = \pm 1$. All the quantities are evaluated at resonance.

From Eq. (4.5), we see that the jump across resonance has sensitive dependence on the resonant phase, *i.e.*, χ. The "shape" of the resonant orbit is dependent upon the value of χ. Phase can make a significant difference in the appearance of orbits whose principal parameters (*i.e.*, E, L_z, Q) are the same. Thus, the driving force which alters the flux rate during a resonance depends on the phase at resonance. Thus, to model the radiative evolution across a resonance we must know the exact phase of the orbit as it

enters the resonance. This implies a crucial point — resonances pose a computational challenge because the adiabatic approximation erases phase information.

4.2 Different origins of resonances in EMRIs

Besides self-force, there can be other sources breaking the integrability of the Kerr spacetime. The origin can be an intrinsic deviation from the Kerr metric such that the solution obeys Einstein's field equations but is not a Kerr BH, or some exotic object deviating from Einstein's theory of relativity. The current theoretical models lack information about how massive BHs formed at the galactic center. Therefore, the nature of this supermassive object is an open and valid question. Motivated by this open issue, there are several works discussing possible observations which can guide us to the answer [68, 71, 70]. The approach to this problem is handled by the argument of *integrability*. If a system is integrable, it has at least as many conserved quantities as degrees of freedom. In principle, a non-integrable system exhibits chaotic behavior in its dynamical evolution. Recent work [71] focuses on a space-time that considers theoretical deviations from Kerr's description of dark compact objects. Hence, they categorize the supermassive object as "deformed-Kerr", which is integrable, and "non-Kerr", which is not integrable. The motion of the small object is studied in deformed-Kerr and non-Kerr space-time. At the level of orbital dynamics, the KAM and Poincare-Birkhoff theorems imply that for a non-integrable system, half of the resonant orbits remain stable while half become unstable. The main idea is that a non-integrable system will possess a scattered series of chaotic islands when the orbit is in resonance. When a small object passes through one of these islands, it undergoes an abrupt orbital evolution, leading to a sudden change (referred to as a "glitch") in GWs frequency. And suppose we observe this discontinuity in the frequency evolution of a waveform. In that case, it might hint toward a deviation from the general theory of relativity! The expected observation from non-Kerr sources is illustrated in Figure 2 of Ref. [71]. Note that while this is one of the possibilities, several other reasons/space-times (like an instrumental malfunction) that may mimic this erratic feature in the spectrogram. One such example that is the Manko-Novikov space-time. The Manko-Novikov space-time is an exact solution to the Einstein Field Equations that allows objects to be black hole-like, but with a multipole structure different from Kerr black holes. This space-time does not exhibit Carter symmetry.

On the other hand, the non-integrability can also be sourced by extrinsic deviations, *i.e.*, the environmental impact on EMRIs. One example of such deviation is the

presence of tidal perturbers near the galactic center. Due to the close perturber, the axi-symmetry of the Kerr space-time is broken. EMRIs may exist within noisy astrophysical environments, and their evolution can therefore deviate from the pure vacuum predictions of GR. My research investigates (discussed in the following chapters) the effect of nearby stellar-mass objects induced resonances on LISA GW sources that leave an observable print on the waveform.

Chapter 5

Tidally perturbed Kerr space-time

It is now possible to study BHs in a strong field regime with GW observatories. Astrophysical BHs are expected to be immersed in a sea of gravitational fields arising from external perturbations that will alter the metric of the background hole. Since there are no exact expressions for computing waveforms in such scenarios, perturbation theory is used to incorporate tidal effects. The goal of this chapter is to find an approximate analytic form of the metric of a rotating BH subjected to tidal field. This chapter summarises the work laid out in Ref. [83].

5.1 Slow-motion approximation

The analytic construction of the metric is carried out in a slow-motion approximation where the perturbations of the external universe are assumed to vary slowly. Consider a spinning BH of mass M with spin parameter a immersed in an external universe described by another object of mass $m_\star$ with the radius of curvature $\mathcal{R}$. To fulfill the slow-motion approximation, we need,

- The perturbation h_{ab} must be relatively small to the background g^B_{ab}.
- The perturbation must change slowly relative to the background, *i.e*, $\dot{h}_{ab}/h_{ab} \ll \Omega_H$.

where Ω_H is angular velocity of the BH horizon. The rotation timescale τ_H of the horizon is defined as

$$\tau_H = \frac{1}{\Omega_H} = \frac{2M^2}{a}\Big(1 + \sqrt{1-(a/M)^2}\Big). \tag{5.1}$$

To apply the slow-motion approximation, this time scale must be much shorter compared to that associated with changing the radius of curvature (determined by the external object $m_\star$) *i.e.*, $\tau_H/\tau_{\rm ext} \ll 1$. Thus, the condition is

$$M/\mathcal{R} \ll a/M, \tag{5.2}$$

given that $\tau_{\rm ext} \approx \mathcal{R}$. In terms of spinning BHs, this relation defines a well-defined slow-motion approximation. For later convenience, we also define the inner and outer horizon of BH as

$$r_\pm = M \pm (M^2 - a^2)^{1/2}. \tag{5.3}$$

5.2 The metric perturbation

For the construction of the full metric perturbation, first, the Newman-Penrose scalar (ψ_0) is constructed. Defining it as follows

$$\psi_0 = C_{abcd}\, l^a m^b l^c m^d, \tag{5.4}$$

where C_{abcd} denotes the Weyl tensor of the space-time, and l^a, m^a are the null tetrad vectors. The tetrad consists of four null vectors $(l, n, m, \bar{m})$ out of which l and m are real and m and $\bar{m}$ are complex conjugates of each other. The vectors satisfy the following orthogonality condition,

$$l \cdot m = l \cdot \bar{m} = n \cdot m = n \cdot \bar{m} = 0 \tag{5.5}$$

The explicit contravariant form in Kerr coordinates is given as,

$$\begin{aligned} l^a &= \left(2\frac{r^2+a^2}{\Delta}, 1, 0\frac{2a}{\Delta}\right), \\ n^a &= \left(0, -\frac{\Delta}{2\Sigma}, 0, 0\right), \\ m^a &= \frac{1}{\sqrt{2}(r + ia\cos\theta)}\left[ia\sin\theta, 0, 1, \frac{i}{\sin\theta}\right]. \end{aligned} \tag{5.6}$$

The Weyl tensor of the space-time is written in terms of the electric $\mathcal{E}_{ab}$ and magnetic $\mathcal{B}_{ab}$ tidal tensors of the external universe (which is completely arbitrary as long as the slow-motion approximation is satisfied), which are slowly varying functions of advanced time v. For instance, if the external matter is characterized by mass $m_\star$

with orbital velocity u at a distance d from the central black hole, the electric-type tidal tensor scales as $m_\star/d^3$ and magnetic-type tidal tensor scales as $m_\star u/d^3$.

Using the slow-motion approximation, we can calculate the metric perturbation by applying the Chrzanowski procedure [84] to ψ_0. In this calculation, two parts are involved: the computation of a potential (Ψ) and the determination of the metric perturbation (h_{ab}). In summary, we have a three-step process:

$$\psi_0 \quad \longrightarrow \quad \Psi \quad \longrightarrow \quad h_{ab}$$

Construction of the functional form of ψ_0

In the asymptotic regime ($r_+ \ll r \ll \mathcal{R}$), the Newman-Penrose scalar is written as

$$\tilde{\psi_0} \sim -\sum_m z_m(v)\ {}_2Y_2^m(\theta,\phi), \tag{5.7}$$

where the tilde is used to symbolise the asymptotic form of ψ_0 and ${}_2Y_2^m(\theta,\phi)$ represents the spin-weighted spherical harmonics. The quantities $z_m(v)$ in Eq. (5.7) determine the nature of tidal field arising from the external object $m_\star$. It is defined as $z_m(v) = \alpha_m(v) + i\beta_m(v)$, where $\alpha_m(v)$ are linear combination of the electric tidal tensors $\mathcal{E}_{ab}$ and $\beta_m(v)$ are linear combination of the magnetic tidal tensors $\mathcal{B}_{ab}$. For the analysis described in this thesis, we will be interested in quadrupole tidal perturbation ($l = 2, m = 0, \pm1, \pm2$) and static tidal field such that magnetic-type tidal tensors do not contribute to $z_m(v)$ (more details in Chapter 6). Therefore, we only show the form of $\alpha(v)$ below,

$$\begin{aligned}
\alpha_0(v) &= \mathcal{E}_{11}(v) + \mathcal{E}_{22}(v), \\
\alpha_{\pm1}(v) &= \mathcal{E}_{13}(v) \mp i\mathcal{E}_{23}(v), \\
\alpha_{\pm2}(v) &= \mathcal{E}_{11}(v) - \mathcal{E}_{22}(v) \mp 2i\mathcal{E}_{12}(v).
\end{aligned} \tag{5.8}$$

Ansatz for the explicit form of ψ_0 was constructed by Poisson using the asymptotic form [85]. It is given as,

$$\psi_0 = -\sum_m z_m(v) R_m(r) {}_2Y_2^m(\theta,\phi), \tag{5.9}$$

where $R_m(r)$ is an unspecified radial function that should satisfy $R_m(r) \to 1$ in the regime $r \gg r_+$. The point is to solve for $R_m(r)$ by inserting ψ_0 into the vacuum Teukolsky equation [86, 87], which yields a differential constraint for $R_m(r)$ as follows:

First, defining a scaled radial coordinate x as

$$x = \frac{r - r_+}{r_+ - r_-}. \tag{5.10}$$

In terms of this coordinate, the differential equation for $R_m(r)$ is written as,

$$\left\{ x(1+x)\frac{d^2}{dx^2} + [3(2x+1) + 2im\gamma]\,\frac{d}{dx} + 4im\gamma\frac{2x+1}{x(1+x)} \right\} R_m(x) = 0, \tag{5.11}$$

where $\gamma = a/(r_+ - r_-)$. On solving the differential equation, one can obtain the full expression for ψ_0 that carries the information of gravitational perturbations arising from the external universe. It is given by

$$\begin{aligned}\psi_0 = -\sum_m B_m x^{-2}(1+x)^{-2}\Bigg(1 &+ \frac{4}{2im\gamma - 1}x + \frac{6}{(2im\gamma-1)im\gamma}x^2 \\ &+ \frac{12}{(2im\gamma-1)im\gamma(2im\gamma+1)}x^3 \\ &+ \frac{12}{(2im\gamma-1)im\gamma(2im\gamma+1)(2im\gamma+2)}x^4\Bigg)\,{}_2Y_2^m(\theta,\phi)\,,\end{aligned} \tag{5.12}$$

where the notations are defined as,

$$B_m = A_m z_m(v), \tag{5.13}$$

$$A_m = -\frac{i}{6}m\gamma(1+im\gamma)(1+4m^2\gamma^2), \tag{5.14}$$

The final expression for ψ_0 only contains quadrupole tidal perturbation ($l = 2$) because the higher modes are smaller by a relative factor of $M/\mathcal{R}$.

The potential Ψ

The potential is constructed by the application of some differential operators on ψ_0.

$$\Psi = \frac{1}{576}\Delta^2(D^\dagger)^4[\Delta^2\bar{\psi_0}], \tag{5.15}$$

where the overbar stands for complex conjugation. Here, $\Delta = r^2 - 2Mr + a^2$. The quantity $D^\dagger$ is differential operator that is expressed in spherical Boyer-Lindquist coordinates (t, r, θ, ϕ) as

$$D^\dagger = \partial_r - \frac{a}{\Delta}\partial_\phi. \tag{5.16}$$

The Kerr coordinates $(v, r, \theta, \phi_{\rm K})$ are related to Boyer-Lindquist coordinates as follows:

$$\begin{aligned} dv &= dt + dr\left(\frac{2Mr}{\Delta} + 1\right), \\ d\phi_{\rm K} &= d\phi + dr\frac{a}{\Delta}. \end{aligned} \tag{5.17}$$

From here on, we work in Kerr coordinates and for the ease of notation we remove the subscript 'K' from the azimuthal Kerr coordinate. The background (in Kerr coordinates) is given by

$$\begin{aligned} ds^2 = &-\left(1 - \frac{2Mr}{\Sigma}\right) dv^2 + \left(r^2 + a^2 + \frac{2Mra^2\sin^2\theta}{\Sigma}\right)\sin^2\theta\, d\phi^2 \\ &+\frac{4Mar\sin^2\theta}{\Sigma}\, dvd\phi - \Sigma\, d\theta^2 + dvdr - 2a\sin^2\theta\, drd\phi, \end{aligned} \tag{5.18}$$

where we recall M is the mass of the background black hole, a is its spin parameter, and $\Sigma = r^2 + a^2\cos^2\theta$. On transformation to Kerr coordinates, we get a simple form for the differential operator

$$D^\dagger = \partial_r. \tag{5.19}$$

After various simplifications and applying all derivatives to obtain Ψ is given by

$$\Psi = -\frac{1}{24}\Delta^2 \sum_m {}_2\bar{Y}_2^m(\theta, \phi)\bar{z}_m(v). \tag{5.20}$$

In above equation, the spin-weighted spherical harmonics ${}_2Y_2^m(\theta, \phi)$ and Δ^2 carry the angular and the radial dependence, respectively, while the information of tidal environment is encoded in $\bar{z}_m(v)$.

The tidally perturbed metric

The metric of the tidally perturbed space-time can be written as follows:

$$g_{ab} = g^B_{ab} + h_{ab}, \tag{5.21}$$

where g^B_{ab} and h_{ab} is the background Kerr metric and the tidal perturbation, respectively. Wald, Cohen, and Kegeles [88, 89] showed that metric perturbation can be constructed as [85],

$$h_{ab} = \Pi_{ab}[\Psi]. \tag{5.22}$$

Here, Π_{ab} is a differential operator that depends on the tetrad and directional derivatives constructed from the tetrad ($D = l^a\partial_a$, $\delta = m^a\partial_a$). Using the spin-coefficients (defined below) we can compactly write the metric perturbation as [90],

$$\begin{aligned} h_{ab} &= 2\Re\Big(\Big\{-l_a l_b(\delta+\bar{\alpha}+3\beta-\tau)(\delta+4\beta+3\tau) - m_a m_b(D-\rho)(D+3\rho) + l_{(a}m_{b)} \\ &\quad \times[(D-\rho+\bar{\rho})(\delta+4\beta+3\tau) + (\delta+3\beta-\bar{\alpha}-\bar{\pi}-\tau)(D+3\rho)]\Big\}\Psi\Big)\,. \end{aligned} \tag{5.23}$$

Here the bar over quantities denote the complex conjugate. The metric perturbation (see Eq.(5.23)) depends on the spin coefficients $(\rho, \beta, \pi, \tau, \alpha)$ of the background. The explicit expressions are as follows [83],

$$\begin{aligned} \rho &= -\frac{r}{\Sigma} - i\frac{a}{\Sigma}\cos\theta, \\ \beta &= \frac{\sqrt{2}}{4}\frac{r}{\Sigma}\cot\theta - i\frac{\sqrt{2}}{4}\frac{a}{\Sigma}\cot\theta\cos\theta, \\ \pi &= -\sqrt{2}\frac{a^2}{\Sigma^2}r\sin\theta\cos\theta + i\frac{\sqrt{2}}{2}\frac{a}{\Sigma^2}\left(r^2 - a^2\cos^2\theta\right)\sin\theta, \\ \tau &= -i\frac{\sqrt{2}}{2}\frac{a}{\Sigma}\sin\theta, \\ \alpha_R &= -\sqrt{2}\frac{a^2}{\Sigma^2}r\sin\theta\cos\theta - \frac{\sqrt{2}}{4}\frac{r}{\Sigma}\cot\theta, \\ \alpha_I &= \frac{\sqrt{2}}{2}\frac{a}{\Sigma^2}\sin\theta\left(r^2 - a^2\cos^2\theta\right) - \frac{\sqrt{2}}{4}\frac{a}{\Sigma}\cot\theta\cos\theta, \end{aligned} \tag{5.24}$$

where to improve readability α_R and α_I are the real and imaginary part of the spin coefficient α. The differential operators (in Kerr coordinates) are expressed as,

$$\begin{aligned} D &= \partial_r + \frac{2a}{\Delta}\partial_\phi, \\ \delta &= \frac{1}{\sqrt{2}(r+ia\cos\theta)}\left(\partial_\theta + \frac{i}{\sin\theta}\partial_\phi\right). \end{aligned} \tag{5.25}$$

The reconstructed metric is given in the ingoing radiation gauge, which satisfies

$$h_{ll} = h_{ln} = h_{lm} = h_{l\bar{m}} = h_{m\bar{m}} = 0.$$

As a final step, we need to take the necessary derivatives on the spin coefficients as well as the potential to determine the form of metric perturbation. The full expression is presented in Eq.(58) of Ref. [83].

Chapter 6

Tidal resonances in EMRIs

6.1 Executive summary

Extreme mass ratio inspirals (EMRIs) will be important sources for future space-based gravitational-wave detectors. In 2019, B. Bonga, H. Yang , and S. Hughes pointed out the relevance of a new phenomena — named, tidal resonances in EMRIs due to a nearby tertiary. These resonances contain information about the next closest BH(s) or stars to EMRI systems and may hold important clues about the formation of galaxies. The tidal resonances in binary orbital evolution induced by the tidal field of nearby stars or black holes have been identified as being potentially significant in the context of EMRIs. These resonances occur when the three orbital frequencies describing the orbit are commensurate. During the resonance, the orbital parameters of the small body experience a 'jump' leading to a shift in the phase of the gravitational waveform. In this chapter, we treat the tidal perturber as stationary, and present a first study of how common and important such resonances are over the entire orbital parameter space. We find that a large proportion of inspirals encounter a low-order resonance in the observationally important regime. While the 'instantaneous' effect of a tidal resonance is small, its effect on the accumulated phase of the gravitational waveform of an EMRI system can be significant due to its many cycles in band; we estimate that the effect is detectable for a significant fraction of sources. We also provide fitting formulae for the induced change in the constants of motion of the orbit due to the tidal resonance for several low-order resonances.

6.2 Motivation

It is unlikely that all EMRIs can be treated as completely isolated for the duration in the LISA band. If an EMRI system is not isolated but is instead influenced by another astrophysical object, the tidal perturbation (even though relatively small to the background) can modify the orbital dynamics and GW radiation of the EMRI system resulting in phase variations in the gravitational waveform [6, 91]. For an EMRI formed in a wet environment, the active accretion disk itself can be treated as a tidal perturber. Also, in this scenario, dynamical friction caused by the disk interaction may leave imprints on GWs [41, 92]. Recently, there has also been work focusing on the "dephasing" of EMRI signal due to the dynamical friction caused by dark matter halos around SMBH [93–95]. All these environmental effects are likely to be detectable with future GW observatories.

We focus on one such environmental scenario — tidal resonances caused by the tidal field generated by close stars/BHs near the EMRI system [6]. During most of the EMRI inspiral, the tidal field of nearby objects can be neglected. However, when the three fundamental orbital frequencies describing the orbit become commensurate, a tidal resonance occurs[1]. As a result, the gravitational potential of the tidal perturber measurably changes the orbit of the small BH and thereby the gravitational radiation it emits. GWs undergoing such resonances will therefore encode information — although limited — about the environment of the galactic center, which is difficult to obtain from EM observations.

Here, we develop analytic and numerical tools to study tidal resonances with the aim of surveying the orbital parameter space and investigating how often tidal resonances occur in realistic inspirals. We compute the accumulation in phase after a tidal resonance has been encountered by an EMRI to understand their impact on waveforms. We investigate properties of tidal resonances such as the effect of spin of the central massive black hole, and the orbital parameters of the EMRI on the strength of each resonance and the resulting phase shift.

6.2.1 Event rate for tidal resonances

Studies based on a Fokker-Planck simulation suggest that a population of $40M_\odot$ BHs can be close to Sagittarius A*, with a median distance $\sim 5\,\mathrm{AU}$ [97, 38, 6]. According

[1]Tidal resonances occur under more general conditions than self-force resonances, which require $n\omega_r + k\omega_\theta = 0$. A tidal resonance occurs when the three orbital frequencies of the EMRI *and* the three of the perturber are commensurate [96]. However, we treat the perturber as static, hence its corresponding orbital frequencies do not play a role in resonance condition.

to [24, 98], brown dwarfs can be at an approximate distance of $\sim 30\,\mathrm{AU}$ for Sgr A*. If this holds for even 10% of EMRI events, the detection rate for the observation of tidal resonances can be approximated to be a few yr^{-1} [6]. The EMRI merger rate is itself uncertain depending on the model parameters as discussed in Sec 3.1. Following [6, 44], we adopt the EMRI merger rate as

$$\frac{1}{T_{\mathrm{EMRI}}} \approx 0.3 \left(\frac{M}{10^6 M_\odot}\right)^{0.19} \mathrm{Myr}^{-1}\,, \tag{6.1}$$

where T_{EMRI} is the interval between EMRI events, and M is the mass of the central SMBH. Under the assumption of circular orbits and considering that the shrinking of the orbit is mainly driven by GW emission, we can write a relation between the time to coalescence and the distance R to the next infalling BH (with mass $M_\star$) as [21]

$$T_{\mathrm{EMRI}} \sim \frac{R}{\dot{R}} \sim \frac{5}{256}\frac{c^5 R^4}{G^3 M_\star M^2}\,, \tag{6.2}$$

Combining the two equations, we can have a rough estimate of the distance of the nearest neighbors to SMBH:

$$R \sim 5.6\ \mathrm{AU} \left(\frac{M_\star}{30 M_\odot}\right)^{1/4} \left(\frac{M}{4\times 10^6 M_\odot}\right)^{0.45}\,. \tag{6.3}$$

Since the tidal field scales as $M_\star/R^3$, the closest stellar-mass BHs are likely to be the main contributors to the tidal environment of EMRIs.

6.3 Framework of tidal resonances

GWs from EMRIs will encode the information of curvature around the central black hole. In addition to this invaluable data, they can also be used to probe the stellar distribution in galactic centers. In our study, we consider an EMRI within the influence of an external tidal field. The information about the tidal environment created by a stellar-mass object near EMRI is treated in a fully relativistic framework by computing the perturbation to the Kerr spacetime (as demonstrated in Chapter 5). We use a set of action-angle variables to study the orbital evolution, such that the action variables J_i parameterize a torus (constant surface of conserved quantities $\{E, L_z, Q\}$) and the conjugate angle variables q_i span the torus with angular advances . This method offers a simple formulation to incorporate and study deviations from the geodesic motion

due to different forces [56]:

$$\frac{dq_i}{d\tau} = \omega_i(\mathbf{J}) + \epsilon g^{(1)}_{i,\mathrm{td}}(q_\phi, q_\theta, q_r, \mathbf{J}) + \eta g^{(1)}_{i,\mathrm{sf}}(q_\theta, q_r, \mathbf{J}) + O(\eta^2, \epsilon^2, \eta\epsilon)\,, \tag{6.4}$$

$$\frac{dJ_i}{d\tau} = \epsilon G^{(1)}_{i,\mathrm{td}}(q_\phi, q_\theta, q_r, \mathbf{J}) + \eta G^{(1)}_{i,\mathrm{sf}}(q_\theta, q_r, \mathbf{J}) + O(\eta^2, \epsilon^2, \eta\epsilon)\,, \tag{6.5}$$

where the terms with subscript "td" are from the tidal force, and the terms with subscript "sf" are from the self-force. Here, the parameter

$$\epsilon = M_\star M^2\, \mathrm{x}_\star / R^3 \tag{6.6}$$

characterizes the strength of the tidal field produced by the perturber $M_\star$ at an inclination $I_\star$. Here, $\mathrm{x}_\star$ is a sinusoidal function of $I_\star$ depending on mode m of the quadrupole ($l = 2$) tidal perturbation. The distance of the tidal perturber from the central MBH is denoted by R. As mentioned before, the frequencies of EMRI orbital evolution associated with a distant observer time are ω_r (oscillations in the radial direction), ω_θ (oscillations in the polar direction), and ω_ϕ (rotations around the central BH spin axis).

From the expressions above, we see that at the zeroth order (neglecting the terms with the superscript (1) and higher order), the action variables are conserved whereas the angle variables increase at a fixed rate in time, which are denoted by ω_i. At leading order in η, the EMRI orbit deviates from the geodesic motion due to the particle's self-force ($g_{i,\mathrm{sf}}$,$G_{i,\mathrm{sf}}$) [52–55]. In our model, the EMRI experiences an external tidal force introduced in evolution equations by terms ($g_{i,\mathrm{td}}, G_{i,\mathrm{td}}$). The tidal force depends on the axial position of the small body ϕ unlike the self-force (due to axisymmetry of the Kerr spacetime). The tidal force acts as a purely conservative force in contrast to the self-force which is both conservative and dissipative. Given the conservative nature of the tidal force, at leading order, the tidal force can be neglected throughout most of the inspiral except when a resonance is encountered (this is also demonstrated in Fig. 6.12.) The mathematical description of the tidal resonance is similar to the resonance effect induced by the self-force itself [73]. Both resonances are transient because the orbital frequencies are changing due to radiation reaction. The main difference between the two resonances is the force that causes it (the tidal force versus the self-force).

As we proceed, we will only consider tidal resonances and hence the leading order tidal force $G^{(1)}_{i,\mathrm{td}}$, and we will drop the subscript 'td', for brevity. The force is written

in terms of its Fourier modes as

$$G_i^{(1)}(q_\phi, q_\theta, q_r, \mathbf{J}) = \sum_{n,k,m} G^{(1)}_{i,nkm}(\mathbf{J}) e^{i(nq_r + kq_\theta + mq_\phi)} \,. \tag{6.7}$$

For non-resonant orbits, the exponential factor in the above equation is rapidly oscillating in time, thereby averaging to zero over many cycles. Thus, all m, k, n modes, except for the one with $m = k = n = 0$, do not contribute to a secular change in $\mathbf{J}$. However, the phase in Eq. (6.7) will be stationary when

$$\omega_{nkm} := n\omega_r + k\omega_\theta + m\omega_\phi = 0 \,, \tag{6.8}$$

i.e. when the tidal resonance condition is satisfied for a set of relatively small integers[2] (n, k, m). Thus, the exponential factor varies slowly around the resonance point, and the corresponding average of the force amplitude $G^{(1)}_{i,nkm}$ is non-vanishing, inducing a secular change in $\mathbf{J}$. During resonance, the orbital motion is restricted to a subspace of the full orbital three-torus $\mathbb{T}^3 = \{q_r, q_\theta, q_\phi\}$.

It is helpful to recall the relevant timescales for our physical setup. The fastest timescale is the orbital period $\tau_{\rm orb} \sim \mathcal{O}(M)$ and the slowest timescale corresponds to the radiation reaction time $\tau_{\rm rr} \sim M/\eta$. The orbital period of the tidal perturber is given by $\tau_{\rm td} \sim 2\pi\sqrt{R^3/M}$. Another key time scale is the resonance duration $\tau_{\rm res}$ [73, 100],

$$\tau_{\rm res} \sim \sqrt{\frac{4\pi}{m\dot{\omega}_\phi + k\dot{\omega}_\theta + n\dot{\omega}_r}} \sim M\sqrt{\frac{1}{\eta}} \,. \tag{6.9}$$

Overall, when the stationary perturber approximation is valid, we have

$$\tau_{\rm orb} \ll \tau_{\rm res} \ll \tau_{\rm td}, \tau_{\rm rr}.$$

However, if the third body is close to the EMRI on the equatorial plane, thereby violating the static approximation, the resonance condition is altered in the following way (assuming equatorial circular prograde or retrograde orbit of the perturber)

$$m(\omega_\phi \pm \Omega_{\phi,\rm td}) + k\omega_\theta + n\omega_r = 0 \,. \tag{6.10}$$

[2]When the condition is satisfied for large integers,the corresponding $G^{(1)}_{i,nkm}$ is much smaller. Hence, they tend to be irrelevant from the observational point of view, although it also depends on the magnitude of the tidal perturbation which resonances are sufficiently influential. This holds true for self-forces resonances as well [99].

In other words, the leading effect of the motion of the perturber would be the change in time of occurrence of resonance. Of course, the tidal force itself will also be different: instead of being time-independent, it will need to include the dynamical effects of the motion of the tidal perturber. However, the time-dependence of the tidal perturber is expected to be subdominant to the leading order quadrupolar field and therefore not considered in our work. Since for all resonances we consider $\Omega_{\phi,td} \ll \omega_\phi$, this shift is negligible in evaluating the resonance strength. Note that the condition above is very similar to the resonance condition of mean motion resonances discussed in [96]. In fact, the tidal resonances considered here are a subset of the relativistic mean motion resonances: tidal resonances are mean motion resonances for which the motion of the outer object can be considered static.

As discussed in Chapter 4, Flanagan and Hinderer [73] gave an analytic expression for the 'jump' induced in the constants of motion due to self-force resonances. We use a similar estimate to model the effect of the tidal resonance, and calculate the jump ΔJ_i in conserved quantities across a resonance point. Assuming that the evolution of $\mathbf{J}$ and hence the orbital periods is dominantly determined by the gravitational radiation reaction, the jump ΔJ_i is estimated as

$$\Delta J_i = \epsilon \int_{-\infty}^{\infty} G_i^{(1)}(q_\phi, q_\theta, q_r, \mathbf{J}) d\tau = \epsilon \sum_{s=\pm 1} \sqrt{\frac{2\pi}{|\Gamma s|}} \exp\left[\mathrm{sgn}(\Gamma s)\frac{i\pi}{4} + is\chi\right] \times G^{(1)}_{i,sn,sk,sm}(\mathbf{J})\,, \quad (6.11)$$

where $\chi = nq_{r0} + kq_{\theta 0} + mq_{\phi 0}$ and $\Gamma = n\dot{\omega}_{r0} + k\dot{\omega}_{\theta 0} + m\dot{\omega}_{\phi 0}$, and the quantities q_{i0} and $\dot{\omega}_{i0}$ are phases and frequency derivatives evaluated at $\tau_{\mathrm{res},0}$ (the instant where tidal resonance condition is satisfied), respectively. Strictly speaking, higher modes with (n, k, m) multiplied by an integer other than ± 1 are also non-vanishing, but their contribution is highly suppressed. This is expected because higher-order resonances $(n, k > 4)$ come closer to covering all the points in the phase-space, so they are more like averaging over the whole space. In the estimate of Γ, the corrections due to the tidal resonance are neglected, because such corrections are higher order in ϵ. The change across resonance is proportional to $\eta/\epsilon^{1/2}$. In this work, we study only the leading quadrupolar l=2 modes, because the higher multipoles will be smaller by a power of M/R. For l =2, allowed values for azimuthal number m are -2 to 2. In Fig 6.1, we show the full set of low order resonance combinations investigated in our analysis. We find that resonance jumps vanish for combinations with $k + m =$ odd. This suppression is discussed in Appendix A.2.

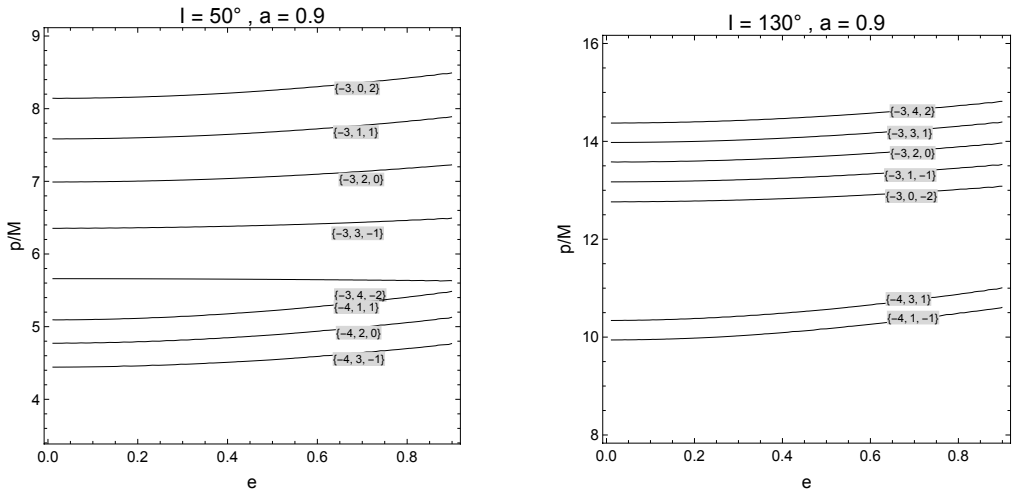

Fig. 6.1 The low order tidal resonance contours for a prograde orbit with inclination 50° (left) and a retrograde orbit with inclination 130° (right) in e - p plane. The spin parameter of the central BH is set to $a = 0.9$. The contour labels correspond to integers $\{n, k, m\}$. We discuss the suppression of resonance combinations with $k + m =$ odd in appendix A.1.

To calculate the tidal force $G_i^{(1)}$, we incorporate the influence of the third object, the tidal perturber, on the EMRI system by calculating its induced tidal deformation of the central BH spacetime. The induced deformation causes the small object of the EMRI to coherently accelerate when resonance occurs. Thus, as a first step, we need the perturbation $h_{\alpha\beta}$ to the central BH's spacetime due to the tidal field. This is obtained by solving the Teukolsky equation [86] in the slow-motion limit (the radius of curvature $\mathcal{R}$ associated to the external spacetime is taken to be much larger than the BH's scales, *i.e.*, $M/\mathcal{R} \ll 1$) followed by metric reconstruction so that the resulting metric is in the ingoing radiation gauge [83]. Another metric describing a tidally deformed black hole given by Eric Poisson also exists [85], which is in the lightcone gauge with coordinates adapted to this gauge and does not rely on metric reconstruction. However, this metric is only valid in the slow spin limit and we would like to explore the entire range in spin of the central black hole. Therefore, we use the metric [3] discussed in Chapter 5.

The metric given by [83] includes only quadrupolar l=2 modes because the higher multipoles will be smaller by a relative factor of $\mathcal{O}(M/\mathcal{R})$. For l =2, allowed values for azimuthal number m are $-l$ to l. However, the m=0 mode is excluded from the

[3]Note that there is an overall factor of two missing in $h_{\alpha\beta}$ in [83]; see footnote 17 in [101] for details. After correcting for this factor, dL_z/dt agrees in the slow spin limit with dL_z/dt for $h_{\alpha\beta}$ given in [85].

metric[4]. An additional point of observation is that if the position of the tidal perturber is restriced to the equatorial plane, the Newmann-Penrose scalar ψ_0 (see (5.12)) is zero for $m = \pm 1$ modes. Nevertheless, we include all $m = \pm 2, \pm 1, 0$ modes in our inclined perturber setting. The input for the metric reconstruction procedure is z_m. At leading order, these coefficients are determined by the electric and magnetic quadrupole moment tensor denoted by $\mathcal{E}_{ab}$, and $\mathcal{B}_{ab}$, respectively. Quadrupole moment tensors scale as [102]

$$\mathcal{E}_{ab} \sim \frac{1}{\mathcal{R}^2}\,, \quad \mathcal{B}_{ab} \sim \frac{\mathcal{V}}{\mathcal{R}^2}\,,$$

where $\mathcal{V} \sim \sqrt{\dfrac{M + M_\star}{R}}$ is the orbital velocity of the third body. In this work, we set the magnetic-type tensor to be zero as we assumed the tidal perturber to be stationary. In a general setting, the dynamics of the third body should be taken into account. To summarize our assumptions, we consider a stationary tidal perturber restricted to the equatorial plane and take into account only its $l = 2$ contributions in the tidal resonance.

The tidal perturber is aligned along the x-axis and for the electric tidal moment tensor we take the following form:

$$\mathcal{E}_{ab} = \frac{M_\star}{R^3}(2\nabla_a x \nabla_b x - \nabla_a y \nabla_b y - \nabla_a z \nabla_b z)\,, \tag{6.12}$$

where x, y, and z are the Cartesian-like coordinates (see Sec. IXB of [103]). We substitute this as input to obtain $h_{\alpha\beta}$ in the ingoing radiation gauge in advanced Eddington-Finkelstein coordinates (called Kerr coordinates in [83]).

Next, we perform a coordinate transformation from the advanced Edington-Finkelstein coordinates $\{v, r_{\rm EF}, \theta_{\rm EF}, \phi_{\rm EF}\}$ to Boyer-Lindquist coordinates $\{t, r, \theta, \phi\}$:

$$dv = dt + \left(1 + \frac{2Mr}{r^2 - 2Mr + a^2}\right) dr\,, \tag{6.13a}$$

$$dr_{\rm EF} = dr\,, \tag{6.13b}$$

$$d\theta_{\rm EF} = d\theta\,, \tag{6.13c}$$

$$d\phi_{\rm EF} = d\phi + \frac{a}{r^2 - 2Mr + a^2} dr\,. \tag{6.13d}$$

Given $h_{\alpha\beta}$, the induced acceleration with respect to the background Kerr spacetime is

$$a^\alpha = -\frac{1}{2}(g^{\alpha\beta}_{\rm Kerr} + u^\alpha u^\beta)(2h_{\beta\lambda;\rho} - h_{\lambda\rho;\beta})u^\lambda u^\rho\,, \tag{6.14}$$

[4]These modes are included in the slow-spin limit metric given by Poisson [85].

with u^α the unit vector tangent to the worldline of the EMRI's small mass μ. The instantaneous change rate of the constants of motion are [91]

$$\frac{dL_z}{d\tau} = a_\phi \,, \tag{6.15}$$

$$\frac{dQ}{d\tau} = 2u_\theta a_\theta - 2a^2\cos^2\theta u_t a_t + 2\cot^2\theta u_\phi a_\phi \,. \tag{6.16}$$

The energy E is conserved as the spacetime is stationary. With these equations in hand, we obtain $dL_z/d\tau$ and $dQ/d\tau$ due to the stationary phase harmonics of the tidal force, $G_{i,mkn}$, as a function of χ (see Eq. (6.11)). Another quantity needed for the computation of jump is Γ which contains information about the resonance duration is obtained from the rate of change of the orbital frequencies at the time of resonance.

6.3.1 Method of determining inspiral

For the evolution of an EMRI orbit, we use the numerical data (shared with us by R. Fujita [61]) for the GW fluxes dissipated by a stellar-mass object with bound orbits around a Kerr BH of spin parameter a for large sets of orbital parameters. The derivation of GW fluxes in the data sets used methods presented in Refs. [104–106] based on the formalism developed by Mano, Suzuki, and Takasugi (MST) [107–110].

Using the MST code, the adiabatic change of constants of motion was computed for a number of data points in the semi-latus rectum p, the orbital eccentricity e, and the orbital inclination I for different spin parameters. We obtained dC^i/dt in phase space $\{p, e, I\}$ through polynomial fitting where $C^i = \{E, L_z, Q\}$. Further, the secular evolution of orbital parameters $P^i = \{p, e, I\}$ is derived from those of $C^i = \{E, L_z, Q\}$ using

$$\left\langle \frac{dP^i}{dt} \right\rangle = \sum_j (\mathcal{T}^{-1})^i_{\ j} \left\langle \frac{dC^j}{dt} \right\rangle, \tag{6.17}$$

where $\mathcal{T}_i^{\ j} \equiv \partial C^j/\partial P^j$ is the Jacobian matrix for the transformation from $\{E, L_z, Q\}$ to $\{p, e, I\}$. Using this approach, we obtain accurate orbits at inexpensive computational cost. One caveat is that the numerical data sets of GW fluxes are obtained only for orbital eccentricity e upto 0.7 and each data set is truncated at $p \sim 6M$ for each value of the spin.[5] Therefore, accuracy of our numerical fitting for fluxes below $6M$ is limited by the available data sets and we rely on extrapolation for the change in fluxes in this region.

[5]When numerical fluxes become available across the parameter space at inexpensive computational costs, we plan to extend our fittings in future work.

Returning to Eq. (6.11), we obtain the change in frequencies during an inspiral from these numerical fits and evaluate Γ. For the implementation of the analytic expressions of fundamental frequencies [51, 49], our code employs the 'Kerr Geodesic' Package from the Black Hole Perturbation Toolkit [111].

6.4 Results

In this section, we investigate the orbital parameter space and find some trends regarding the number of resonances encountered and the strength of each resonance as a function of the spin of the central massive black hole and the orbital parameters of the EMRI. We compute the accumulated phase shift due to different tidal resonances and show the affected parameter space. In addition to calculating the jump semi-analytically, we have also implemented the tidal effects using the forced osculating orbital elements method [112, 113]. The numerical evolution establishes that, as expected, the tidal force can be neglected throughout most of the EMRI evolution except during resonances. Moreover, the numerical evolution not only agrees qualitatively with the general features of tidal resonances, but also quantitatively. In particular, the numerically evaluated jumps agree remarkably well with the semi-analytic methods, thereby supporting the validity of both methods, which are implemented independently.

6.4.1 Inspiral crossing tidal resonances

Our aim is to span the complete orbital parameter space that is likely relevant for observationally important EMRI events. With the help of numerical data, we can compute the inspiral for both prograde ($0 \leq I < \pi/2$) and retrograde orbits ($\pi/2 < I < \pi$) by picking initial I from the set $\in [20°, 50°, 80°, 100°, 130°, 160°]$. The spin parameter are chosen from the set $a/M \in [0.1, 0.5, 0.9]$ ranging from a slowly rotating central BH to a rapidly rotating one. For the orbital eccentricity e, the range varies from $0.0125 \leq e \leq 0.7$ with grid spacing $\Delta e = 0.0125$. The values of p are not randomly sampled but are chosen such that the resonance condition in Eq. (6.8) is satisfied for some low order integers n, k, and m.

We find that every inspiral encounters at least one lower-order resonance. As also seen for self-force resonances, higher-order resonances have smaller jumps compared to lower-order ones [79]. In Fig. 6.2, we show the low-order tidal resonances (*i.e.* $n, k \in [-4, 4]; m = 0, \pm 2$) shown by black contours in the e - p plane for different spin parameters of the central black hole. In the upper panel, prograde geodesics

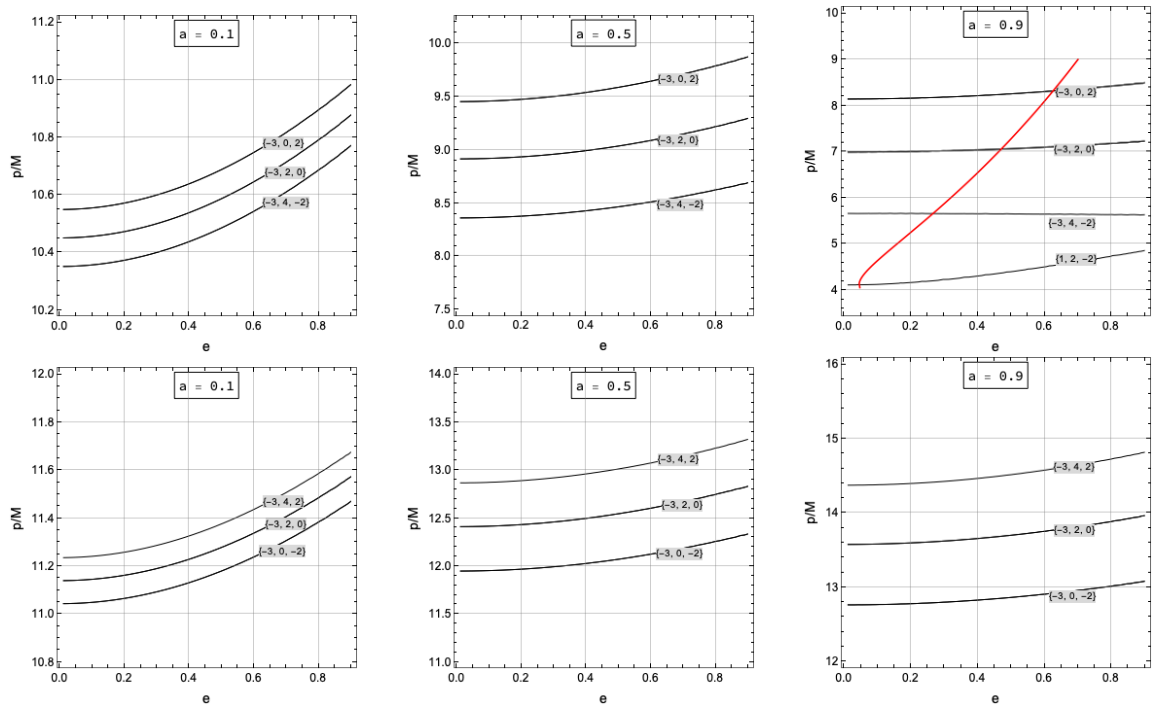

Fig. 6.2 The upper panels shows the tidal resonance contours for prograde orbits with orbital inclination 50° for different spin parameters of the central BH in e - p plane. The contour labels correspond to integers n, k, m. In the right figure (upper panel), an inspiral is shown in red starting at $e = 0.7$ and $p = 9M$. During the evolution, p shrinks and e decreases due to radiation reaction. We see that before plunging, the orbit crosses multiple tidal resonances. The lower panels show the tidal resonance contours for retrograde orbits with orbital inclination 130° for different spin parameters.

are considered with $I = 50°$ whereas in the lower panel, resonances are shown for retrograde geodesics with $I = 130°$. We see that the value of p at which resonances occur depends strongly on EMRIs orbital parameters. For instance, comparing the plots in the upper panel, the same resonance contour is in a different location on the e - p plane as the spin parameter varies (left to right).

As an example, we show an inspiral (in red) evolving in the e - p plane with $a = 0.9$ and $I = 50°$. As the orbit shrinks and circularizes due to radiation reaction it passes through four low-order tidal resonances before it plunges. When a resonance occurs at large p, the tidal field is stronger, leading to a larger jump in conserved quantities. Note that for retrograde orbits (lower panel) resonances occur at larger values of p as compared to prograde orbits thereby experiencing a larger tidal force. Also, at large p, the EMRI systems evolve relatively slowly, spending more time in resonance. To access the secular impact of tidal resonances on EMRIs the time remaining after crossing each resonance is also of importance. The space-based low-frequency interferometers will be able to track the evolution of EMRI waves for years. In the example shown, for an inspiral with parameters $M = 4 \times 10^6 M_\odot$ and $\mu = 30 M_\odot$ the observational time after crossing the $n : k : m = -3 : 0 : 2$ resonance is about 10 yrs whereas the $-3 : 4 : -2$ resonance is crossed ~ 1.5 yrs before plunge.

6.4.2 Dependence on orbital phase

When we introduce the tidal perturber on the equatorial plane, the spacetime describing the central black hole and the tidal perturber is no longer axisymmetric. As shown in Eq. (6.5), the tidal force depends on the axial position of the small body. Hence, the change in conserved quantities is sensitive to EMRI's orbital phase on entering the resonance. To illustrate this dependence, we first compute dL_z/dt and dQ/dt for some resonance with non-zero m, k, n. After orbit averaging, the sum in Eq. (6.7) can be written as,

$$\left\langle G_i^{(1)}(q_\phi, q_\theta, q_r, \mathbf{J}) \right\rangle \approx G_{i,mkn}^{(1)}(\mathbf{J}) e^{i(m q_{\phi 0} + k q_{\theta 0} + n q_{r0})} + \{\text{c.c.}\}. \tag{6.18}$$

In Fig. 6.3, we show dependence of average change rate of conserved quantities on $q_{\phi 0}$ for an inspiral orbit (shown in Fig. 6.2) crossing the $3 : 0 : -2$ resonance with $a = 0.9$. Note that $\langle dL_z/dt \rangle$ and $\langle dQ/dt \rangle$ are made non-dimensional by factoring out ϵ/M.

The phases q_{r0} and $q_{\theta 0}$ determine the values of r and θ at resonance. Here, we set $q_{\theta 0} = 0$ and $q_{r0} = 0$ when the orbit enters resonance meaning that the orbit enters resonance at $\theta = I$ and $r = r_{\rm min}$. The azimuthal phase $q_{\phi 0}$ describes the

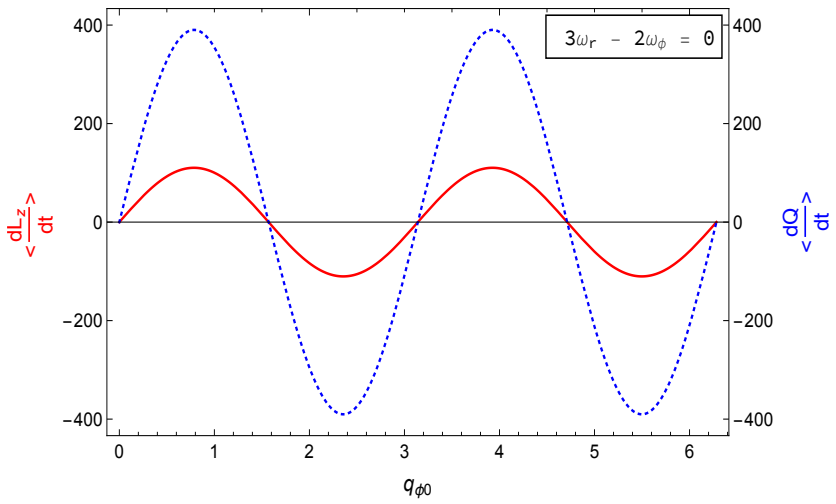

Fig. 6.3 Average change rate of z-component of angular momentum (red-solid) and Carter constant (blue-dotted) as a function of orbital phase $q_{\phi 0}$ for an orbit crossing the $n:k:m=3:0:-2$ resonance with $a=0.9$. Both $\langle dL_z/dt\rangle$ and $\langle dQ/dt\rangle$ are normalised by ϵ and powers of M to be dimensionless.

motion of a small object with mass μ around the central BH spin axis. The change induced in constants of motion has sinusoidal dependence on phase, *i.e.*, $\sin(m\,q_{\phi 0})$. Therefore, depending on this phase an orbit may cross the tidal resonance without "feeling" its effect. In our analysis, to determine the impact of tidal resonances, we will fine-tune the phase value such that the change in L_z and Q due to resonance is maximum. In that sense, our results show the upper limit of influence caused by these resonances. The phase dependence is easily retrieved by multiplying the results here by $\sin(mq_{\phi 0}+kq_{\theta 0}+nq_{r0})$.

6.4.3 Trends and fitting formulae

In addition to the information of orbital phase, to estimate the jump in the constants of motion induced (see Eq. 6.11) by tidal resonances, we need the rate of change in orbital frequencies (Γ) and tidal force amplitude $G_{i,mkn}$. First, we survey the orbital parameter space and compute dL_z/dt and dQ/dt for different resonances to find some interesting trends. Using the numerical data obtained by evaluating the analytic expressions given in Eqs. (6.15) and (6.16) we made 3-D $\{a,e,x\}$ fitting formulas by making a polynomial ansatz of the form $C_{ijk}a^ie^jx^k$ up to some order in i,j,k and then fitting the numerical data points simultaneously to obtain the coefficients C_{ijk}. These numerical

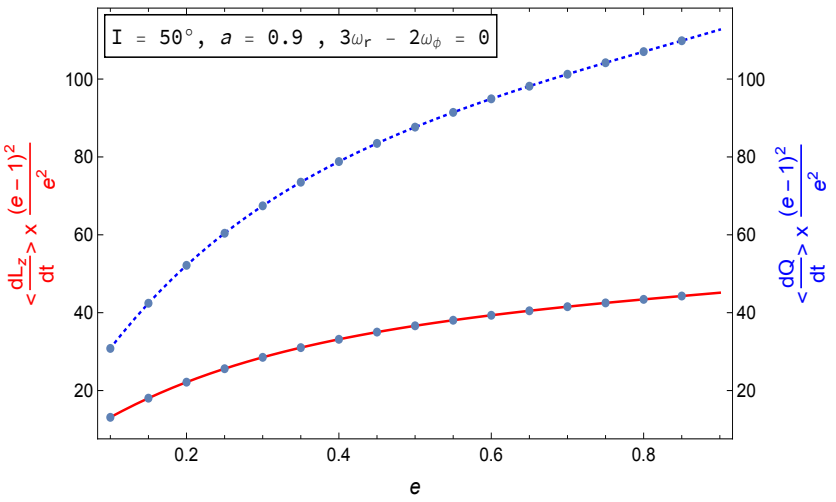

Fig. 6.4 Dependence of average change rate of the z-component of angular momentum (red-solid) and Carter constant (blue-dotted) on the orbital eccentricity for $n:k:m=3:0:-2$ with spin parameter and orbital inclination set to 0.9 and 50°, respectively. Both rates of change increase with increasing eccentricity. The factor $e^2/(e-1)^2$ ensures that dL_z/dt and dQ/dt are zero for circular orbits ($e=0$) since ω_r is zero in that case. The dots represent the values obtained from semi-analytic calculation and curves denote the obtained fitting.

fits allow inexpensive calculations of dL_z/dt and dQ/dt due to a tidal resonance. First to analyse the trends of different resonance combinations, we discuss them separately depending on the value of azimuthal integer m.

Resonances with $m=\pm 2$

We find that for all the resonances encountered by an inspiral before plunge the change in L_z and Q increases as we go from low to high eccentricity regardless of the rotation direction of the orbit, *i.e.*, prograde or retrograde. This is expected because for large eccentricity, the distance of the apoapsis $r_a=a(1+e)$ is larger and hence it experiences a larger tidal force. In Fig. 6.4, we show an increase in both quantities with eccentricity for the $3:0:-2$ resonance. The dots represent the values obtained from the semi-analytic calculations and curves denote the obtained fitting. The agreement between the semi-analytic evaluation and fitting agrees remarkably well with the error always less than 1%.

Another interesting pattern is observed with a variation in the spin parameter of SMBH. As shown in Fig. 6.5, for prograde orbits, dL_z/dt and dQ/dt decrease as the

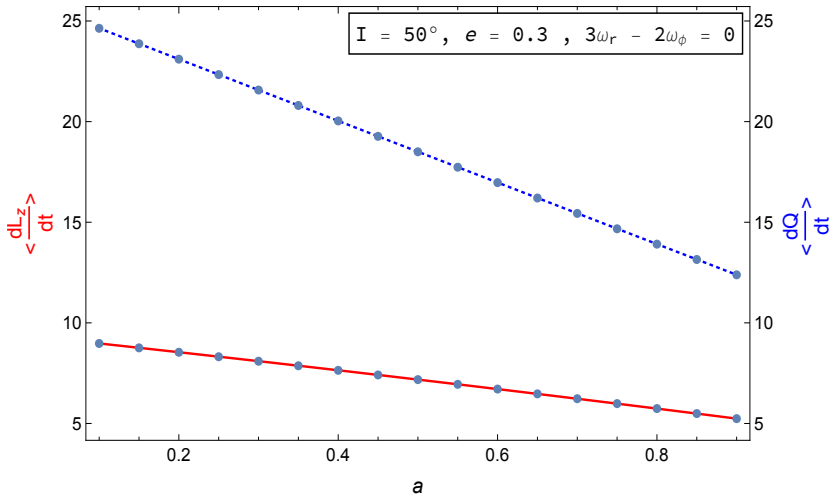

Fig. 6.5 Dependence of average change rate of the z-component of angular momentum (red-solid) and Carter constant (blue-dotted) on spin of central BH for $n : k : m = 3 : 0 : -2$ with eccentricity and orbital inclination set to 0.3 and 50°, respectively. Both quantities decrease with increasing spin of SMBH.

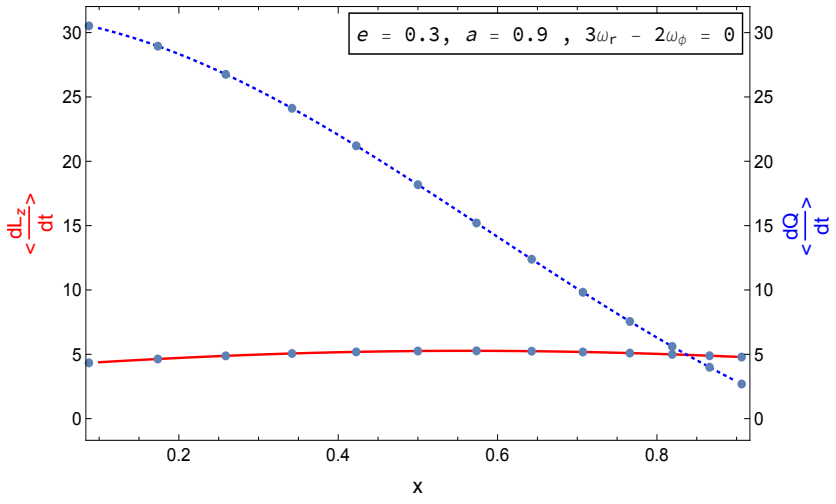

Fig. 6.6 Dependence of average change rate of the z-component of angular momentum (red-solid) and Carter constant (blue-dotted) on orbital inclination for $n : k : m = 3 : 0 : -2$ with eccentricity and spin set to 0.3 and 0.9, respectively. As we go from high to a low inclination angle, dQ/dt decreases whereas dL_z/dt appears to be largely insensitive to the orbital inclination angle. The insensitivity of dL_z/dt to inclination angle is however only true for resonances with $k = 0$.

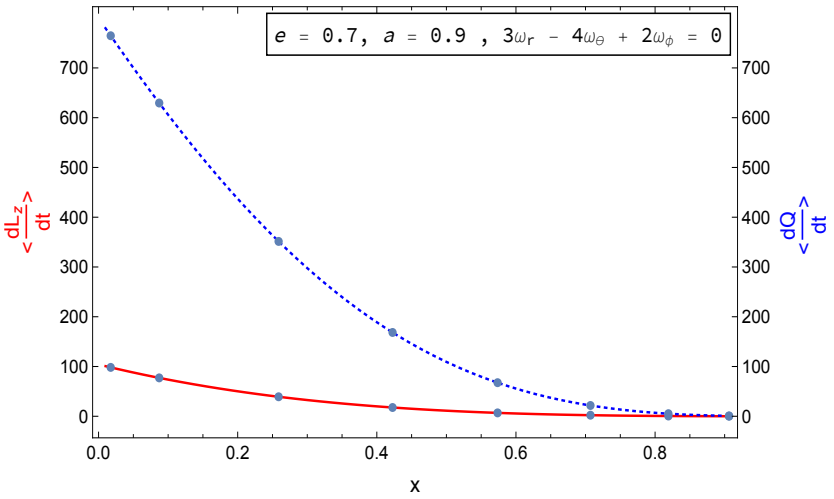

Fig. 6.7 Dependence of average change rate of the z-component of angular momentum (red-solid) and Carter constant (blue-dotted) on orbital inclination for $n : k : m = 3 : -4 : 2$ with eccentricity and spin set to 0.7 and 0.9, respectively. As we go from high to a low inclination angle, dQ/dt and dL_z/dt decreases for the prograde orbit.

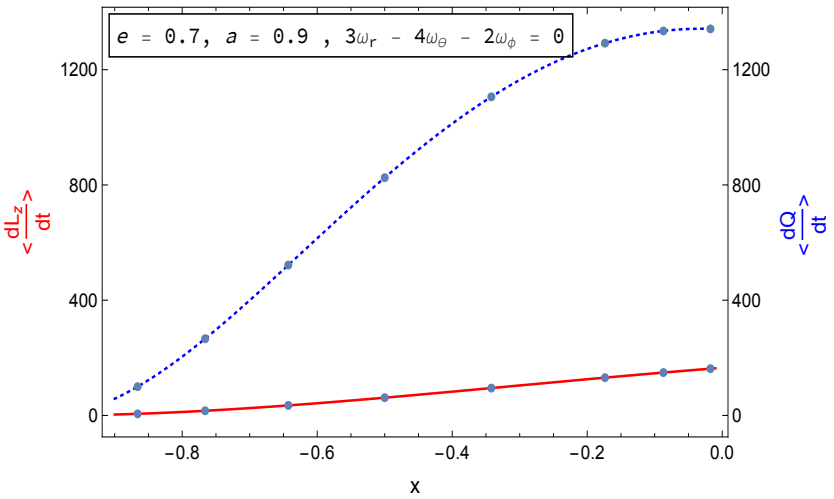

Fig. 6.8 Dependence of average change rate of the z-component of angular momentum (red-solid) and Carter constant (blue-dotted) on orbital inclination for $n : k : m = 3 : -4 : -2$ with eccentricity and spin set to 0.7 and 0.9, respectively. As we go from high to a low inclination angle, dQ/dt and dL_z/dt decreases for the retrograde orbit.

spin parameter increases. This change directly translates to the jump induced during resonance implying that for rapidly spinning central massive objects the resonance strength is smaller. However for retrograde orbits, dL_z/dt and dQ/dt increase as the spin parameter increases. This is expected because the resonance occurs at larger p values (see low panels of Fig. 6.2). Thus, the acting tidal force is greater for retrograde orbits.

We also find that as the orbital inclination angle is varied from high to low, dQ/dt and dL_z/dt decreases for both prograde and retrograde orbits. In Fig 6.6, we show both the quantities for the $3:0:-2$ resonance. The change in L_z appears to be insensitive to change in inclination, but it is only true for resonances with $k = 0$. In Fig. 6.7, dependence of dQ/dt and dL_z/dt on the orbital inclination is shown for the prograde orbit crossing $3:-4:2$ resonance. Similarly, the case for retrograde orbit crossing $3:-4:-2$ resonance is shown in Fig. 6.8.

The fitting formulae to obtain change in Q and L_z by the $3:0:-2$ (prograde orbits) resonance are given in Appendix A.1. The fitting depends on orbital parameters $\{a, e, x\}$ and sinusoidally on orbital phases $q_{\phi 0}$ and q_{r0} at resonance. The prefactor $e^2/(e-1)^2$ ensures that dL_z/dt and dQ/dt are zero for circular orbits ($e = 0$) since ω_r is zero for this case. Note that $\langle dL_z/dt\rangle$ and $\langle dQ/dt\rangle$ are normalised by multiplying a factor of $(\epsilon/M)^{-1}$. The Mathematica notebook with fitting formulae for other resonances (including $3:0:2$) is made available on [114].

Resonances with $m = \pm 1$

In the following, we first explore the strength of $m = \pm 1$ mode resonances as a function of orbital parameters (a, p, e, x) and inclination θ_{per} of the tidal perturber. We compute the change in L_z and Q for different resonances and note some interesting trends for $m = \pm 1$ modes. In Fig. 6.9, we show dependence of a sample resonance $-3:1:1$ (prograde orbit) on a, e, x and θ_{per}.

- We find that, irrespective of the resonance combinations, *i.e.* $m = \pm 1, \pm 2$, and the direction of the orbit (prograde or retrograde), both dL_z/dt and dQ/dt increase with increasing orbital eccentricity e. The prefactor $e^2/(e-1)^2$ in the fitting formulae ensures that dL_z/dt and dQ/dt are zero for circular orbits ($e = 0$) since the amplitude of radial oscillations is zero for this case.

- Another pattern is observed for variation in the spin parameter of MBH. Similar to $m = \pm 2$ modes, for prograde orbits, $m = \pm 1$ mode resonances show a decrease in both dL_z/dt and dQ/dt as a increases whereas for retrograde orbits

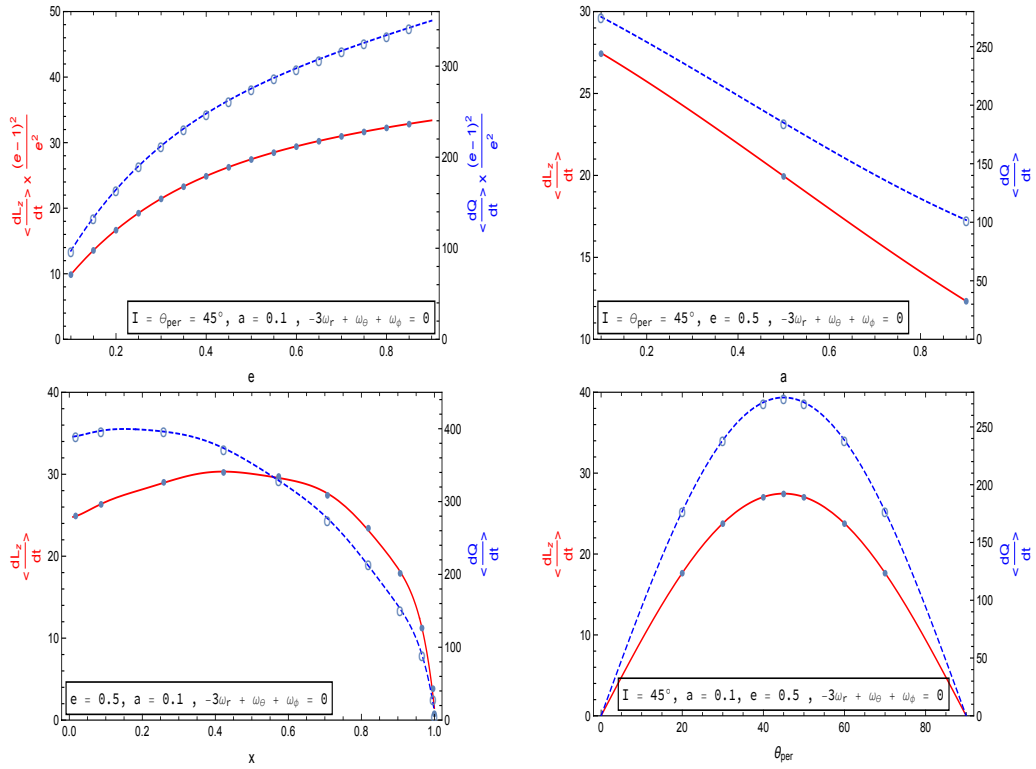

Fig. 6.9 Dependence of average change rate of the z-component of angular momentum (red-solid) and Carter constant (blue-dashed) on the orbital eccentricity (top, left), on orbital inclination (bottom, left), the spin of central BH (top, right), and perturber's inclination (bottom, right) for $n : k : m = -3 : 1 : 1$. The dots represent the values obtained from the semi-analytic calculation, and curves denote the obtained fitting. Note that both $\langle dL_z/dt \rangle$ and $\langle dQ/dt \rangle$ are normalised by multiplying a factor of $(\epsilon/M)^{-1}$.

both quantities increase as a increases. The difference between prograde and retrograde orbits is expected because the resonance occurs at smaller (larger) p values for prograde (retrograde) orbits for larger values of a (see vertical scale of lower panel in Fig. 6.1) for which the acting tidal force is greater.

- As for orbital inclination parameter x = cos I, we find that, as x increases, both dL_z/dt and dQ/dt tends to decrease regardless of the orbit's direction. This feature is again qualitatively similar to the trend found for $m = \pm 2$.

- Next, we note the dependence of resonance strength on inclination of the tidal parameter θ_{per}. For the sample resonance $-3 : 1 : 1$ and other resonance combinations with $m = \pm 1$, the change in dL_z/dt and dQ/dt is maximum for the perturber at an inclination of $\theta_{per} = 45°$. This behaviour can be qualitatively

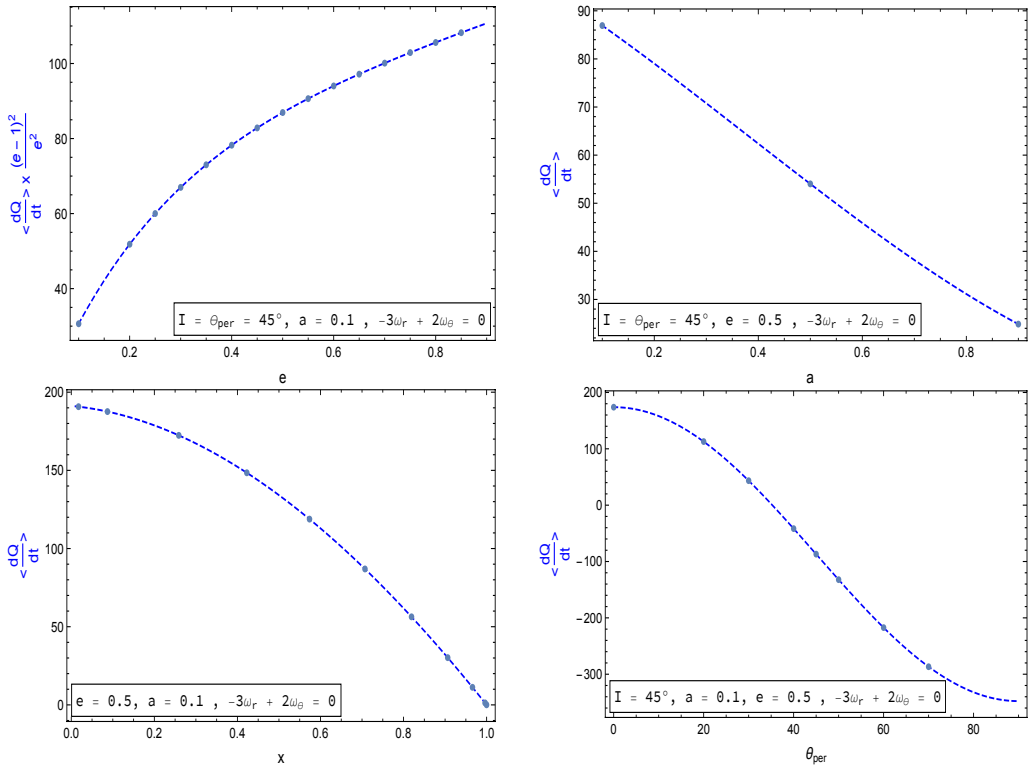

Fig. 6.10 Dependence of average change rate of the Carter constant (blue-dotted) on the orbital eccentricity (top, left), on orbital inclination (bottom, left), the spin of central BH (top, right), and perturber's inclination (bottom, right) for $n : k : m = -3 : 2 : 0$. The dots represent the values obtained from the semi-analytic calculation, and curves denote the obtained fitting. There is no change in the z-component of angular momentum given the axisymmetry of the $m = 0$ perturbation. Note that $\langle dQ/dt \rangle$ is normalised by multiplying a factor of $(\epsilon/M)^{-1}$.

explained for L_z using Newtonian arguments — the spherical harmonic decomposition of $(l = 2, m = \pm 2)$ mode of the tidal force and hence the torque turns out to be proportional to $\sin\theta_{\rm per}\cos\theta_{\rm per}$ [115]. This dependence also clarifies that $m = \pm 1$ resonance gives no contribution for an equatorial perturber ($\theta_{per} = 0°$) and polar perturber ($\theta_{per} = 90°$).

Resonances with $m = 0$

In Fig 6.10, we show the dependence on orbital and tidal parameter for an $m = 0$ mode focusing on $-3 : 2 : 0$ resonance. For this mode, the axisymmetry of the background Kerr spacetime remains intact. Therefore there is no jump induced in L_z. Nonetheless, we find that such resonances can still drive a jump in Q as shown in Fig 6.10. The dependency on $e, a,$ x are qualitatively similar to $m = 1$ resonances discussed above. In

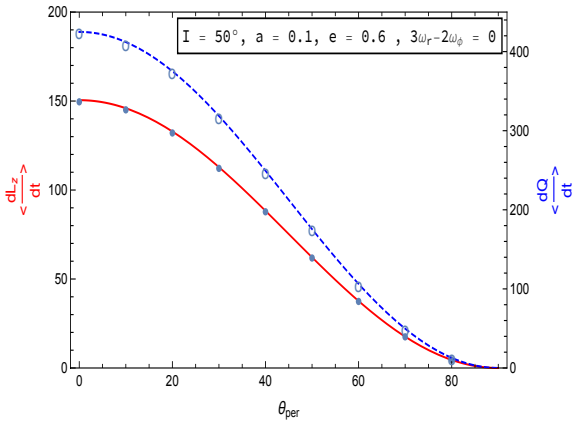

Fig. 6.11 Dependence of average change rate of the Carter constant (blue-dotted) on the perturber's inclination for a prograde orbit crossing $n : k : m = 3 : 0 : -2$. The dots represent the values obtained from the semi-analytic calculation, and curves denote the obtained fitting. Note that both $\langle dL_z/dt \rangle$ and $\langle dQ/dt \rangle$ are normalised by multiplying a factor of $(\epsilon/M)^{-1}$.

contrast, for $m = 0$ resonances, we find that the absolute jump size is largest when the perturber is aligned with the rotation axis of the SMBH *i.e.* $\theta_{per} = 90°$. This finding is important because $m = 0$ modes can cause a jump in Q, implying that other axisymmetric sources such as accretion disks can also induce a jump and impact waveforms through tidal resonances. Furthermore, tidal resonances with $m = 0$ modes are degenerate with self-force resonances, for which only the radial and polar integers (n and k) determine the resonance combination due to the axisymmetry of the Kerr space-time. In order to dissociate such resonances, waveforms need to be accurately modeled. If multiple tidal resonances due to the same perturber are encountered by an EMRI, they might be sufficient to break the degeneracy. For the completeness, in Fig 6.11 we show the dependence of the $m = 2$ mode on θ_{per}. The $\cos^2\theta_{\rm per}$ like dependence highlights that the jump size from $m = 2$ modes is maximum when the perturber is on the equatorial plane. This holds true irrespective of the orbit's direction.

6.4.4 Computation of jump and consistency with numerical evolution

The estimate of induced jump in conserved quantities across a resonance is evaluated using the analytical expression given by Eq. (6.11). For example, using this expression for an orbit crossing the $3 : 0 : -2$ tidal resonance, the maximum jumps (by setting

$q_{r0} = q_{\theta 0} = 0, q_{\phi 0} \sim 0.785$) induced in L_z and Q are

$$\Delta L_{z,max} = 7.4 \times 10^{-6}, \quad \Delta Q_{\rm max} = 1.8 \times 10^{-5}\,.$$

The above values are shown for an EMRI with mass ratio $\eta = 7.5 \times 10^{-6}$ (for $M = 4 \times 10^6 M_\odot$ and $\mu = 30{\rm M}_\odot$) and orbital parameters $\{a, p, e, x\} \sim \{0.9, 8.35, 0.62, 0.643\}$ at resonance under influence of a tidal perturber with mass $30M_\odot$ at a distance of 10 AU from the SMBH.

To perform a consistency check on the analytical calculation, we separately implemented the tidal force computed from the metric perturbation $h_{\alpha\beta}$ using the forced osculating orbital elements method [113, 116]. For the inclusion of radiation reaction effects, we employ a newly developed solver of the PN fluxes that takes into account the correction up to 5PN order and tenth order in eccentricity [61, 114]. We use 5PN fluxes to drive the inspiral in our osculating code instead of MST fluxes because PN fluxes are easier to implement and MST flux data sets are limited to $p \sim 6M$. In the osculating geodesics approach, the instantaneous tangential geodesics are referred to as osculating orbits. The transition between osculating orbits corresponds to the change in orbital elements. The inspiral motion is constructed from a smooth sequence of tangent geodesics where the driving forces are radiation reaction (5PN fluxes) and the tidal force caused by the perturber. We ran two simulations for an inspiral orbit with and without the effect of the tidal force taking the same initial conditions for the orbit as shown in Fig. 6.2. To extract the size of the jump, we compute the difference between the full trajectory (tidal force + 5PN) and adiabatic (only 5PN) trajectory.

In Fig. 6.12, we show the differences ΔL_z (left) and ΔQ (right). The apparent thickness of the lines shown in the figures is caused by oscillations on the orbital timescale. The orbit spends hundreds of cycles in the resonance regime which lasts about 17 days. It also shows that the tidal force significantly affects the inspiral around the resonance only.

An EMRI orbit can enter the resonance with any orbital phase thus affecting the size of the jump. We first find the value of $q_{\phi 0}$ at which $\Delta Q_{\rm max}$ matches ΔQ in the plot (right panel of Fig. 6.12) by solving

$$\Delta Q_{\rm max} \sin(-2q_{\phi 0}) = \Delta Q.$$

This yields $q_{\phi 0} \sim 0.23$. Then, we use this phase to check what the numerical value of ΔL_z should be based on the maximum value it can take analytically, *i.e.*, $\Delta L_{z,max}$. Our check yields $\Delta L_z \sim 3.2 \times 10^{-6}$, which agrees with the jump estimated from numerical

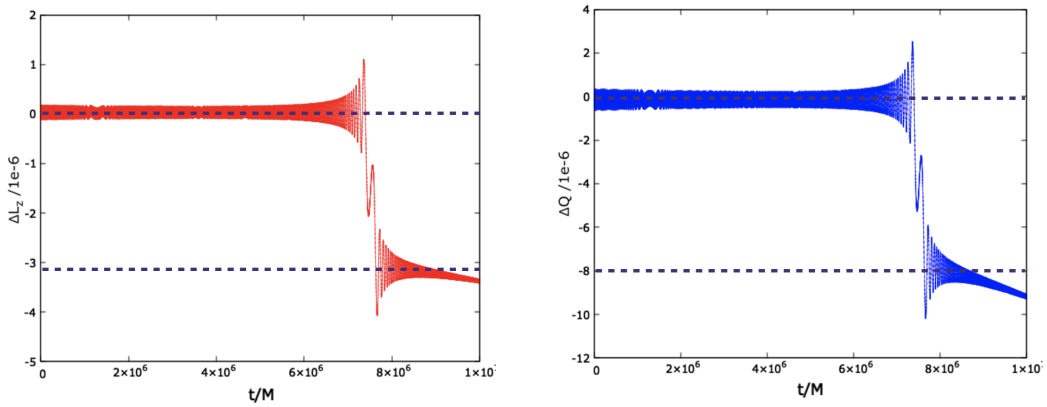

Fig. 6.12 The left figure shows the difference in L_z between the orbit evolved with and without tidal resonance effect. When the orbit enters resonance, there is a jump in the quantity. The fast oscillations correspond to orbital timescales. The gap between the horizontal dotted lines estimates the size of the jump. Similarly, the right figure shows a jump in the Carter constant.

evolution (left panel of Fig. 6.12). This computation verifies the jump estimated using the semi-analytic expression. Hereafter, we rely on the semi-analytical estimate of the jump (obtained using the numerical strategy discussed in Sec. 6.3.1) to study the impact of tidal resonances on gravitational waves.

6.4.5 Impact on gravitational waveform

For an EMRI source to be detectable by space-based interferometers, it must have an orbital frequency higher than about $f_{\rm LISA} = 10^{-4}$Hz. Using the approximation of Keplerian frequency when EMRI enters LISA band, we arrive at a rough condition on the semi-major axis $a_{\rm semi}$,

$$\frac{a_{\rm semi}}{M} < 20 \times \left(\frac{M}{4\times 10^6 M_\odot}\right)^{-2/3} \left(\frac{f_{\rm LISA}}{10^{-4}{\rm Hz}}\right)^{-2/3}. \tag{6.19}$$

Using this rough estimate, an EMRI with $a_{\rm semi}$ less than $20M$ will lie in the observable band. Low-order resonances encountered by both prograde and retrograde orbits lie well within LISA frequency band for the central black hole less massive than $4\times 10^6 M_\odot$.

As discussed in previous sections, an orbit passing through a resonance can lead to a sudden change in constants of motion. This change means that the evolution post-resonance can become out of phase with that of the pre-resonance evolution. Therefore, we cannot match both parts with the same template. This can hamper the

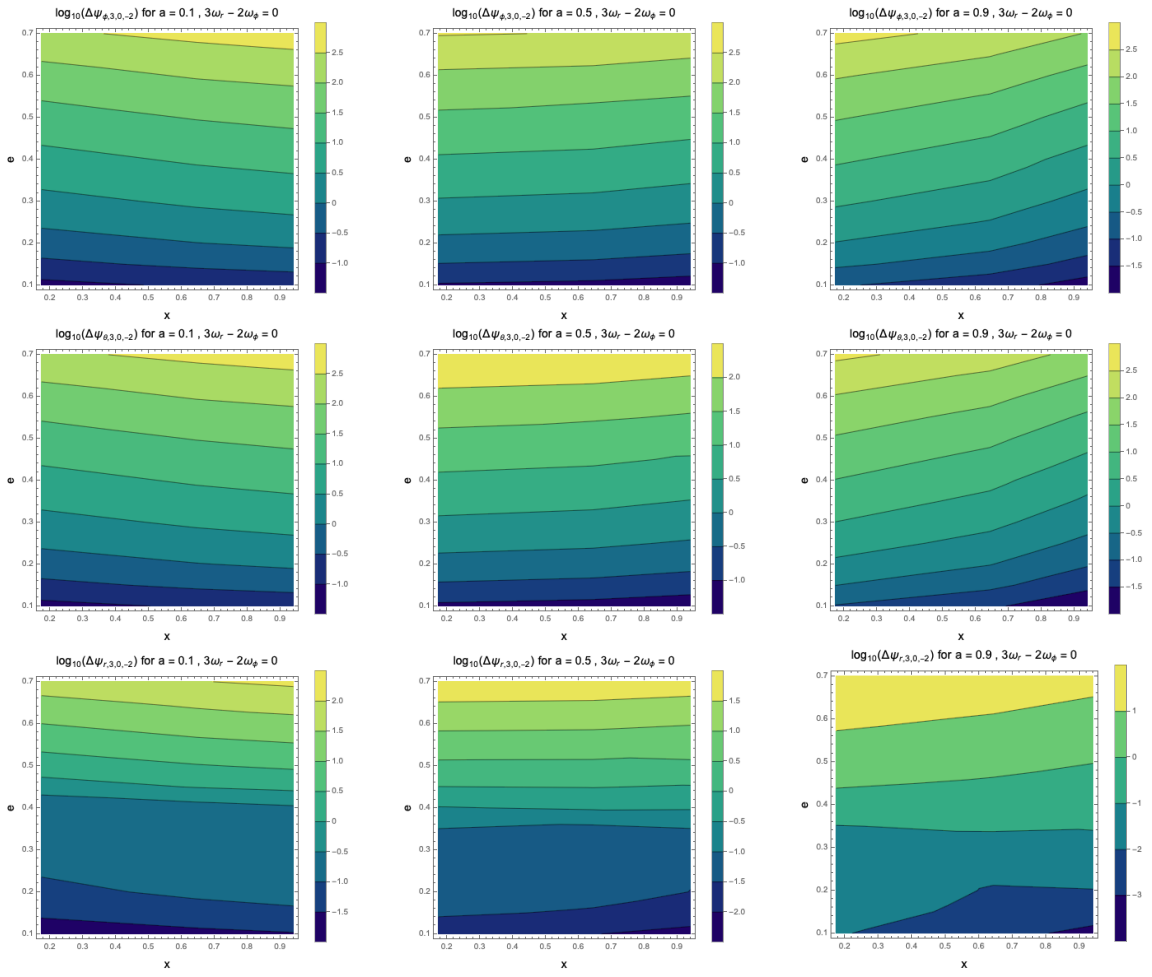

Fig. 6.13 Accumulated phase $\Delta\Psi_i$ for spin parameter $a = 0.1, 0.5, 0.9$ for a prograde orbit crossing the $3:0:-2$ resonance in the x - e plane. Top, middle and bottom panels correspond to $\Delta\Psi_\phi$, $\Delta\Psi_\theta$ and, $\Delta\Psi_r$, respectively. The phase shift is computed for an EMRI with $M = 4 \times 10^6 M_\odot, \mu = 30 M_\odot$ under the influence of a tidal perturber with mass $M_\star = 30 M_\odot$ at a distance of 10 AU from the central SMBH. Results for different sets of parameters can be estimated from the scaling relation given in Eq. (6.21).

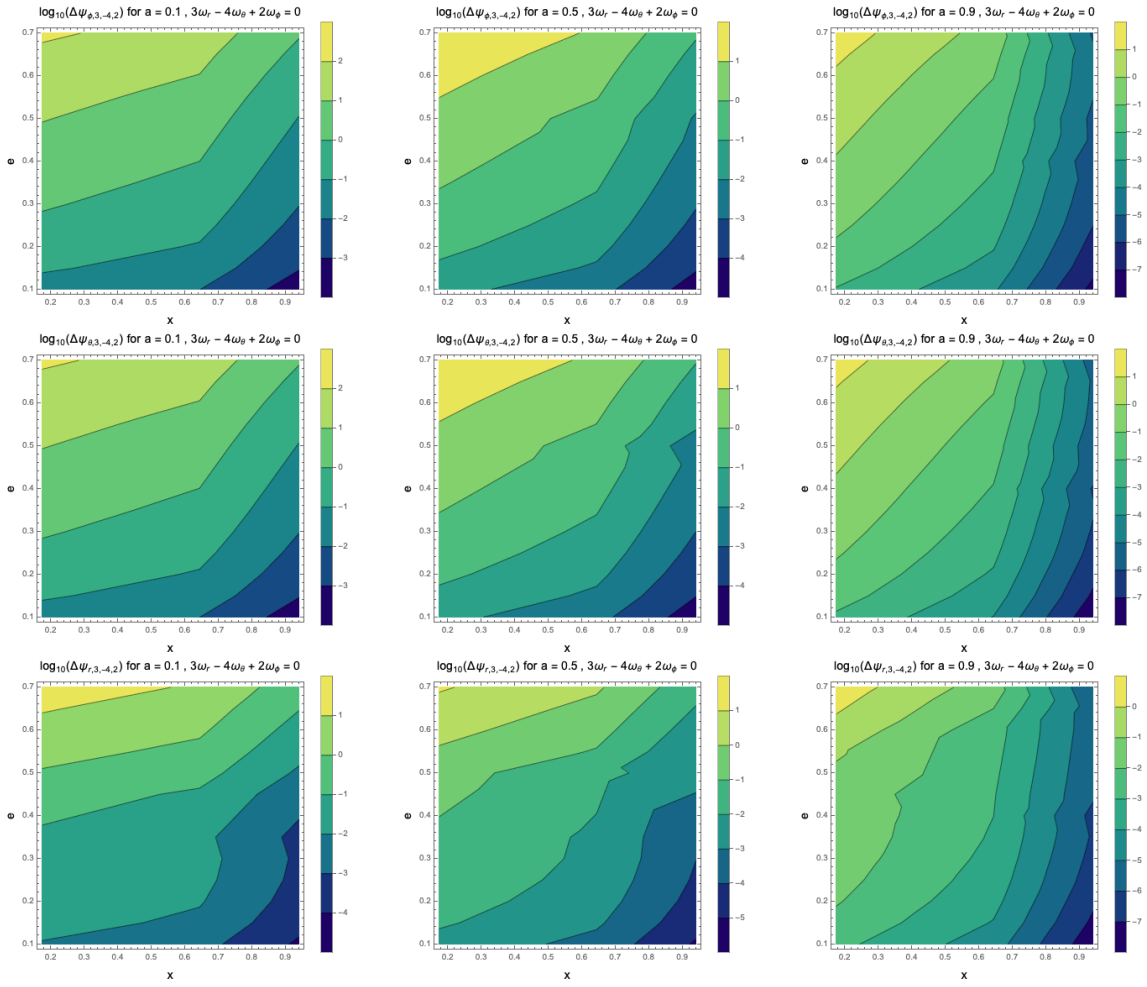

Fig. 6.14 Accumulated phase $\Delta\Psi_i$ for spin parameter $a = 0.1, 0.5, 0.9$ for a prograde orbit crossing the $3:-4:2$ resonance in the $x-e$ plane. Top, middle and bottom panels correspond to $\Delta\Psi_\phi$, $\Delta\Psi_\theta$ and, $\Delta\Psi_r$, respectively. The phase shift is computed for an EMRI with $M = 4\times10^6 M_\odot, \mu = 30M_\odot$ under the influence of a tidal perturber with mass $M_\star = 30M_\odot$ at a distance of 10AU from the central SMBH. Results for different sets of parameters can be estimated from the scaling relation given in Eq. (6.21).

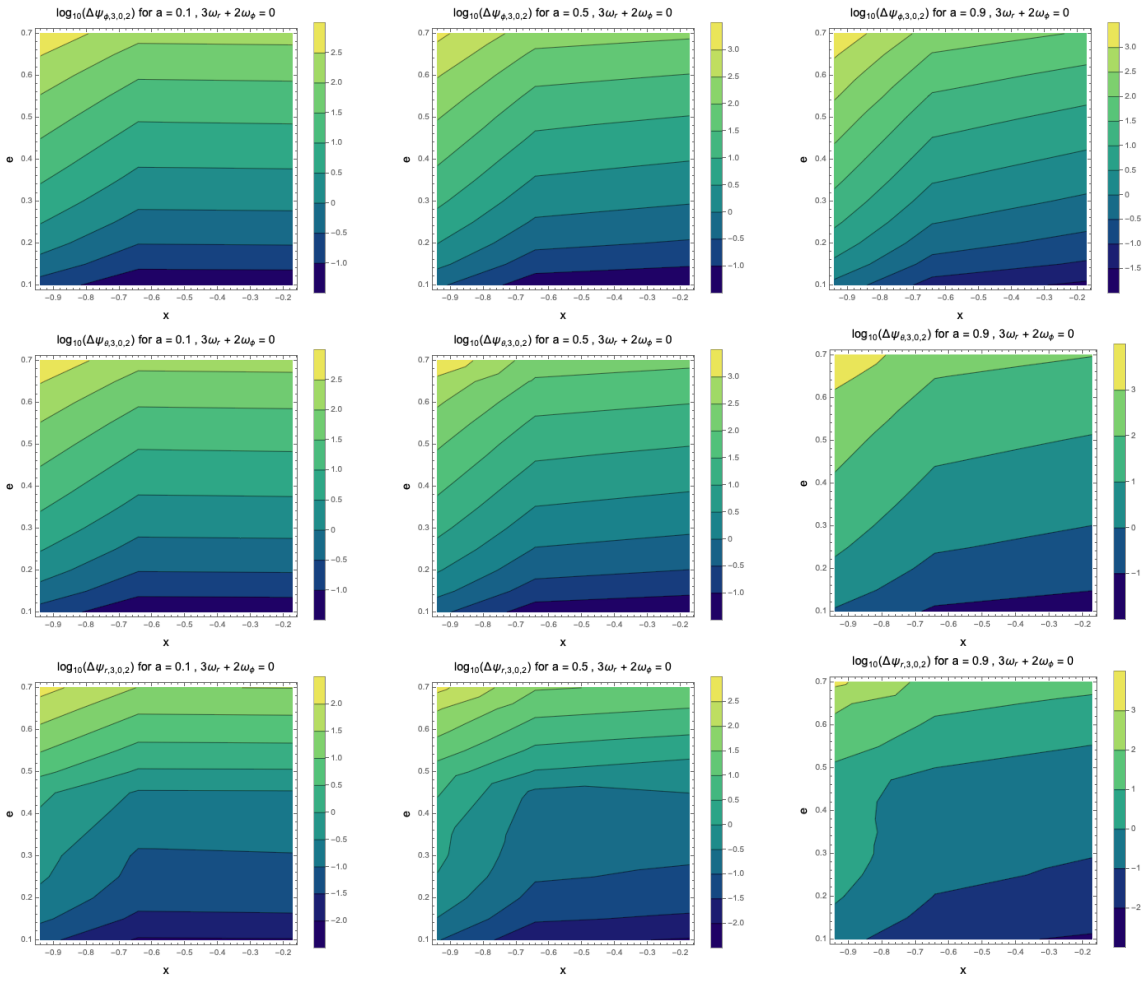

Fig. 6.15 Accumulated phase $\Delta\Psi_i$ for spin parameter $a = 0.1, 0.5, 0.9$ for a retrograde orbit crossing the $3:0:2$ resonance in the x - e plane. Top, middle and bottom panels correspond to $\Delta\Psi_\phi$, $\Delta\Psi_\theta$ and, $\Delta\Psi_r$, respectively. The phase shift is computed for an EMRI with $M = 4 \times 10^6 M_\odot, \mu = 30 M_\odot$ under the influence of a tidal perturber with mass $M_\star = 30 M_\odot$ at a distance of 10AU from the central SMBH. Results for different set of parameters can be estimated from scaling relation given in Eq. (6.21).

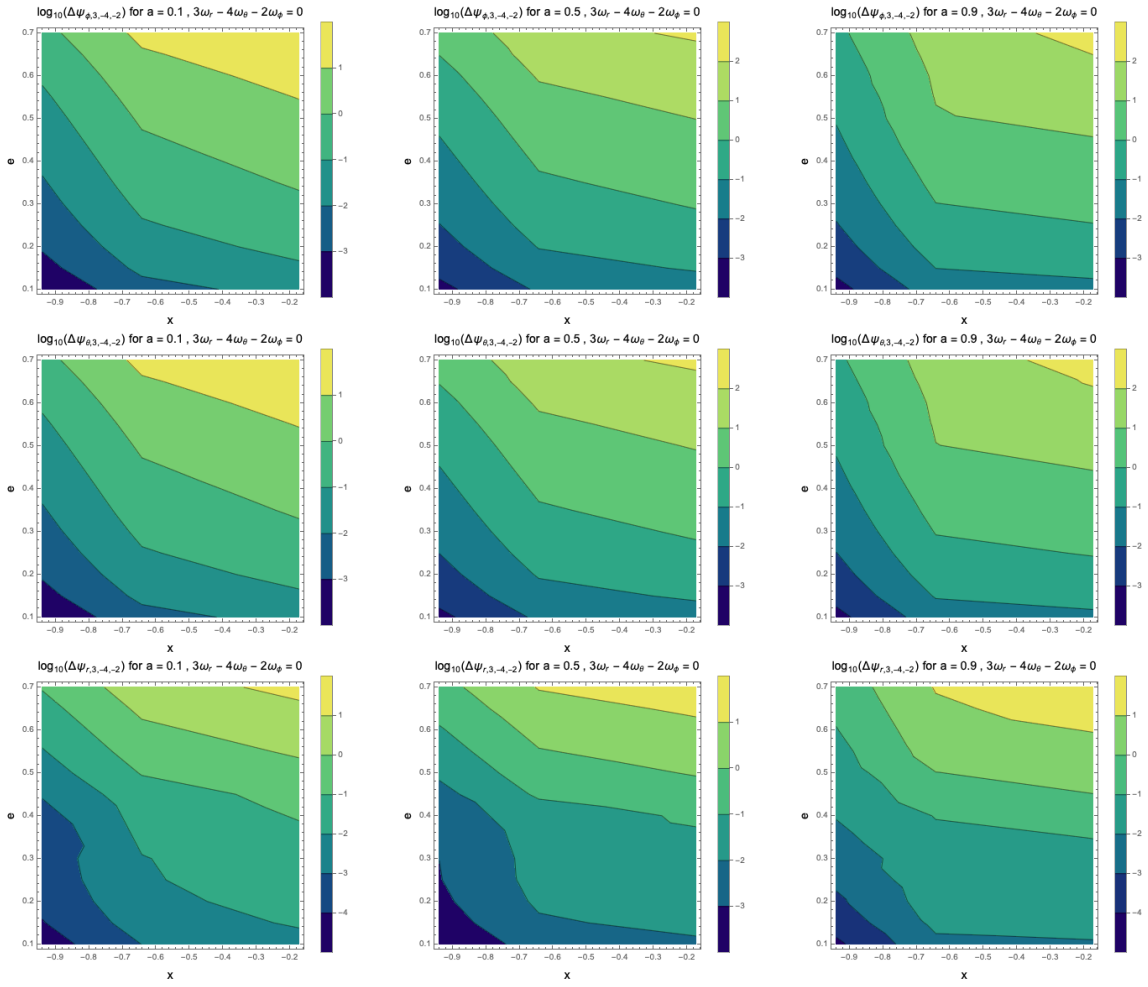

Fig. 6.16 Accumulated phase $\Delta\Psi_i$ for spin parameter $a = 0.1, 0.5, 0.9$ for a retrograde orbit crossing the $3:-4:-2$ resonance in the $x-e$ plane. Top, middle and bottom panels correspond to $\Delta\Psi_\phi$, $\Delta\Psi_\theta$ and, $\Delta\Psi_r$, respectively. The phase shift is computed for an EMRI with $M = 4\times10^6 M_\odot, \mu = 30M_\odot$ under the influence of a tidal perturber with mass $M_\star = 30M_\odot$ at a distance of 10AU from the central SMBH. Results for different set of parameters can be estimated from scaling relation given in Eq. (6.21).

detection of EMRIs using standard matched filtering techniques. Thus, it is important to study their impact on EMRI waveforms. To estimate the effect, we study the deviation in the orbital phase, which can be evaluated as

$$\Delta\Psi_\phi = \int_0^{T_{\rm plunge}} 2\Delta\omega_\phi dt\,. \tag{6.20}$$

The accumulation in phase is integrated from the resonance time up to the plunge time $T_{\rm plunge}$. We evolve two orbits one with and without ΔJ_i included. At each time ω_ϕ for both the orbits is compared and the difference in frequencies for these two evolutions is given by $\Delta\omega_\phi$. The factor of 2 in Eq. (6.20) is because the strongest harmonic in GWs is the quadrupolar mode ($l = 2, m = 2$). The phase evolution of waveform depends on the combination of three orbital phases: radial, polar, azimuthal. Therefore, in a similar manner, we also evaluate radial and polar accumulated phase shift, *i.e.*, $\Delta\Psi_r$ and $\Delta\Psi_\theta$, respectively. LISA has a remarkable sensitivity to the phase resolution of EMRI measurements, which is roughly estimated as $\Delta\Psi_\phi \sim 0.1$, assuming SNR to be 20 [117, 6]. The resonance causes a shift in fundamental frequencies that is not replicated by adiabatic evolution, thus resulting in gradual dephasing of waveforms.

In our analysis, we show that in a significant fraction of the parameter space EMRIs are likely to experience a tidal resonance (or multiple) that induces phase shift greater than 0.1 rad making the effect detectable. Therefore, including the signature of resonances in waveform modeling is necessary to test GR with precision and allows a study of the environment around an EMRI. To compute the phase shift we set $M = 4 \times 10^6 M_\odot$, $\mu = M_\star = 30 M_\odot$ and $R = 10$AU. This distance as twice as far as in [6] to give a more conservative estimate. In Fig 6.13, the accumulation in phase is shown for prograde orbits crossing the $3:0:-2$ resonance in the x - e plane for different spin parameters of the SMBH. In the top panel, $\Delta\Psi_\phi$ is shown. The whole parameter space except for low eccentricity orbits (< 0.2) is affected by this resonance as the phase shift lies in the detectable range of LISA. Middle and bottom panels show the affected parameter space for $\Delta\Psi_\theta$ and $\Delta\Psi_r$, respectively. The dephasing increases with increasing eccentricity and mildly depends on the spin parameter. Since this resonance is encountered early in the inspiral phase (see upper panel of Fig 6.2), the phase is accumulated over hundreds of thousands of cycles before plunge and therefore affects most of the parameter range.

In Fig. 6.14, a similar plot is shown for a prograde orbit crossing the $3:-4:2$ resonance. In this case, dephasing is sensitive to changes in inclination and spin parameter. For the case $\Delta\Psi_\phi$ (top panel), orbits with low eccentricity ($\lesssim 0.3$) and

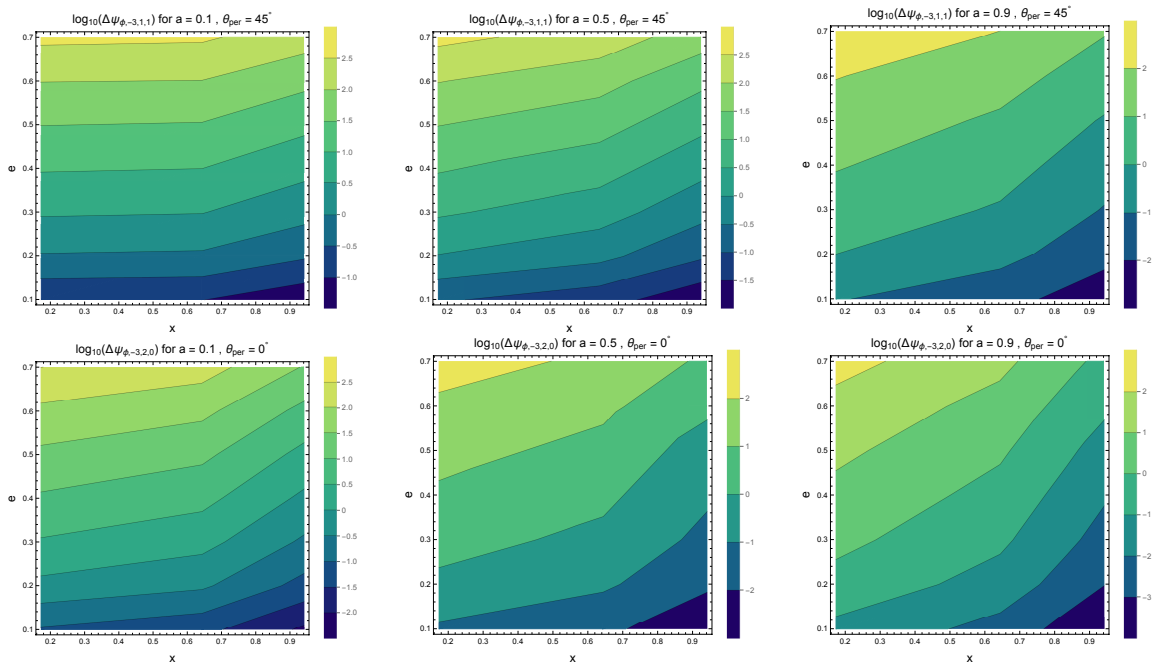

Fig. 6.17 Log of accumulated phase $\Delta\Psi_\phi$ for spin parameter $a = 0.1, 0.5, 0.9$ for a prograde orbit crossing the $-3:1:1$ (top panel) and $-3:2:0$ (bottom panel) resonance in the x - e plane. The phase shift is computed for an EMRI with $M = 4\times10^6 M_\odot, \mu = 30M_\odot$ under the influence of a tidal perturber with mass $M_\star = 30M_\odot$ at a distance of 10 AU from the central MBH. Results for different sets of parameters can be estimated from the scaling relation given in Eq. (6.21).

small inclination ($\lesssim 45°$) have phase shift smaller than 0.1, implying that the tidal resonance does not cause an observable effect in this range. As the spin is increased, a larger region of the parameter space is in the non-observable range. For $a = 0.9$, only orbits with high inclination ($\gtrsim 50°$) and high eccentricity have a detectable tidal effect. The middle panel shows $\Delta\Psi_\theta$ which is of the same order as $\Delta\Psi_\phi$, and the bottom panel shows $\Delta\Psi_r$.

In Fig. 6.15 and Fig. 6.16, we show the accumulated phase shift for retrograde orbits crossing the $3:0:2$ and $3:-4:-2$ resonances, respectively, for different spin parameters. As is clear from the figures, dephasing is larger compared to prograde orbits. This is expected because the value of p is larger for retrograde orbits (see the lower panels of Fig. 6.2), causing the effect of tidal force to be larger compared to prograde orbits. In contrast to the trend observed for prograde orbits, dephasing increases as the spin parameter increases.

In Fig 6.17, $\Delta\Psi_\phi$ is shown for prograde orbits crossing the $-3:1:1$ (top panel) and $-3:2:0$ (bottom panel) resonances in the x - e plane for different spin parameters

of the MBH. The whole parameter space except for low eccentricity orbits and/or for a large spin is measurably affected by the $-3:1:1$ resonance. In a similar way, the $-3:2:0$ resonance impacts a large parameter space. The dephasing increases with increasing eccentricity. Since both sample resonances are encountered early in the inspiral phase (see the left panel of Fig 6.1), the dephasing accumulates over hundreds of thousands of cycles before the plunge, and therefore affects most of the parameter range.

The accumulated phase shown for the sample resonances is calculated for fixed masses of the MBH, EMRI and the tidal perturber. The accumulated phase $\Delta\Psi'_{nkm}$ for a different set of parameters $M', \mu', M'_\star, R', \mathrm{x}'_\star$ simply scales as

$$\Delta\Psi' = \Delta\Psi\left(\frac{M'}{M}\right)^{7/2}\left(\frac{\mu'}{\mu}\right)^{-3/2}\left(\frac{M'_\star}{M_\star}\right)\left(\frac{\mathrm{x}'_\star}{\mathrm{x}_\star}\right)\left(\frac{R'}{R}\right)^{-3}. \tag{6.21}$$

So far, our results suggest that resonance jumps are sensitive to intrinsic orbital parameters, especially the orbital phases at resonance. Also, dephasing due to low-order tidal resonances can strongly impact the EMRIs detectable by LISA, assuming such tidal perturbers exist. Consequently, the waveform evolution becomes out of phase, compared to a template neglecting resonances — reducing the detection rate because the signal-to-noise ratio falls as the phase error accumulates. It calls for careful modeling of waveforms that correctly detect EMRIs and estimate the parameters of EMRI and perturber. This serves as our motivation for the next chapter.

Chapter 7

Modeling transient resonances in EMRIs

7.1 Executive summary

The observation of EMRI gravitational waves will offer stringent tests on general theory of relativity, and provide a wealth of information about the dense environment in galactic centers. To unlock such potential, it is necessary to correctly characterize EMRI signals. However, resonances are phenomena that occurs in EMRI systems and can impact parameter inference, and therefore the science outcome, if not properly modeled. The previous chapter has demonstrated that tidal resonances induced by the tidal field of a nearby astrophysical object alters the orbital evolution, leading to a significant dephasing across observable parameter space. Here, we explore how to model resonances and develop an efficient implementation.

If the resonance effects are large enough, post-resonance waveform evolution can become totally out of phase compared with the template neglecting resonances. It requires a practical, *i.e.*, fast and accurate, model to efficiently detect EMRIs and correctly estimate the parameters of EMRI and the perturber. A recent work [81] presented a partially phenomenological Effective Resonance Model (ERM) with additional free parameters for the resonance jumps. We use techniques from this model to incorporate tidal resonances that are constrained by physics, and hence our model is no longer "effective" in the above sense.

Here, we go beyond semi-analytic fits to resonant jumps by proposing a new waveform model taking the resonances into account. A consistency check confirms that the obtained fitting formulae accurately estimate the jump size by comparing it with the osculating elements trajectory [113]. Hence, these fittings allow incorporating

resonances at inexpensive computational costs. To model the jump, we use a step function approach rather than a 'smooth' impulse function [81], and show that this simplified treatment is enough to maintain the accuracy required for data analysis. The accuracy of post-resonance evolution depends far more on the fitting formulae than the profile of the jump. For a small tidal perturbation (examined here), the phase accumulated during the passage of the resonance is negligible, which makes the step function approach suitable. In case of large tidal perturbations (sustained resonances), the impulse function must be carefully selected. However, this occurs in a less astrophysically relevant region of the parameter space, and is beyond the scope of our work.

With our model, we explore the parameter measurement precision when tidal resonances are present and study the parameter bias induced by ignoring them [118]. Based on the studied EMRI configurations, we find that biases are larger than noise-induced statistical errors. As a result of our findings, parameter estimates of resonant EMRIs will likely be biased if resonances are not taken into consideration in parameter estimation models. The Fisher matrices are also used to discuss the threshold magnitude of tidal perturbation below which the observed signal cannot be interpreted as indicative of tidal perturbation. Modeling of self-force resonances can also be carried out using the implementation presented in this study, which will be crucial for EMRI waveform modeling.

7.2 Motivation

The event rate of EMRIs depends on highly uncertain parameters such as the stellar density profile around each galactic center, the population of compact objects, and rates of dynamical processes that can lead to the capture of the stellar-mass body in the gravitational potential of a MBH [24, 23, 37–40]. Therefore, the expected range varies from a few to a few hundred EMRI signals over a four-year mission duration for LISA [117, 40]. To take the full advantage of the scientific potential of such astrophysical sources, data analysis methods rely on theoretical waveform templates to compare against the data. Thus, we must have waveforms for generic orbits that are modelled accurately within a fraction of a radian, even after hundreds of thousands of orbital cycles. Another necessity is that the templates should cover the high dimensional parameter space of possible EMRI configurations and their generation must be fast enough to be able to deal with templates in large numbers. Significant efforts by the scientific community focusing on the computation of the self-force, together with LISA

working groups and mock data challenges, are concentrated on realizing the goal of accurate and fast waveform modeling [61, 76, 77, 119–121].

Environmental effects will introduce systematic parameter estimation errors, potentially spoiling the efforts of the community towards accurate waveform models and precision gravitational wave astrophysics. This can lead to the erroneous conclusion that the data conflicts with GR [6]. Thus, quantifying and modeling resonances resulting from self-force and external tidal fields on inspirals is another challenge to overcome, if we want to perform precision tests of GR [6, 122]. Our research is motivated by this issue, and we investigate the modeling of resonances induced by an external tidal field. We developed for the first time the implementation of a realistic EMRI waveform passing through a resonance. This is essential for the scientific success of LISA. In particular, full waveforms will be essential for the search [99] and parameter estimation of EMRIs [81]. The insights gained from this work will be also relevant to self-force resonances, which we do not model as there are no precise jump size estimations available at present, but we hope they will be available in the near future [74, 123–125].

7.3 Modeling Tidal Resonances

In this section, we first review how to evaluate the expected accuracy and systematic bias in parameter estimation, based on Fisher analysis. Next, we introduce the structure of the resonance model (RM), which is used to incorporate tidal resonances in waveforms and investigate the loss of signal and the systematic bias due to inaccurate modeling.

7.3.1 Gravitational wave data analysis

The output data $s(t)$ of a gravitational detector consists of random noise, $n(t)$ and possibly a gravitational wave signal $h(t;\boldsymbol{\lambda})$ characterized by a set of parameters $\boldsymbol{\lambda} = [\lambda_1 \dots \lambda_n]$ in n-dimensional parameter space.

$$s(t) = h(t;\boldsymbol{\lambda}) + n(t). \tag{7.1}$$

We assume that noise is given by a weakly stationary, Gaussian random process with zero mean and a signal is present in the detector output. Under these assumptions, the Likelihood for the parameters $\boldsymbol{\lambda}$ () is given by [126],

$$p(s|\boldsymbol{\lambda}) \propto \exp\left(-\frac{1}{2}\langle s - h(\boldsymbol{\lambda})|s - h(\boldsymbol{\lambda})\rangle\right), \tag{7.2}$$

where $\langle\cdot|\cdot\rangle$ is a noise-weighted inner product defined as,

$$\langle a(t)|b(t)\rangle := 4\ \mathrm{Re}\int_0^\infty \frac{\tilde{a}^*(f)\tilde{b}(f)}{S_n(f)}\,df\,. \tag{7.3}$$

$S_n(f)$ is the power spectral density (PSD) of the noise and the variable with tilde indicates the Fourier transform of the corresponding time series data. Additionally, it is customary to define the signal-to-noise ratio (SNR),

$$\rho = \sqrt{\langle h|h\rangle}, \tag{7.4}$$

which characterizes the detectability of a signal by a detector with a given noise power spectrum.

We recall two other quantities defined in Chapter 2 that serve as a measure of similarity between two template waveforms $h_a = h(t;\boldsymbol{\lambda}_a)$ and $h_b = h(t;\boldsymbol{\lambda}_b)$, the Overlap $\mathcal{O}(h_a,h_b)$ and Mismatch $\mathcal{M}(h_a,h_b)$, by

$$\mathcal{O}\langle h_a,h_b\rangle = \frac{\langle h_a|h_b\rangle}{\sqrt{\langle h_a|h_a\rangle\langle h_b|h_b\rangle}} \tag{7.5}$$

$$\mathcal{M}(h_a,h_b) = 1-\mathcal{O}(h_a,h_b). \tag{7.6}$$

If we want to estimate how accurately parameters are measured, it is helpful to calculate the Fisher Information matrix Γ_{ij}. When a strong signal with parameters $\boldsymbol{\lambda}$ is present in the detector output, the likelihood is strongly peaked in the parameter space at the best-fit (BF) parameter set close to the true values. Namely, the measurement error

$$\Delta\boldsymbol{\lambda} = \boldsymbol{\lambda}_{\mathrm{BF}} - \boldsymbol{\lambda}\,, \tag{7.7}$$

is small. Then, we expand $h(\boldsymbol{\lambda})$ up to linear order in $\Delta\boldsymbol{\lambda}$ (truncating higher orders terms given the smallness of $\Delta\boldsymbol{\lambda}$ in the strong signal limit) and substitute it into (7.2). On substitution, the Likelihood function becomes

$$p(s|\boldsymbol{\lambda}) \propto \exp\left(-\frac{1}{2}\sum_{i,j}\Gamma_{ij}\Delta\lambda^i\Delta\lambda^j\right). \tag{7.8}$$

where

$$\Gamma_{ij} = \langle\frac{\partial h}{\partial\lambda^i}\Big|\frac{\partial h}{\partial\lambda^j}\rangle. \tag{7.9}$$

The probability function shows that the inverse of Γ_{ij}, known as the covariance matrix, contains information about variances of parameter measurement error (diagonal elements) as well as correlations of errors among different parameters (off-diagonal elements). In particular, the statistical error in the estimate of the parameter λ_i can be evaluated by[1]

$$\Delta\lambda_i^{stat} = \sqrt{(\Gamma^{-1})^{ii}}\,. \tag{7.10}$$

From (7.9), the Fisher Matrix scales as $\sim \rho^2$, therefore $\Delta\boldsymbol{\lambda}$ scales as $\sim \rho^{-1}$.

Besides the errors induced by noise, there can be a possible systematic uncertainty that is not parameterized in our waveform models. For instance, if we use an inaccurate waveform model $h_m(\boldsymbol{\lambda})$ to estimate the parameters $\boldsymbol{\lambda}_0$ of a signal actually described by a model $h_t(\boldsymbol{\lambda})$, the recovered parameters will be affected by systematic errors given by [118],

$$\Delta\lambda_i^{sys} = (\Gamma^{-1})^{ki}\langle\partial_k h(\boldsymbol{\lambda}_0)|h_t(\boldsymbol{\lambda}_0) - h_m(\boldsymbol{\lambda}_{\rm BF})\rangle\,. \tag{7.11}$$

This error is independent of the strength of the signal. Therefore, if exists, it will dominate over noise-induced error, whenever the data quality is sufficiently good.

In this work, we evaluate the above mentioned errors, by comparing two kinds of waveforms: resonant waveforms which are produced using the AAK module [67, 127] implemented in the RM (discussed in Sec. 7.3.2), and non-resonant waveforms where we "turn-off" the jumps induced by tidal resonances. For our Fisher analysis, we assume that from the data we determine the following ten parameters:

$$\boldsymbol{\lambda} = \left(\log_{10}\frac{M}{M_\odot}, \log_{10}\frac{\mu}{M_\odot}, a, p, e, \mathrm{x}, q_r, q_\theta, q_\phi, \widetilde{\epsilon}\right)\,, \tag{7.12}$$

where q_r, q_θ, q_ϕ are the initial phases of an EMRI orbit and $\widetilde{\epsilon}$ is the normalized (by the fiducial value of ϵ) tidal parameter. These intrinsic parameters govern the detailed dynamical evolution of a system, regardless of where or how an observer observes it. For computational convenience, we are not including extrinsic parameters such as the sky location angles (θ_S, ϕ_S) and the angles pointing to the direction of the MBH's spin (θ_K, ϕ_K) in this list. The luminosity distance D_L of the source is rescaled for each waveform to fix the SNR to 30. Our fiducial values for the masses of the EMRI system are $M = 10^6 M_\odot$ and $\mu = 30 M_\odot$. The perturber of mass $M_\star = 30 M_\odot$ is placed at a distance of 5AU on the equatorial plane, resulting in the following fiducial tidal parameter $\epsilon \sim 2.3 \times 10^{-13}$ for $\mathrm{x} = 1$. For every Fisher matrix computed, we examine

[1] In our analysis, the waveform derivatives $\partial_j h$ are computed numerically using the five-point stencil formula such that the numerical error scales at fourth order in the derivative spacing.

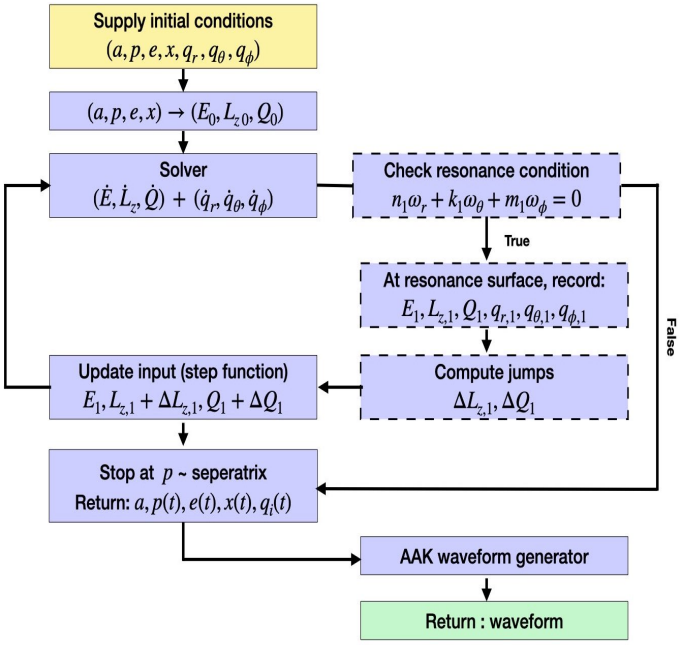

Fig. 7.1 Workflow of Resonance Model.

its validity by checking the condition number and the linear signal approximation in which the Fisher matrix analysis is valid.

7.3.2 Resonance model

The Effective Resonance Model (ERM) is a phenomenological model developed recently to study EMRI resonances. It was constructed using the resonance jumps as free parameters and applied to the case of self-force resonances [81]. Following the implementation of [81], we extend the ERM to incorporate tidal resonances. We refer to our working code as the resonance model (RM); the word "Effective" has been discarded since we are not using the resonance jumps as free parameters. The flowchart is shown in Fig 7.1. The solver employs flux and phase evolution equations to obtain the trajectory, given some initial condition (E_0, L_{z0}, Q_0). Our calculations use the fifth order post-Newtonian (5PN) fluxes generated by the post-Newtonian (PN) approximation in first-order black hole perturbation theory [61]. The right-hand side of the phase evolution equations are corresponding Kerr orbital frequencies [49] *i.e.* $dq_i/dt = \omega_i$. The resonance condition is checked at each time step of the solver (using the adaptive time step and event handling tool in the `Solve-ivp` ODE package in `Python`) for some low order integer $m, k,$ and n. If the resonance condition is satisfied, we record the orbital parameters at the resonance surface and use them to estimate the

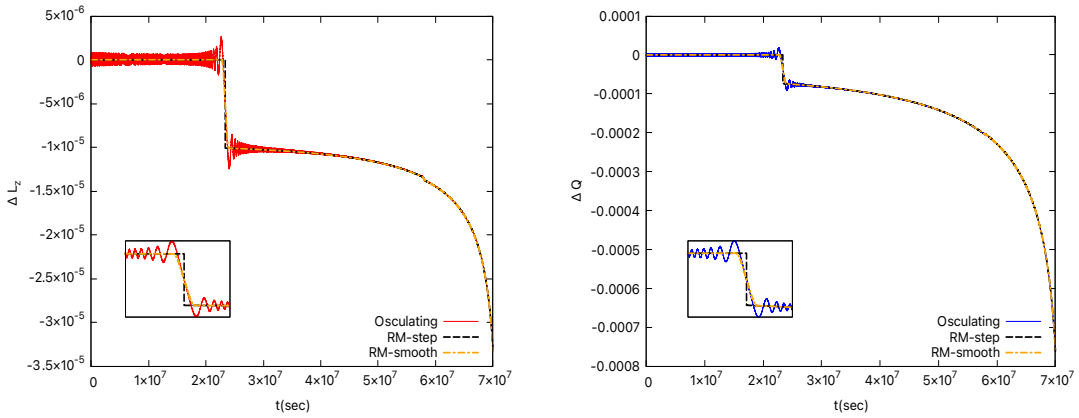

Fig. 7.2 The left figure shows the difference in L_z between the orbits evolved with and without tidal resonance effect. When the orbit undergoes a resonance, there is a jump in the action variables $\mathbf{J}$. Black dashed lines illustrate the evolution of ΔL_z using a step impulse function in the RM, whereas orange (dashed-dotted) lines represent evolution tracks using a 'smooth' impulse function. Similarly, the right figure shows the evolution of the Carter constant Q. The initial conditions for this orbit are $(a, p, e, \mathrm{x}) = (0.9, 11.8, 0.8, 0.0187)$, and the trajectory crosses two resonances, $n : k : m = 3 : 0 : -2$ and $n : k : m = 3 : -4 : -2$ around $t \sim 2.2 \times 10^7$and $\sim 5.8 \times 10^7$, respectively. The fast oscillations in both figures correspond to timescales of the orbital motion. The inset plot shows zoomed-in evolution near the $3 : 0 : -2$ resonance.

jump size of the resonance due to the tidal field using the analytic fits obtained from our semi-analytic calculations [100]. Once the jump sizes ΔL_z and ΔQ are measured, we update the constants of motion for the next time step using a step function. In [81], the resonance jump is implemented using a "smooth" impulse function. In this study, however, we find that using a smooth function instead of a step function did not affect our results (shown in Fig 7.2). Consequently, we choose to implement the faster and simpler step function. We stop the evolution of the trajectory once the separatrix, where ω_r vanishes, is reached. The orbital parameters and phases are then fed to the Augmented Analytic Kludge (AAK) module to obtain the waveform. Our code makes use of the modular FEW package [127].

7.4 Results

In this section, we compare the jump obtained from analytic fits with the result obtained by the numerical osculating code, to find a good agreement between the two. Using the RM and Fisher matrices, we show mismatches for different initial conditions

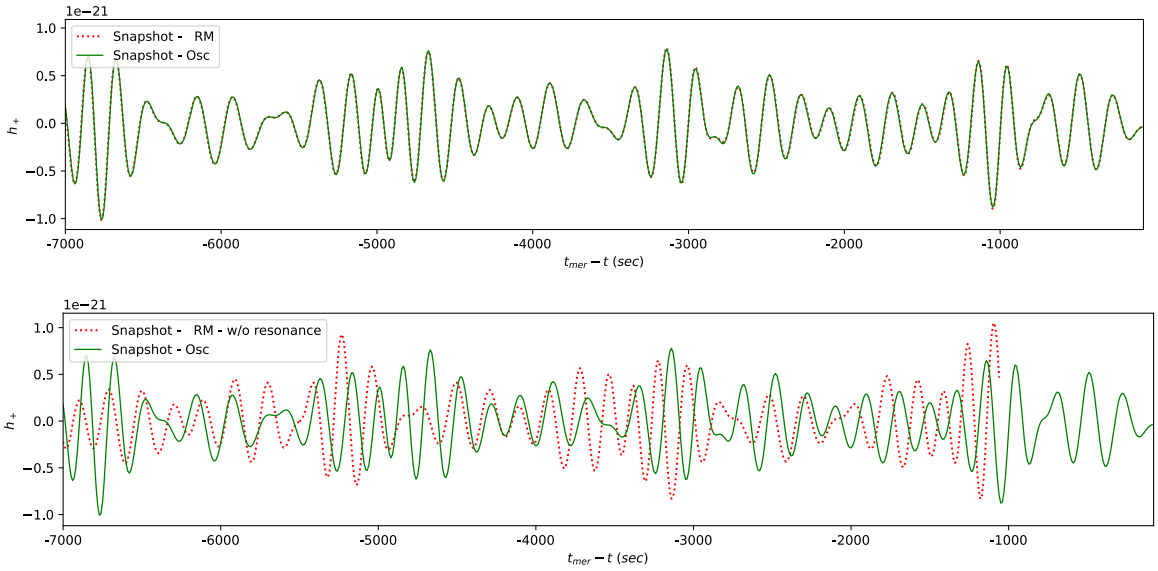

Fig. 7.3 Snapshot of h_+ waveforms obtained from the RM and osculating method a few hours before plunge. Top panel: comparison of $h+$ from RM (with resonance jump included) and the one from the osculating method. Lower panel: comparison of $h+$ from the RM without resonance jump and the one from the osculating method.

IC	(a, p, e, x)	$t_{3:0:-2}$ $(10^7 \mathrm{sec})$
1	$0.1, 11.5, 0.7, 0.642$	~ 1.64
2	$0.5, 10.5, 0.8, 0.642$	~ 1.85
3	$0.7, 11.0, 0.7, 0.342$	~ 1.71
4	$0.9, 11.8, 0.8, 0.087$	~ 2.24

Table 7.1 Initial conditions for EMRI orbit. The last column shows the time of $n : k : m = 3 : 0 : -2$ resonance encounter.

and assess the measurement precision of EMRI orbital parameters and tidal parameters. We also compute the systematic bias that would be induced by ignoring resonances.

7.4.1 Mismatch analysis

Dephasing induced by tidal resonances accumulates over the inspiral, resulting in a decrease in the overlap (7.5) between resonant and non-resonant waveforms after resonance encounter. In this section, we analyze the evolution of the mismatch $\mathcal{M}$ (7.6) as a function of the final time for different initial conditions listed in Table 7.1. These conditions were chosen since they cover a broad range of possibilities for astrophysical

EMRI events that may be measured by future low-frequency GW missions. All initial conditions are subject to a 30 $M_\odot$ tidal perturber at a distance of 5 AU on the equatorial plane, and the EMRI inspiral lasts for $\sim 1-2$ years. The parameters chosen for tidal perturber are motivated by the Fokker-Planck simulation study that suggests a population of stellar-mass BHs at a median distance of $\sim$ 5AU [38]. We note that for the chosen set of parameters $\tau_{\rm res} \sim \tau_{\rm td}$, thereby violating the stationary perturbation approximation. However, we leave the impact of a dynamical tidal perturber on the resonances for future work.

We first determine the consistency of the resonance model by comparing its trajectory evolution with the numerical osculating trajectory. The forced osculating orbital elements method [113, 116] uses the tidal force computed from the metric perturbation $h_{\alpha\beta}$ and for the inclusion of radiation reaction effects, 5PN fluxes [61, 114] are employed. Using the osculating code, we ran two simulations for an inspiral orbit — with and without the effect of the tidal force with the same initial conditions. To extract the jump size, we compute the difference (ΔL_z and ΔQ) between the full trajectory (tidal force + 5PN) and adiabatic (only 5PN) trajectory. A similar trajectory evolution is obtained by means of the resonance model, where the inspiral is derived mostly from 5PN adiabatic fluxes, and the jump is added only when the resonance condition is satisfied.

The comparison is presented in Fig 7.2. We show the differences ΔL_z (left, red) and ΔQ (right, blue) for IC4 crossing two resonances $3:0:-2$ and $3:-4:-2$. The apparent thickness of the lines shown in the figures is due to oscillations on the orbital timescale. In this plot, the evolution of the respective quantities obtained from the RM are overlaid for both the 'step' (black, dashed) and 'smooth' (orange, dashed-dotted) impulse functions that model the jump obtained from the fitting formulae. This figure shows a good agreement of jump size (and therefore resonant phase) and overall evolution between the RM and osculating method regardless of the choice for the impulse function. The difference between the evolutions from the two impulse functions is $\sim \mathcal{O}(10^{-8})$, too small to resolve on the scale in Fig 7.2.

Additionally, we compare the agreement between the RM and osculating methods at the waveform level. The trajectory information from both models is fed into the AAK module, and the snapshot of the waveform (+ polarization) a few hours just before the plunge is displayed in Fig 7.3. We can see a remarkable phase match between the two in the top panel. In the lower panel, we switch off the jump in the RM waveform and compare it with the osculating waveform. As a result of dephasing, there is a clear disagreement in the waveforms. Furthermore, we see that in the present example

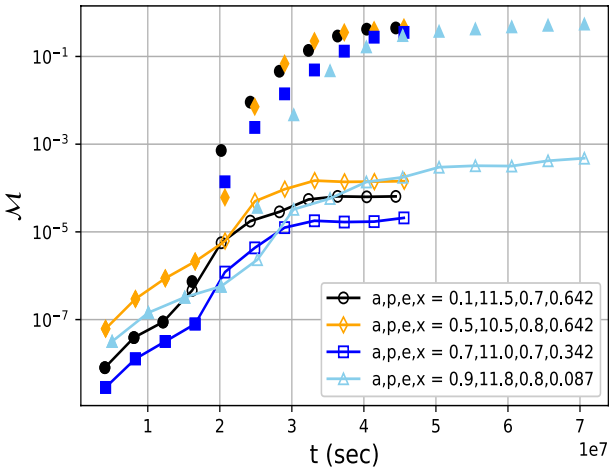

Fig. 7.4 The cumulative mismatch between resonant and non-resonant waveforms using the RM and osculating method. Here, the unfilled markers show the cumulative mismatch between the resonant waveforms using the RM and osculating method for different initial conditions (see Table 7.1) crossing two resonances $n:k:m=3:0:-2$ and $n:k:m=3:-4:-2$ during the evolution. In contrast, the filled markers show the mismatch if resonances are neglected in the waveform model. The filled markers overlay the unfilled ones before crossing the first resonance for every initial condition. The condition with spin 0.9 has the longest inspiral time because the separatrix is close to the central BH compared to the low spin EMRIs.

the merger time corresponding to the end point of the waveform is delayed for the osculating waveform, which takes the tidal jump into account, because of the positive jump in L_z and Q.

In Fig 7.4, the cumulative mismatch between resonant and non-resonant waveforms using the RM and osculating method is shown. The unfilled markers show the cumulative mismatch between the resonant waveforms using the RM and osculating method, for four different initial conditions crossing two resonances $n:k:m=3:0:-2$ and $n:k:m=3:-4:-2$ during the evolution. In contrast, the filled markers show the mismatch when the resonances are neglected in the RM waveform model. Before crossing the first resonance, the filled markers overlay the unfilled ones for every initial condition. This indicates that the mismatch increases with each subsequent resonance encounter. The tiny increase in $\mathcal{M}$ before resonance is only due to numerical error arising from a 'shift' in initial orbital frequencies due to tidally perturbed metric as also discussed in [128] using a Newtonian analysis. A key point to notice is that after the resonance the mismatch between the RM and osculating resonant waveforms grows from $10^{-5}-10^{-7}$ only up to $\sim 10^{-3}$. This result is significant for the waveform

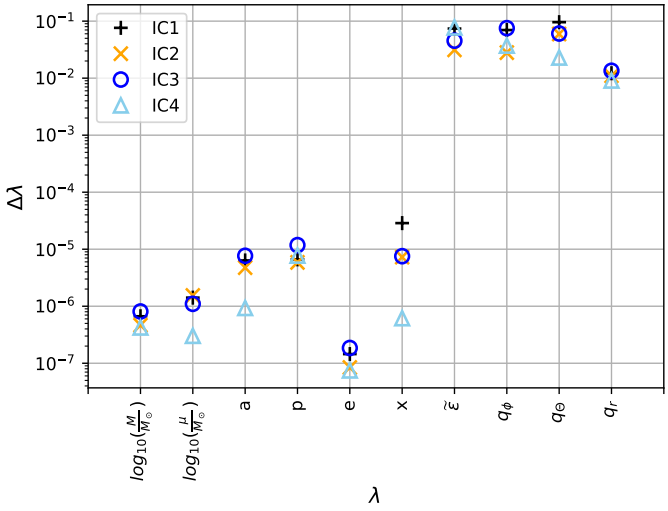

Fig. 7.5 Measurement precision $\Delta\lambda$ of EMRI's intrinsic and tidal parameters for the initial conditions listed in Table 7.1. All the signals are normalized to SNR = 30.

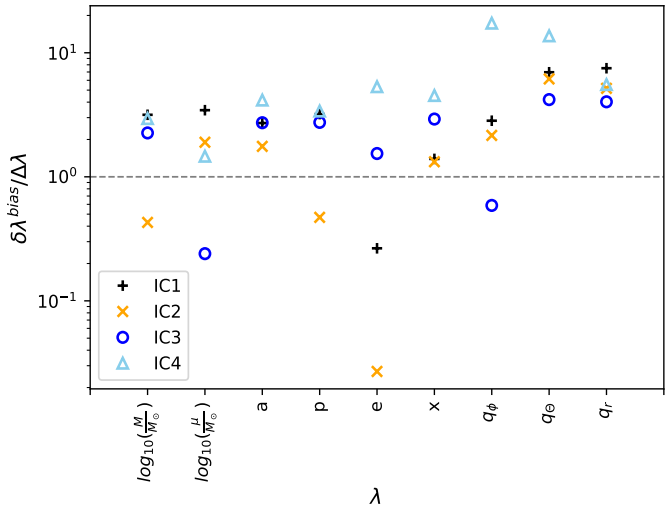

Fig. 7.6 The ratio $\delta\lambda^{bias}/\Delta\lambda$ between the size of the systematic and statistical errors is shown for the initial conditions listed in Table 7.1. The dashed grid line indicates that the ratio is equal to 1. For $\delta\,\lambda^{bias}/\Delta\lambda > 1$, the bias induced by inaccurate waveform modeling is more significant than that caused by the noise fluctuations in the detector.

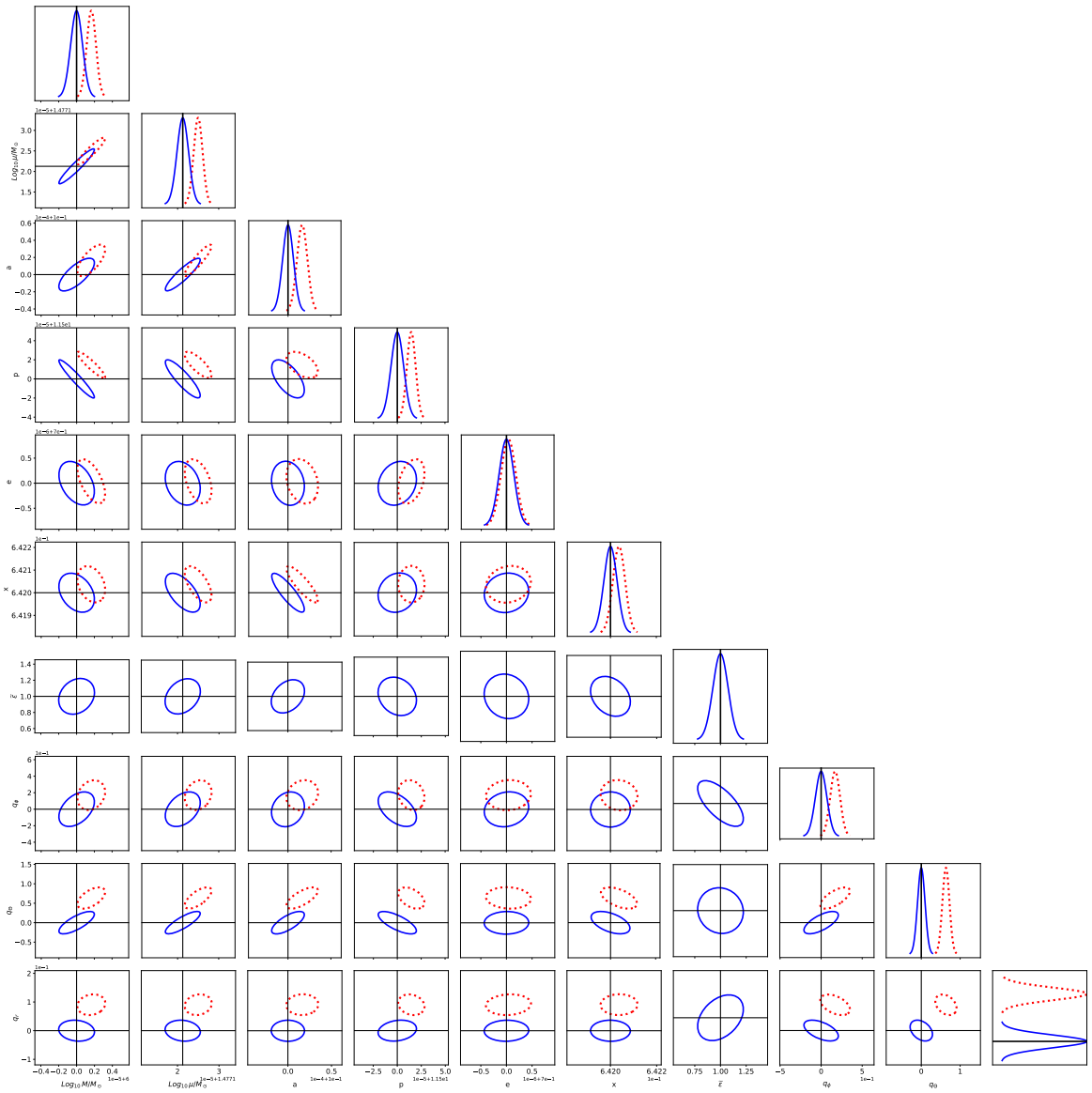

Fig. 7.7 The 2-dimensional posterior showing 3σ contours for IC1 (see Table 7.1), where the injected signal had an SNR of 30. The solid (blue) contours are generated by the model with resonance and are centered on the true parameter values. The dotted (red) contours are derived from a model without resonance with peak shifted to parameter values estimated with induced systematic error.

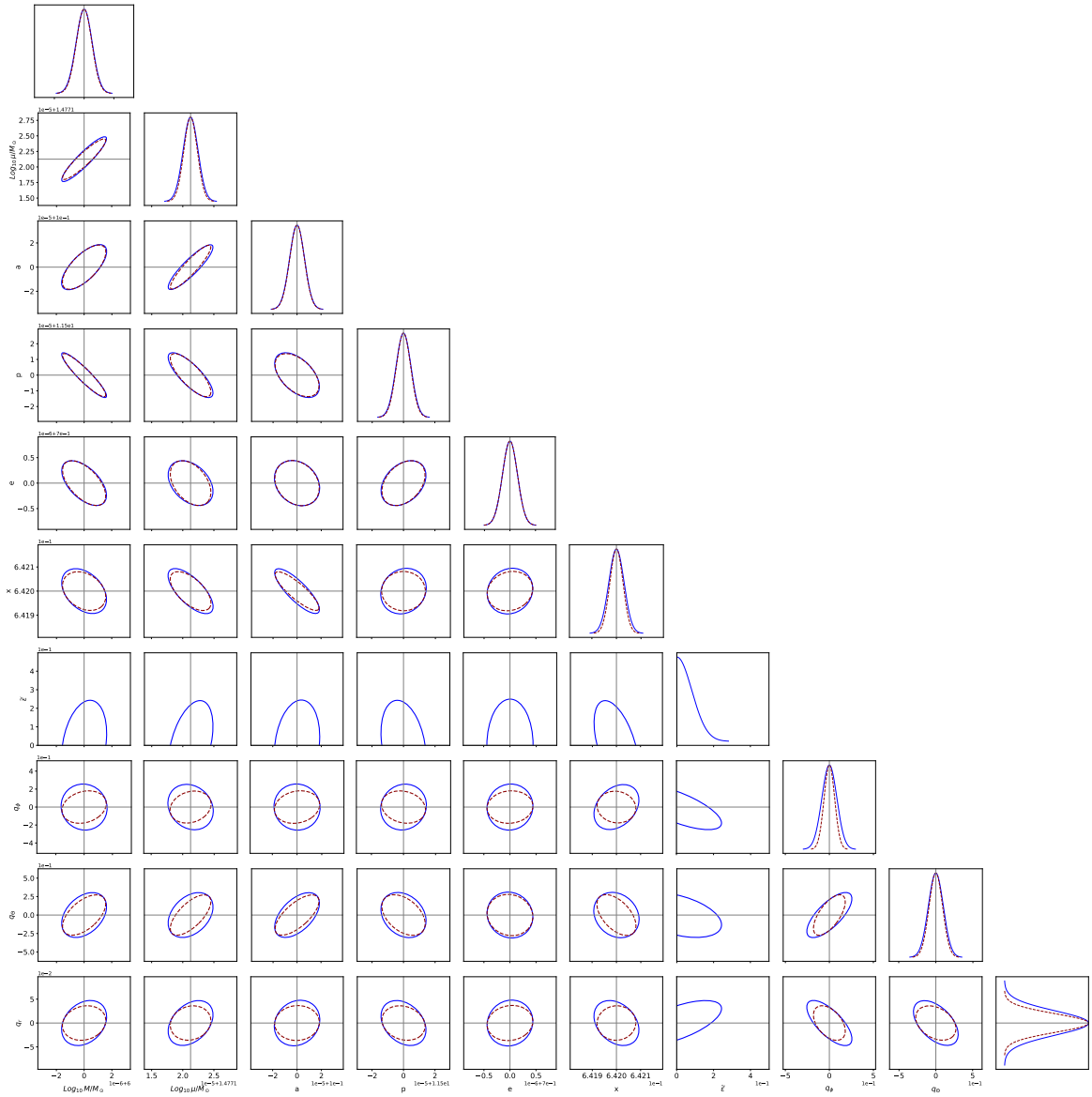

Fig. 7.8 The 2-dimensional posterior showing 3σ contours for IC1 (see Table 7.1), where the injected signal had an SNR of 30. The blue-solid contours represent the model in which the tidal parameter is set to zero ($\widetilde{\epsilon} = 0$), and red-dotted contours represent the model in which the tidal parameter is not included in the analysis. The confidence contours are centered at the true value since both signals were unperturbed.

modeling community, because it quantifies the mismatch induced by ignoring the resonance modeling. As long as we correctly predict the resonance jumps, it is possible to have an accurate waveform up to a mismatch of $\sim 10^{-3}$. In summary, we can model (multiple) tidal resonances by using the RM and match the waveform until the end of the inspiral keeping $\mathcal{M}$ below 10^{-3}. It is worth reminding the reader that the cause of the mismatch of $\mathcal{O}(10^{-3})$ comes from a numerical error resulting from tidally perturbed metric causing a tiny 'shift' in the initial conditions. If we can determine the initial conditions correctly, the mismatch would be smaller. We also find no discernible difference in mismatch between the RM with the 'step' and the 'smooth' impulse functions for all four initial conditions.

7.4.2 Parameter estimation and systematic bias

With the resonant waveforms derived from the RM and including only one resonance $(3:0:-2)$, we examine the parameter measurement precision of the orbital and tidal parameters based on Fisher matrices (discussed in Sec 7.3.1). All the waveforms have been normalized so that their SNR = 30 and the extrinsic parameters are set to $\{\theta_K, \phi_K, \theta_S, \phi_S\} = \{\pi/4, 0, \pi/4, 0\}$. The results for Fisher matrix estimates are shown in Fig. 7.5. In this figure, we can see that the orbital parameters (except the initial phases) are well constrained, whereas the tidal parameters are less well constrained. In particular, the measurement precision for the tidal parameter $\tilde{\epsilon}$ and the phases is $\sim 10^{-1}$. In terms of the waveform, the initial phases determine the initial position of the compact object and do not affect the frequency evolution of the EMRI at adiabatic order, so their impact is weaker, which leads to the lower measurement precision. Due to the longer observation time for IC4 (see Fig. 7.4), the orbital parameters of this system are better constrained than for the other models.

In waveform modeling, using an approximate model can introduce systematic error (7.11) into parameter estimation. We investigate the systematic error by using a non-resonant approximate waveform h_m, while the true waveform h_t incorporates the resonance using the RM. To compare this error with the statistical error (7.10), we show the ratio $\delta\lambda^{bias}/\Delta\lambda$ in Fig. 7.6. With $\delta\lambda^{bias}/\Delta\lambda > 1$, the inaccurate waveform modeling leads to biases larger than those induced by noise fluctuations. The magnitude of systematic bias naturally depends on the magnitude of the tidal perturbation. For the strong but still realistic examples (motivated by [97, 38, 6]) of tidal resonance that we consider, the systematic errors cannot be completely ignored. Thus, we may need to account for the presence of tidal perturbers when performing careful inference, as also indicated by mismatch analysis in Fig. 7.4.

In addition to measurement precision, the Fisher matrix also provides the covariance relation between the parameters. Covariance is a measure of how much two variables vary together. To visualize this, we plot the 3σ contours in Fig. 7.7 for IC1. The solid (blue) contours are generated by the true model (with resonance) and are centered on the true parameter values. The dotted (red) contours are derived from the model without resonance, where the peak values are shifted by the amount of the systematic errors shown in Fig. 7.6. For the example considered in Fig. 7.7, the bias is within the credible region for most of the EMRI parameters. However, our ability to measure the initial phases is more significantly affected if tidal effect is not modeled. The normalized tidal parameter $\widetilde{\epsilon}$ (discussed below Eq. 7.12) can be constrained with an absolute precision of 0.25.

In the analysis above, we showed the bias induced in parameter measurement precision if tidal resonance was not modeled in the waveform. Next, we compare the same model with the one in which tidal parameter is set to zero *i.e.* the signal is not tidally perturbed but the tidal parameter is included in the Fisher analysis. The goal is to check whether the error estimates are affected by the introduction of the tidal parameter. We assume that the signal is given by a model with the tidal parameter set to zero. In Fig. 7.8 blue-solid contours show the 3σ confidence region when we use the model with 10 parameters including the tidal parameter, while the red-dotted contours corresponding to the model with 9 parameters excluding the tidal parameter.

Because the tidal parameter is positive by definition, we show a section of ellipses in the positive range. The orbital parameters such as $M, \mu, a, p, e, \mathrm{x}$ are measured with approximately the same precision in both models. Our ability to measure the EMRI's initial phasing is noticeably more degraded, but the overall impact is still fairly marginal. Thus, the tidal parameter is largely a non-degenerate degree of freedom, and its inclusion in EMRI data analysis will not pose fundamental issues in the absence of a tidal perturber at least for the magnitude of tidal perturbation considered in our work.

By combining the results from Fig. 7.7 and Fig. 7.8 for the example considered, we can infer the maximum value of tidal parameter under which the presence of a tidal resonance cannot be assessed. According to Fig. 7.7, we can constrain the tidal parameter within the error bar of ± 0.25 of the true value, whereas Fig. 7.8 says that we can rule out values larger than 0.25 for $\widetilde{\epsilon}$. Therefore, if we choose a signal with $\widetilde{\epsilon} = 0.25$, we would likely have an ellipse centered at 0.25 and the width touching the zero (since the error bar is ± 0.25). It follows that we may rule out zero for a larger $\widetilde{\epsilon}$ (> 0.25), thereby marking the presence of the perturber, but not for a smaller $\widetilde{\epsilon}$.

Chapter 8

Conclusion

It is only the start of an exciting succession of events that have unfolded in the field since the first direct detection of GWs by Advanced LIGO in 2015. In just a short period, we have witnessed numerous binary mergers, while the outlook for a forthcoming detection with pulsar timing arrays has greatly improved. In this fast-evolving field of GW astronomy, it is hoped that the work presented here contributes modestly but timely to the growing field.

While the background theory of GWs and the framework needed for our work is explained in Chapters 1 to 5, our main results are presented in Chapter 6 and Chapter 7. In Chapter 6, we show that in the presence of a tidal perturber, an EMRI can encounter multiple resonances before the plunge. Each resonance may last for hundreds or thousands of orbital cycles depending on the EMRI's mass ratio. We assessed the impact of tidal resonances on GWs to survey the orbital parameter space and investigate how often tidal resonances occur in realistic inspirals. The effect of resonances (self-force and tidal) on phase evolution contributes more than post-adiabatic corrections. In order to understand the impact of tidal resonances on waveforms, we calculated accumulation in phase following an encounter with a tidal resonance by an EMRI. The study of dephasing revealed that a large portion of orbital space is impacted by the tidal resonance, while the less eccentric ($\lesssim 0.2$) inspirals do not leave a detectable imprint in the phase evolution. We also provide fitting formulae for the change in the constants of motion caused by low-order tidal resonances, which can be efficiently used to take into account the resonance jump in waveform modeling without much computational cost.

In Chapter 7, using Fisher matrices, we analyzed how this phenomenon impacts the estimation of the intrinsic orbital and tidal parameters by using a resonance model (RM) based on a step function approach. We validated the evolution of the trajectory

derived from the RM by comparing it with the forced osculating trajectory. This gives us confidence in the robustness of the fitting formulae as well as the implementation of the RM. Our study examined the systematic errors that might arise from neglecting tidal resonances in the estimation of intrinsic parameters. Our results suggest that parameter estimates are likely to be biased if resonances are not considered in waveform modeling. In addition to tidal resonances, transient self-force resonances could also be modeled using the analysis presented in our work.

As part of the extension of this work, we will relax the stationary perturber approximation and explore multiple resonant interactions in parameter estimation using Bayesian posterior calculations. Furthermore, once the resonances jump sizes due to the self-force is available, the ability of RM to detect and characterize EMRIs should be investigated. Last, the overall approach in this work, and modeling efforts by the EMRI community is to pursue a *modeled* treatment of resonances (be it self-force or tidal) in data analysis. However, this is not the only possible approach, since phenomenological treatments such as ERM (where information on resonance jumps is recovered rather than modeled) might also prove useful; this is especially the case if sufficiently precise modeling of these jumps turns out to be unfeasible or unachievable. Thus, it is worthwhile to continue exploring both approaches in parallel, which will in turn benefit from shared techniques such as those introduced in this thesis.

Appendix A

A.1 Fitting formulae for $n : k : m = 3 : 0 : -2$

$$\left\langle \frac{dL_z}{dt} \right\rangle = \frac{e^2}{(e-1)^2}\Bigg(13.8664(a^2(e^5(x^4 + 1.70942x^3 - 0.8785x^2 - 0.5336x - 0.32076) - 4.79651x^3 + 1.781x^2 + 2.27585x + 1.11764) + e^3(7.17415x^4 + 5.67992x^3 - 1.22333x^2 - 4.01184x - 1.64238) + e^2(-7.25395x^4 - 3.92149x^3 - 0.0528632x^2 + 3.96175x + 1.36426) + e(4.21764x^4 + 1.69592x^3 + 0.404326x^2 - 2.33394x - 0.756895) + 0.012012x^4 - 0.012569x^3 + 0.0127552x^2 - 0.00766985x - 0.000627702) + a(e^5(0.289607x^4 - 3.94961x^3 - 3.9027x^2 - 1.82132x + 0.710913) + e^4(-0.370237x^4 + 12.6334x^3 + 15.3809x^2 + 6.2625x - 2.47674) + e^3(-0.377266x^4 - 17.4934x^3 - 25.9795x^2 - 9.31769x + 3.78052) + e^2(1.09716x^4 + 14.3769x^3 + 25.2598x^2 + 7.96198x - 3.5384) + e(-0.864082x^4 - 7.40462x^3 - 14.5161x^2 - 4.3349x + 1.92547) - 0.0109531x^4 + 0.0114339x^3 - 0.0375848x^2 - 0.00156484x + 0.00169788) + e^5(-0.328544x^4 + 0.766588x^3 + 1.98025x^2 + 5.37844x + 2.57726) + e^4(0.850133x^4 - 2.02349x^3 - 7.73277x^2 - 19.233x - 9.3297) + e^3(-0.8120x^4 + 2.0503x^3 + 13.0406x^2 + 29.8651x + 14.6449) + e^2(0.320494x^4 - 0.886721x^3 - 12.336x^2 - 26.4222x - 13.0807) + e(-0.0228461x^4 + 0.142487x^3 + 7.20898x^2 + 14.7695x + 7.35985) + 0.00829816x^4 - 0.0186416x^3 + 0.0256575x^2 + 0.0190106x + 0.0117907)\Bigg)\sin(-2q_{\phi 0} + 3q_{r0})\,, \quad \text{(A.1)}$$

$$\left\langle \frac{dQ}{dt} \right\rangle = \frac{e^2}{(e-1)^2}\Bigg(6166.4(a^2(e^5(x^6-3.36x^5+4.29x^4-2.64672x^3+0.827x^2-0.113x) + e^4(-2.561x^6+8.6411x^5-10.9856x^4+6.73865x^3-2.14181x^2 + 0.2942x+0.01469)+e^3(2.4592x^6-8.338x^5+10.4957x^4-6.38662x^3 + 2.10369x^2-0.307742x-0.02541)+e^2(-1.0576x^6+3.73285x^5-4.57117x^4 + 2.7179x^3-0.98419x^2+0.16744x+0.023683)+e(0.2142x^6-0.77253x^5 + 0.858453x^4-0.46584x^3+0.23502x^2-0.054646x-0.0146077) - 0.0131998x^6+0.0442585x^5-0.057625x^4+0.0360626x^3-0.01073x^2 + 0.0130161x-0.00683955)+a(e^5(-1.41091x^6+4.70494x^5-5.988x^4 + 3.7815x^3-1.17999x^2+0.082132x+0.01024)+e^4(3.636x^6-12.12x^5 + 15.3555x^4-9.7812x^3+3.11081x^2-0.16016x-0.03945)+e^3(-3.51x^6 + 11.7153x^5-14.6986x^4+9.5462x^3-3.1598x^2+0.048679x+0.06504) + e^2(1.56518x^6-5.20606x^5+6.36726x^4-4.35903x^3+1.5984x^2 + 0.10196x-0.06398)+e(-0.31407x^6+1.02894x^5-1.14294x^4+0.9495x^3 - 0.45183x^2-0.10985x+0.03645)+0.02657x^6-0.066807x^5+0.0859032x^4 - 0.0523576x^3+0.0151582x^2-0.00205405x+0.0944331)+e^5(0.50946x^6 - 1.6744x^5+2.1131x^4-1.3159x^3+0.3583x^2+0.00554x+0.04718) + e^4(-1.32659x^6+4.35489x^5-5.48625x^4+3.45939x^3-0.77303x^2 - 0.060315x-0.168315)+e^3(1.3068x^6-4.2645x^5+5.36471x^4-3.47472x^3+ 0.6569x^2+0.15588x+0.26122)+e^2(-0.58987x^6+1.944x^5-2.42323x^4 + 1.67565x^3-0.186175x^2-0.1797x-0.22711)+e(0.12024x^6-0.39217x^5 + 0.49435x^4-0.42018x^3-0.0448911x^2+0.118569x+0.12802)-0.00827x^6 + 0.02662x^5-0.03651x^4+0.0195x^3-0.05746x^2+0.000836659x + 0.000193748)\Bigg)\sin(-2q_{\phi 0}+3q_{r0})\,, \quad \text{(A.2)}$$

A.2 Suppression of odd $k+m$ integer resonances

A.2.1 Qualitative discussion for $m = \pm 1$ resonances

We discover that tidal resonances with odd $k+m$ integer do not give rise to a jump in the constants of motion. Hence, they do not contribute to a secular accumulation of a phase shift and are therefore not relevant for waveform modeling. On assuming a static tidal interaction, the leading order external potential at a large distance is expressed as

$$U_{ext} \propto \mathcal{E}_{ab}\, x^a x^b,$$

where the symmetric tidal tensor $\mathcal{E}_{ab}$ contains all the information about the tidal environment. For $m = \pm 1$ modes, only $\mathcal{E}_{xz}$ and $\mathcal{E}_{yz}$ contribute where $x, y, z(r, \theta, \phi)$ are standard Cartesian (spherical) coordinates. Note that transforming $q_\phi \to q_{\phi+\pi} \Rightarrow x \to -x, y \to -y$ or $q_\theta \to q_{\theta+\pi} \Rightarrow z \to -z$ leads to a sign flip of the tidal potential and hence the resulting torque. Therefore, if corresponding points (for instance, both (q_ϕ, q_θ) and $(q_\phi, q_{\theta+\pi})$) are passed by an orbit, then it results in a net cancellation of dL_z/dt between the two segments of the orbit. In Fig A.1, for illustrative purpose, we show a section of the orbit in the q_ϕ - q_θ plane for $k+m = 1$ (left) and $k+m = 2$ (right) resonance combinations. In the left plot, for fixed $q_r = 0$, the distance between two lines is π. Thus, the orbit evolves in such a manner, that the net tidal force cancels out resulting in no change in L_z. Whereas, in the right plot, the corresponding "cancellation" points are not crossed by the orbit. While this discussion helps understand the vanishing dL_z/dt on crossing odd $k+m$ resonances, empirically we found that dQ/dt also vanishes for such resonances.

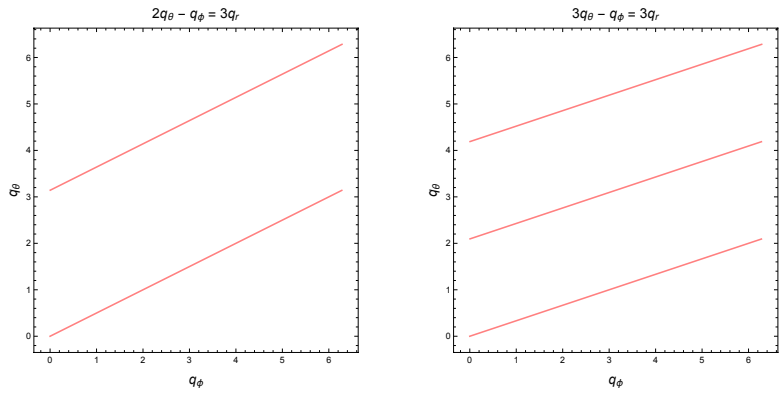

Fig. A.1 Section of orbit in q_ϕ - q_θ plane for different resonance conditions.

A.2.2 Qualitative discussion for $m = \pm 2$ resonances

In Fig. A.2, for illustrative purpose, we show section of orbit in q_r - q_θ plane for different resonances (with $m = \pm 2$). In the leftmost panel we consider a $2:1:-2$ resonance (odd k) and compare section for fixed values of $q_\phi = 0$ (red lines) and $q_\phi = \pi/2$ (blue-dashed lines). On rotation of the orbit by $\pi/2$, the plot shows the same value for q_r and q_θ. Thus, the net tidal force of $m = \pm 2$ modes acting on the orbit cancels out completely resulting in no change in L_z. Hence, they do not contribute to a secular accumulation of a phase shift and are therefore not relevant for waveform modeling. The middle plot shows a $k = 2$ resonance. In this case, two lines are not identical: therefore, the tidal force couples with the quadrupole moment of the orbit causing a finite jump in L_z. The rightmost plot shows the $-2:3:-2$ resonance exhibiting the same behavior as the $k = 1$ case.

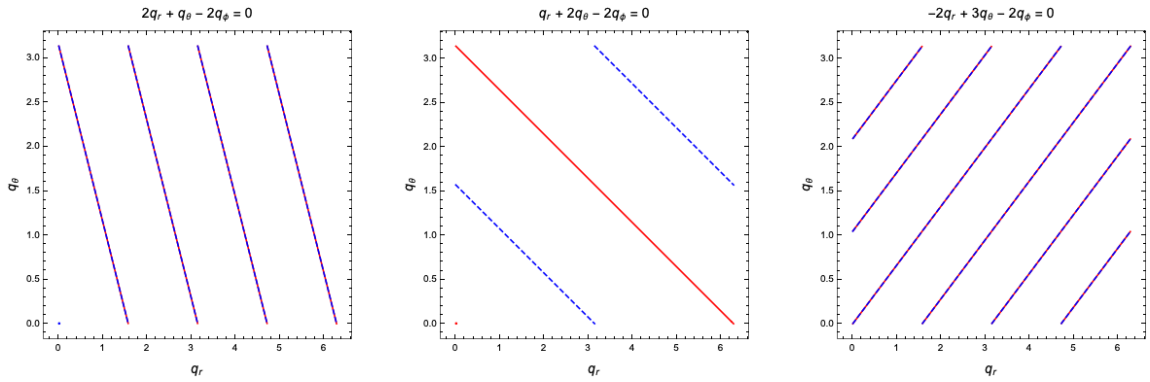

Fig. A.2 Section of orbit in q_r - q_θ plane for different resonance conditions. The red lines and blue dashed lines are obtained for $q_\phi = 0$ and $q_\phi = \pi/2$, respectively.

References

[1] LIGO Scientific Collaboration and Virgo Collaboration. Observation of gravitational waves from a binary black hole merger. *Phys. Rev. Lett.*, 116:061102, Feb 2016.

[2] The Ligo Scientific Collaboration and the Virgo Collaboration. Population properties of compact objects from the second LIGO–virgo gravitational-wave transient catalog. *The Astrophysical Journal Letters*, 913(1):L7, May 2021.

[3] Pau Amaro-Seoane et al. eLISA: Astrophysics and cosmology in the millihertz regime. arXiv-1201.3621, 2012.

[4] S. Kawamura et al. The Japanese space gravitational wave antenna DECIGO. *Class. Quant. Grav.*, 23:S125–S132, 2006.

[5] Jun Luo et al. TianQin: a space-borne gravitational wave detector. *Classical and Quantum Gravity*, 33(3):035010, Jan 2016.

[6] Béatrice Bonga, Huan Yang, and Scott A. Hughes. Tidal resonance in extreme mass-ratio inspirals. *Phys. Rev. Lett.*, 123(10):101103, 2019.

[7] Cosimo Bambi. *Classical Tests of General Relativity*, pages 163–178. Springer, 2018.

[8] Albert Einstein. *Relativity: the Special and the General Theory.* Routledge classics. Fifteenth edition, 2001.

[9] Sean M. Carroll. Lecture notes on general relativity, 1997.

[10] S. Chandrasekhar. *The Mathematical Theory of Black Holes*, pages 5–26. Springer, 1984.

[11] *Bending of Light in the 1919 Eclipse Experiments: Einstein and Eddington*, pages 127–137. Springer, 2009.

[12] N. S. Hetherington. Sirius B and the gravitational redshift - an historical review. *Quarterly Journal of the Royal Astronomical Society*, 21:246–252, September 1980.

[13] Kazunori Akiyama et al. First M87 Event Horizon Telescope Results. V. Physical Origin of the Asymmetric Ring. *Astrophys. J. Lett.*, 875(1):L5, 2019.

[14] Dimitrios Psaltis. Testing general relativity with the event horizon telescope. *General Relativity and Gravitation*, 51(10), Oct 2019.

[15] Thibault Damour. Poincaré, the dynamics of the electron, and relativity. *Comptes Rendus Physique*, 18(9):551–562, 2017.

[16] R. A. Hulse and J. H. Taylor. Discovery of a pulsar in a binary system. *Apj letters*, 195:L51–L53, January 1975.

[17] J. M. Weisberg, D. J. Nice, and J. H. Taylor. Timing Measurements of the Relativistic Binary Pulsar PSR B1913+16. *Apj*, 722(2):1030–1034, October 2010.

[18] LIGO Scientific Collaboration and Virgo Collaboration. GW170817: Observation of Gravitational Waves from a Binary Neutron Star Inspiral. *Phys. Rev. Lett.*, 119:161101, Oct 2017.

[19] M. Nicholl et al. The Electromagnetic Counterpart of the Binary Neutron Star Merger LIGO/Virgo GW170817. III. Optical and UV Spectra of a Blue Kilonova from Fast Polar Ejecta. *The Astrophysical Journal*, 848(2):L18, oct 2017.

[20] Alexander H. Nitz et al. 3-OGC: Catalog of gravitational waves from compact-binary mergers. *The Astrophysical Journal*, 922(1):76, nov 2021.

[21] Michele Maggiore. *Gravitational waves*. Oxford Univ. Press, Oxford, 2008.

[22] LIGO Scientific and Virgo Collaborations. Tests of General Relativity with GW150914. *Phys. Rev. Lett.*, 116:221101, May 2016.

[23] Pau Amaro-Seoane. The gravitational capture of compact objects by massive black holes, 2020.

[24] Pau Amaro-Seoane. Extremely large mass-ratio inspirals. *Phys. Rev. D*, 99:123025, Jun 2019.

[25] Prospects for fundamental physics with LISA. *General Relativity and Gravitation*, 52(8), 2020.

[26] G. B. Hobbs and others. Gravitational-wave detection using pulsars: Status of the parkes pulsar timing array project. *Publications of the Astronomical Society of Australia*, 26(2):103–109, 2009.

[27] P. C. Peters and J. Mathews. Gravitational radiation from point masses in a keplerian orbit. *Phys. Rev.*, 131:435–440, Jul 1963.

[28] Edwin Hubble. A Relation between Distance and Radial Velocity among Extra-Galactic Nebulae. *Proceedings of the National Academy of Science*, 15(3):168–173, March 1929.

[29] R W Wilson. History of the discovery of the cosmic microwave background radiation. *Physica Scripta*, 21(5):599–605, jan 1980.

[30] C. L. Bennett et al. First-year wilkinson microwave anisotropy probe (WMAP) observations: Preliminary maps and basic results. *The Astrophysical Journal Supplement Series*, 148(1):1–27, sep 2003.

[31] Planck collaboration. Planck results VI. Cosmological parameters. *Astronomy & Astrophysics*, 641:A6, 2020.

[32] Gerard Auger and Eric Plagnol. *An Overview of Gravitational Waves: Theory, Sources and Detection*. World Scientific, Singapore, 2017.

[33] R. N. Manchester. Pulsar glitches and their impact on neutron-star astrophysics. *IAU Symp.*, 337:197–202, 2017.

[34] Angelo Ricciardone. Primordial gravitational waves with LISA. *Journal of Physics: Conference Series*, 840:012030, May 2017.

[35] Alvin J. K. Chua, Michael L. Katz, Niels Warburton, and Scott A. Hughes. Rapid generation of fully relativistic extreme-mass-ratio-inspiral waveform templates for lisa data analysis. *Phys. Rev. Lett.*, 126:051102, Feb 2021.

[36] E. A. Huerta and Zhizhen Zhao. Advances in machine and deep learning for modeling and real-time detection of multi-messenger sources. In *Handbook of Gravitational Wave Astronomy*, pages 1–27. Springer, 2021.

[37] Razieh Emami and Abraham Loeb. Observational signatures of the black hole mass distribution in the galactic center. *Journal of Cosmology and Astroparticle Physics*, 2020(02):021–021, Feb 2020.

[38] Razieh Emami and Abraham Loeb. Detectability of gravitational waves from a population of inspiralling black holes in Milky Way-mass galaxies. *Monthly Notices of the Royal Astronomical Society*, 502(3):3932–3941, 02 2021.

[39] Zhen Pan and Huan Yang. Formation rate of extreme mass ratio inspirals in active galactic nuclei. *Phys. Rev. D*, 103:103018, May 2021.

[40] Zhen Pan, Zhenwei Lyu, and Huan Yang. Wet extreme mass ratio inspirals may be more common for spaceborne gravitational wave detection. *Phys. Rev. D*, 104:063007, Sep 2021.

[41] Bence Kocsis, Nicolás Yunes, and Abraham Loeb. Observable signatures of extreme mass-ratio inspiral black hole binaries embedded in thin accretion disks. *Physical Review D*, 84(2), Jul 2011.

[42] Audrey Galametz et al. The cosmic evolution of active galactic nuclei in galaxy clusters. *The Astrophysical Journal*, 694(2):1309–1316, Mar 2009.

[43] Michael Macuga and et al. The fraction of active galactic nuclei in the uss 1558–003 protocluster at z = 2.53. *The Astrophysical Journal*, 874(1):54, Mar 2019.

[44] Jonathan R Gair, Stanislav Babak, Alberto Sesana, Pau Amaro-Seoane, Enrico Barausse, Christopher P L Berry, Emanuele Berti, and Carlos Sopuerta. Prospects for observing extreme-mass-ratio inspirals with LISA. *Journal of Physics: Conference Series*, 840:012021, may 2017.

[45] Christopher P. L. Berry, Scott A. Hughes, Carlos F. Sopuerta, Alvin J. K. Chua, Anna Heffernan, Kelly Holley-Bockelmann, Deyan P. Mihaylov, M. Coleman Miller, and Alberto Sesana. The unique potential of extreme mass-ratio inspirals for gravitational-wave astronomy. *arXiv-1903.03686*, 2019.

[46] Abhay Ashtekar. The simplicity of black holes. *Physics*, 8, 2015.

[47] Leor Barack and Curt Cutler. Using LISA extreme-mass-ratio inspiral sources to test off-kerr deviations in the geometry of massive black holes. *Physical Review D*, 75(4), 2007.

[48] James M. Bardeen, William H. Press, and Saul A. Teukolsky. Rotating Black Holes: Locally Nonrotating Frames, Energy Extraction, and Scalar Synchrotron Radiation. *Apj*, 178:347–370, December 1972.

[49] W Schmidt. Celestial mechanics in kerr spacetime. *Classical and Quantum Gravity*, 19(10):2743–2764, Apr 2002.

[50] Yasushi Mino. Perturbative approach to an orbital evolution around a supermassive black hole. *Physical Review D*, 67(8), Apr 2003.

[51] Ryuichi Fujita and Wataru Hikida. Analytical solutions of bound timelike geodesic orbits in kerr spacetime. *Classical and Quantum Gravity*, 26(13):135002, June 2009.

[52] Yasushi Mino, Misao Sasaki, and Takahiro Tanaka. Gravitational radiation reaction to a particle motion. *Physical Review D*, 55(6):3457–3476, Mar 1997.

[53] Theodore C. Quinn and Robert M. Wald. Axiomatic approach to electromagnetic and gravitational radiation reaction of particles in curved spacetime. *Physical Review D*, 56(6):3381–3394, Sep 1997.

[54] Eric Poisson, Adam Pound, and Ian Vega. The motion of point particles in curved spacetime. *Living Reviews in Relativity*, 14(1), Sep 2011.

[55] Leor Barack and Adam Pound. Self-force and radiation reaction in general relativity. *Reports on Progress in Physics*, 82(1):016904, Nov 2018.

[56] C. W. Misner, K. S. Thorne, and J. A. Wheeler. Gravitation. *The Astrophysical Journal*, 2017.

[57] Adam Pound, Barry Wardell, Niels Warburton, and Jeremy Miller. Second-order self-force calculation of gravitational binding energy in compact binaries. *Physical Review Letters*, 124(2), Jan 2020.

[58] Samuel D. Upton and Adam Pound. Second-order gravitational self-force in a highly regular gauge. *Phys. Rev. D*, 103:124016, June 2021.

[59] R. Fujita. Gravitational waves from a particle in circular orbits around a schwarzschild black hole to the 22nd post-newtonian order. *Progress of Theoretical Physics*, 128(5):971–992, nov 2012.

[60] R. Fujita. Gravitational waves from a particle in circular orbits around a rotating black hole to the 11th post-newtonian order. *Progress of Theoretical and Experimental Physics*, 2015(3):33E01–0, 2015.

[61] Ryuichi Fujita and Masaru Shibata. Extreme mass ratio inspirals on the equatorial plane in the adiabatic order. *Physical Review D*, 102(6), sep 2020.

[62] Leor Barack and Curt Cutler. LISA capture sources: Approximate waveforms, signal-to-noise ratios, and parameter estimation accuracy. *Physical Review D*, 69(8), apr 2004.

[63] Stanislav Babak, Hua Fang, Jonathan R. Gair, Kostas Glampedakis, and Scott A. Hughes. 'Kludge' gravitational waveforms for a test-body orbiting a Kerr black hole. *Phys. Rev. D*, 75:024005, 2007.

[64] E. A. Huerta and Jonathan R. Gair. Influence of conservative corrections on parameter estimation for extreme-mass-ratio inspirals. *Phys. Rev. D*, 79:084021, 2009.

[65] E. A. Huerta, Prayush Kumar, Jonathan R. Gair, and Sean T. McWilliams. Self-forced evolutions of an implicit rotating source: A natural framework to model comparable and intermediate mass-ratio systems from inspiral through ringdown. *Phys. Rev. D*, 90(2):024024, 2014.

[66] Alvin J. K. Chua and Jonathan R. Gair. Improved analytic extreme-mass-ratio inspiral model for scoping out eLISA data analysis. *Class. Quant. Grav.*, 32:232002, 2015.

[67] Alvin J. K. Chua, Christopher J. Moore, and Jonathan R. Gair. Augmented kludge waveforms for detecting extreme-mass-ratio inspirals. *Phys. Rev. D*, 96(4):044005, 2017.

[68] Georgios Lukes-Gerakopoulos, George Contopoulos, and Theocharis A. Apostolatos. Non-linear effects in non-kerr spacetimes. In *Springer Proceedings in Physics*, pages 129–136. Springer International Publishing, 2014.

[69] Georgios Lukes-Gerakopoulos, Theocharis A. Apostolatos, and George Contopoulos. Observable signature of a background deviating from the Kerr metric. *Phys. Rev. D*, 81:124005, 2010.

[70] Jonathan R. Gair, Chao Li, and Ilya Mandel. Observable Properties of Orbits in Exact Bumpy Spacetimes. *Phys. Rev. D*, 77:024035, 2008.

[71] Kyriakos Destounis, Arthur G. Suvorov, and Kostas D. Kokkotas. Gravitational wave glitches in chaotic extreme-mass-ratio inspirals. *Physical Review Letters*, 126(14), apr 2021.

[72] Maarten van de Meent. Conditions for Sustained Orbital Resonances in Extreme Mass Ratio Inspirals. *Phys. Rev. D*, 89(8):084033, 2014.

[73] Éanna É. Flanagan and Tanja Hinderer. Transient resonances in the inspirals of point particles into black holes. *Phys. Rev. Lett.*, 109:071102, Aug 2012.

[74] Éanna E. Flanagan, Scott A. Hughes, and Uchupol Ruangsri. Resonantly enhanced and diminished strong-field gravitational-wave fluxes. *Phys. Rev. D*, 89(8):084028, 2014.

[75] Tanja Hinderer and Éanna É. Flanagan. Two-timescale analysis of extreme mass ratio inspirals in kerr spacetime: Orbital motion. *Phys. Rev. D*, 78:064028, Sep 2008.

[76] Scott A. Hughes, Niels Warburton, Gaurav Khanna, Alvin J. K. Chua, and Michael L. Katz. Adiabatic waveforms for extreme mass-ratio inspirals via multivoice decomposition in time and frequency. *Phys. Rev. D*, 103:104014, May 2021.

[77] Alvin J. K. Chua, Michael L. Katz, Niels Warburton, and Scott A. Hughes. Rapid generation of fully relativistic extreme-mass-ratio-inspiral waveform templates for lisa data analysis. *Phys. Rev. Lett.*, 126:051102, Feb 2021.

[78] Uchupol Ruangsri and Scott A. Hughes. Census of transient orbital resonances encountered during binary inspiral. *Phys. Rev. D*, 89:084036, Apr 2014.

[79] Christopher P. L. Berry, Robert H. Cole, Priscilla Cañizares, and Jonathan R. Gair. Importance of transient resonances in extreme-mass-ratio inspirals. *Phys. Rev. D*, 94:124042, Dec 2016.

[80] Jeandrew Brink, Marisa Geyer, and Tanja Hinderer. Orbital resonances around black holes. *Phys. Rev. Lett.*, 114:081102, Feb 2015.

[81] Lorenzo Speri and Jonathan R. Gair. Assessing the impact of transient orbital resonances. *Phys. Rev. D*, 103:124032, Jun 2021.

[82] Maarten van de Meent. Resonantly enhanced kicks from equatorial small mass-ratio inspirals. *Phys. Rev. D*, 90(4):044027, 2014.

[83] Nicolas Yunes and Jose Gonzalez. Metric of a tidally perturbed spinning black hole. 73:024010, 2006.

[84] Paul L. Chrzanowski. Vector potential and metric perturbations of a rotating black hole. *Phys. Rev. D*, 11:2042–2062, Apr 1975.

[85] Eric Poisson. Tidal deformation of a slowly rotating black hole. *Physical Review D*, 91(4):044004, 2015.

[86] Saul A. Teukolsky. Perturbations of a rotating black hole. I. Fundamental equations for gravitational electromagnetic and neutrino field perturbations. *Astrophys. J.*, 185:635–647, 1973.

[87] Saul A Teukolsky. The kerr metric. *Classical and Quantum Gravity*, 32(12):124006, Jun 2015.

[88] Robert M. Wald. Construction of solutions of gravitational, electromagnetic, or other perturbation equations from solutions of decoupled equations. *Phys. Rev. Lett.*, 41:203–206, Jul 1978.

[89] Lawrence S. Kegeles and Jeffrey M. Cohen. Constructive procedure for perturbations of spacetimes. *Phys. Rev. D*, 19:1641–1664, Mar 1979.

[90] Manuela Campanelli and Carlos O. Lousto. Second order gauge invariant gravitational perturbations of a kerr black hole. *Physical Review D*, 59(12), may 1999.

[91] Huan Yang and Marc Casals. General relativistic dynamics of an extreme mass-ratio binary interacting with an external body. *Phys. Rev. D*, 96:083015, Oct 2017.

[92] Lorenz Zwick, Pedro R Capelo, Elisa Bortolas, Verónica Vázquez-Aceves, Lucio Mayer, and Pau Amaro-Seoane. Improved gravitational radiation time-scales II: Spin–orbit contributions and environmental perturbations. *Monthly Notices of the Royal Astronomical Society*, 506(1):1007–1018, 06 2021.

[93] Kazunari Eda, Yousuke Itoh, Sachiko Kuroyanagi, and Joseph Silk. New probe of dark-matter properties: Gravitational waves from an intermediate-mass black hole embedded in a dark-matter minispike. *Physical Review Letters*, 110(22), May 2013.

[94] Kazunari Eda, Yousuke Itoh, Sachiko Kuroyanagi, and Joseph Silk. Gravitational waves as a probe of dark matter minispikes. *Physical Review D*, 91(4), Feb 2015.

[95] Bradley J. Kavanagh, David A. Nichols, Gianfranco Bertone, and Daniele Gaggero. Detecting dark matter around black holes with gravitational waves: Effects of dark-matter dynamics on the gravitational waveform. *Physical Review D*, 102(8), Oct 2020.

[96] Huan Yang, Béatrice Bonga, Zhipeng Peng, and Gongjie Li. Relativistic Mean Motion Resonance. *Phys. Rev. D*, 100(12):124056, 2019.

[97] Pau Amaro-Seoane, Patrick Brem, Jorge Cuadra, and Philip J. Armitage. The butterfly effect in the extreme-mass ratio inspiral problem. *The Astrophysical Journal*, 744(2):L20, dec 2011.

[98] E. Gourgoulhon, A. Le Tiec, F. H. Vincent, and N. Warburton. Gravitational waves from bodies orbiting the galactic center black hole and their detectability by lisa. *Astronomy & Astrophysics*, 627:A92, Jul 2019.

[99] Christopher P.L. Berry, Robert H. Cole, Priscilla Cañizares, and Jonathan R. Gair. Importance of transient resonances in extreme-mass-ratio inspirals. *Physical Review D*, 94(12), Dec 2016.

[100] Priti Gupta, Béatrice Bonga, Alvin J. K. Chua, and Takahiro Tanaka. Importance of tidal resonances in extreme-mass-ratio inspirals. *Phys. Rev. D*, 104:044056, Aug 2021.

[101] Alexandre Le Tiec, Marc Casals, and Edgardo Franzin. Tidal love numbers of kerr black holes. *Phys. Rev. D*, 103:084021, Apr 2021.

[102] Eric Poisson and Igor Vlasov. Geometry and dynamics of a tidally deformed black hole. *Physical Review D*, 81(2), Jan 2010.

[103] Eric Poisson. Absorption of mass and angular momentum by a black hole: Time-domain formalisms for gravitational perturbations, and the small-hole or slow-motion approximation. *Phys. Rev. D*, 70(8):084044, Oct 2004.

[104] R. Fujita and H. Tagoshi. New numerical methods to evaluate homogeneous solutions of the teukolsky equation. *Progress of Theoretical Physics*, 112(3):415–450, Sep 2004.

[105] R. Fujita and H. Tagoshi. New Numerical Methods to Evaluate Homogeneous Solutions of the Teukolsky Equation. II: – Solutions of the Continued Fraction Equation. *Progress of Theoretical Physics*, 113(6):1165–1182, June 2005.

[106] R. Fujita, W. Hikida, and H. Tagoshi. An efficient numerical method for computing gravitational waves induced by a particle moving on eccentric inclined orbits around a kerr black hole. *Progress of Theoretical Physics*, 121(4):843–874, Apr 2009.

[107] Misao Sasaki and Hideyuki Tagoshi. Analytic black hole perturbation approach to gravitational radiation. *Living Reviews in Relativity*, 6(1), Nov 2003.

[108] S. Mano, H. Suzuki, and E. Takasugi. Analytic solutions of the teukolsky equation and their low frequency expansions. *Progress of Theoretical Physics*, 95(6):1079–1096, Jun 1996.

[109] S. Mano, H. Suzuki, and E. Takasugi. Analytic solutions of the regge-wheeler equation and the post-minkowskian expansion. *Progress of Theoretical Physics*, 96(3):549–565, Sep 1996.

[110] M. Shuhei and T. Eiichi. Analytic solutions of the teukolsky equation and their properties. *Progress of Theoretical Physics*, 97(2):213–232, Feb 1997.

[111] Black Hole Perturbation Toolkit. (bhptoolkit.org).

[112] Adam Pound and Eric Poisson. Osculating orbits in Schwarzschild spacetime, with an application to extreme mass-ratio inspirals. *Phys. Rev.*, D77:044013, 2008.

[113] Jonathan R. Gair, Eanna E. Flanagan, Steve Drasco, Tanja Hinderer, and Stanislav Babak. Forced motion near black holes. *Phys. Rev.*, D83:044037, 2011.

[114] Black Hole Perturbation Club. (https://sites.google.com/view/bhpc1996/home).

[115] Eric Poisson and Clifford M. Will. *Gravity: Newtonian, Post-Newtonian, Relativistic*. Cambridge University Press, 2014.

[116] Adam Pound and Eric Poisson. Osculating orbits in schwarzschild spacetime, with an application to extreme mass-ratio inspirals. *Phys. Rev. D*, 77:044013, Feb 2008.

[117] Stanislav Babak, Jonathan Gair, Alberto Sesana, Enrico Barausse, Carlos F. Sopuerta, Christopher P.L. Berry, Emanuele Berti, Pau Amaro-Seoane, Antoine Petiteau, and Antoine Klein. Science with the space-based interferometer lisa. *Physical Review D*, 95(10), May 2017.

[118] Curt Cutler and Michele Vallisneri. Lisa detections of massive black hole inspirals: Parameter extraction errors due to inaccurate template waveforms. *Physical Review D*, 76(10), Nov 2007.

[119] Michael L. Katz, Alvin J.K. Chua, Lorenzo Speri, Niels Warburton, and Scott A. Hughes. Fast extreme-mass-ratio-inspiral waveforms: New tools for millihertz gravitational-wave data analysis. *Physical Review D*, 104(6), Sep 2021.

[120] Barry Wardell, Adam Pound, Niels Warburton, Jeremy Miller, Leanne Durkan, and Alexandre Le Tiec. Gravitational waveforms for compact binaries from second-order self-force theory. *arXiv*, eprint: 2112.12265, Dec 2021.

[121] Philip Lynch, Maarten van de Meent, and Niels Warburton. Eccentric self-forced inspirals into a rotating black hole. *arXiv*, eprint: 2112.05651, Dec 2021.

[122] Pau Amaro-Seoane et al. Astrophysics with the Laser Interferometer Space Antenna. *arXiv*, eprint: 2203.06016, Mar 2022.

[123] Soichiro Isoyama, Ryuichi Fujita, Hiroyuki Nakano, Norichika Sago, and Takahiro Tanaka. Evolution of the Carter constant for resonant inspirals into a Kerr black hole: I. The scalar case. *PTEP*, 2013(6):063E01, 2013.

[124] Soichiro Isoyama, Ryuichi Fujita, Alvin J. K. Chua, Hiroyuki Nakano, Adam Pound, and Norichika Sago. Adiabatic waveforms from extreme-mass-ratio inspirals: An analytical approach. *Phys. Rev. Lett.*, 128:231101, Jun 2022.

[125] Zachary Nasipak and Charles R. Evans. Resonant self-force effects in extreme-mass-ratio binaries: A scalar model. *Phys. Rev. D*, 104:084011, Oct 2021.

[126] *Gravitational-Wave Data Analysis*, chapter 7, pages 269–347. 2011.

[127] Michael L. Katz, Alvin J. K. Chua, Niels Warburton, and Scott A. Hughes. BlackHolePerturbationToolkit/FastEMRIWaveforms: Official Release, August 2020.

[128] David Bronicki, Alejandro Cárdenas-Avendaño, and Leo C. Stein. Tidally-induced nonlinear resonances in EMRIs with an analogue model. *arXiv*, eprint: 2203.08841, Mar 2022.